UNIVERSITY COLLEGE LONDON

Faculty of Mathematics and Physical Sciences

Department of Physics & Astronomy

THE DARK ENERGY CAMERA'S OPTICAL CORRECTOR

Thesis submitted for the Degree of Doctor of Philosophy of University College London

by

Michelle Louise Antonik

March 20, 2012

To My Parents, For Everything

I, Michelle Louise Antonik, confirm that the work presented in this thesis is my own. Where information has been derived from other sources, I confirm that this has been indicated in the thesis.

Abstract

This thesis details the design, construction and alignment of the Dark Energy Survey's optical corrector. The Dark Energy Camera (DECam) is a new wide-field corrector with a 2.2 square degree field of view and five filters covering the visible wavelengths. It has been commissioned as an upgrade for the Blanco telescope at the Cerro Tololo Inter-American Observatory in Chile.

The initial discussion in this thesis centres on the verification of the compression modulus of the rubber used in the opto-mechanical design. Experimental results are compared against the theoretical models used in the design of the optical corrector. This leads into the techniques created to ensure the identical reproduction of these rubber pads. The testing of the chemical composition of the cell material is then explored along with its thermal expansion properties in order to determine compliance with the specifications. The discussion on the design of DECam is completed with the metrology of the cells and the mapping of the variations from flat and the non-circularity on the alignment surfaces.

The thesis then extends to the alignment of the lenses (both prototype and DECam) within their cells and the tolerances to which they are held. Finally the effect of misalignment of the lenses on the weak lensing signal was investigated. Each lens was considered individually and then random misalignments were used to look at multiple lens misalignments. A quantitative system was used to determine the relative importance of the lenses for ensuring the best possible optical performance from the perspective of the weak lensing community.

Preface

The optical corrector for the Dark Energy Survey (DES) could never be the work of one person. The collaboration itself consists of 27 different institutions over 6 countries. University College London (UCL) has been involved with both the science and instrumentation side of DES. Instrumentationally UCL has been heavily involved in the Dark Energy Camera (DECam), including design work on the optics and lens-cells as well as taking responsibility for the contracts of these components. UCL is also performing the alignment of the lenses into their cells and the attachment into the barrel, as well as ensuring the alignment does not change during transportation to the telescope. Brenna Flaugher from the Fermi National Accelerator Laboratory is the DES Project Manager with Peter Doel being the PI at UCL. His team consists of the author; Dr Brooks, an optical physicist; and a post-doc, Dr Lanigan, who was present for one year.

This thesis discusses the final design, construction and alignment of the optical corrector for the DECam as well as the impact of lens misalignment on the weak lensing scientific output. Background is presented in chapeter 1 which is an introduction to the science behind DECam and previous wide-field optical correctors, chapter 2 details the inital design of DECam and chapter 5 gives details on the polishing of the lenses. Work in this thesis that was performed by the author is documented in chapters 3, 4, 6 and 7. Chapter 3 discusses the work done on verifying the compressibility of thin RTV pads and the processes required for identical reproduction as required by the design. Chapter 4 then discusses the cell material composition and the metrology of the cells with chapter 6 detailing the alignment of both the prototype lens and cell and the final optical corrector. The effects of the misalignments within the optical corrector on the weak lensing scientific output are discussed in chapter 7.

The collaborating member institutions of DES are: The Fermi National Accelerator Laboratory, The University of Chicago, The National Optical Astronomy Observatory, University College London, University of Cambridge, University of Edinburgh, University of Portsmouth, University of Sussex, University of Nottingham, Observatorio Nacional, Centro Brasileiro de Pesquisas Fisicas, Universidade Federal do Rio Grande do Sul, The Ohio State University, Texas A&M University, Ludwig-Maximilians Universitt, Excellence Cluster Universe, The University of Illinois at Urbana-Champaign, The Lawrence Berkeley National Laboratory, Instituto de Ciencias del Espacio, Institut de Fisica d'Altes Energies, Centro de Investigaciones Energeticas, Medioambientales y Tecnologicas, The University of Michigan, The University of Pennsylvania, Argonne National Laboratory, University of California Santa Cruz, SLAC National Accelerator Laboratory and Stanford University.

Funding for this project has been provided by: U.S. Department of Energy, U.S. National Science Foundation, Ministry of Science and Education of Spain, Science and Technology Facilities Council (STFC) of Great Britain, Higher Education Funding Council for England, National Centre for Supercomputing Applications at the University of Illinois at Urbana-Champaign, Kavli Institute of Cosmological Physics at the University of Chicago, Conselho Nacional de Desenvolvimento Cientfico e Tecnolgico, Financiadora de Estudos e Projetos, Fundao Carlos Chagas Filho de Amparo Pesquisa do Estado do Rio de Janeiro, Ministrio da Cincia e Tecnologia and by the collaborating DES institutions.

Shoot for the moon. Even if you miss, you'll land among the stars.

Unknown

Contents

List of Figures

List of Tables

Chapter 1

Introduction

Space, says the introduction to the guide, is big. Really big. You just won't believe how vastly, hugely, mind bogglingly big it is.

The Hitchhiker's Guide to the Galaxy, Douglas Adams

The current standard cosmological model is the ΛCDM model where the universe is comprised of approximately 73% dark energy, 23% dark matter and only about 4% baryonic matter[1]. To particle physicists baryonic matter is comprised of three quarks, e.g. protons and neutrons, whereas cosmologists use a more extended definition to include leptons, e.g. electrons, that encompasses all the 'normal' matter that is seen around us and in the stars and galaxies.

In 1998 it was discovered that the expansion of the universe was accelerating[2][3]. This was an unexpected finding as it was thought that the expansion rate of the universe would be decreasing due to the effect of gravity. This led to the proposal of a new force, dark energy, to account for this acceleration. The term dark energy is used to cover several theories regarding its origin. The two current leading theories are that either a negative vacuum pressure fills the universe or that General Relativity breaks down at large distances. Both theories can largely be described in the same way, either with an equation of state parameter, w[4], or by the reinstatement in General Relativity of a cosmological constant, Λ, which Einstein famously removed after Hubble proved the expansion of the

universe. The equation of state for a negative pressure fluid is equal to the ratio of the dark energy pressure, p and the dark energy density, ρ, so[1]

$$w = \frac{p}{\rho} \tag{1.1}$$

Dark matter is described in the standard cosmological model as non-relativistic (therefore slow and hence cold), non-colliding particles. As it does not emit light in the electromagnetic spectrum the term dark is used, hence it is called cold dark matter (CDM)[1]. However, it can be detected by its gravitational force. The evidence for dark matter originally came from the rotation curves of galaxies which could not be explained without a large hidden mass associated with the galaxy. Other evidence for dark matter came from the measurement of the velocities of galaxies in clusters, where the visible mass of the cluster is not large enough alone to prevent dispersion of the cluster[5].

The aim of the Dark Energy Survey is to determine w to 5% and the dark energy density to ± 0.01. This will be a significant reduction from the current precision of w of about 15%. DES will use several complementary methods to detect the effects of dark energy and dark matter, allowing better resolving of systematic errors as well as constraining w more strongly than if a single technique had been used. Approximately 300 million galaxies will be imaged between redshifts z = 0.2 to z = 1.3 in over 5000 square degrees of sky in the southern hemisphere. This will generate a large and deep galaxy catalogue, which will also be one of the largest public image archives in the world[4]. In order to undertake the survey the 4 meter Blanco telescope at the Cerro Toloro Inter-American Observatory (CTIO) in Chile is to be upgraded with new wide-field camera with a 2.2 degree of view focal plane, called DECam[6].

1.1 Detection Methods Used in DES

Several methods are proposed to be used in DES to measure the dark energy equation of state and the densities of dark energy and dark matter. These are: light curves from supernovae; galaxy clustering; and weak gravitational lensing[4].

1.1.1 Type Ia Supernovae

Type Ia supernovae are believed to occur in binary star systems where a white dwarf has accreted mass from its binary partner. This continues until the Chandrasekhar mass limit is reached, at which point the star implodes and goes supernova[1]. All type Ia supernovae have the same maximum absolute brightness allowing them to be used standard candles. Hence, a comparison of the relative brightness of the supernovae allows relative distances to be measured. This luminosity distance can then be combined with the redshift from multiple supernova events allowing the expansion history of the universe to be plotted[1].

DES will use photometric redshifts, or photo-z, which heavily relies on the $4000\mathring{A}$ break, a sharp drop-off in the light emitted by galaxies at wavelengths below $4000\mathring{A}$. By determining the position of this break the redshift of the galaxy can be found. DECam's five filters will be used on the same patch of sky; by measuring the light from each galaxy in each filter the position of the $4000\mathring{A}$ break can be determined[4]. DES will provide better cosmological constraints than existing surveys due to its larger sample size and more precise calibration. It is hoped that DES will identify 1900 type Ia supernovae over its operational lifetime[7].

1.1.2 Galaxy clustering

Large cluster surveys look at the abundance and evolution of galaxy clusters. The abundance of galaxy clusters helps to give estimates on dark energy's influence on the expansion of the universe. This can be achieved by measuring the change in the number of galaxies within a given volume at different redshifts, charting the expansion of the universe[7].

The formation of galaxy clusters is influenced by initial perturbations and gravitational collapses making it highly dependent on dark matter[7]. As they evolve the gravitational attraction between the galaxies keeps the cluster together as the dark energy tries to push them apart. This allows estimates to be made of the strength of dark energy relative to gravity. Several features within a galaxy cluster's power spectrum are dependent on matter and baryon densities, creating a standard ruler. These can be compared to the angular scale of the same features from the angular power spectrum. The comparison of the angular scale with the luminosity allows an angular distance to the cluster's redshift to be derived[4].

1.1.3 Weak gravitational lensing

Weak lensing is a direct measurement of the gravitational potential, and hence mass, between a galaxy and Earth. The gravitational lensing effects can be seen most easily in strong lensing where an intervening gravitational potential, e.g. a black hole, can cause Einstein rings. These are formed when the galaxy behind the lensing object is smeared into a circle. More commonly seen are arcs, either due to a less strong lens or the lensing effect is not happening in a direct line between the object and Earth. Weak lensing occurs when the light from a distant galaxy has been distorted by the gravitational force of dark matter between the galaxy and Earth, this has the same effect as Einstein's rings and arcs but on a much smaller scale. Rather than forming an arc, the galaxy appears to have been stretched slightly into a 'banana' like shape which is called a shear pattern. There is a coherent correlation between the shear pattern caused by the gravitational force and the mass of the dark matter present. This allows the use of these distortions to directly determine the amount of dark matter between Earth and the distant galaxy[8]. However, the size of this induced shear is very small, of the order of 1% of the galaxy's size[9], which is often smaller than the distortions put into an image by the telescope and atmosphere. DES will have extremely small telescopic distortions that can be accurately calibrated out. This will allow more precise measurements of these shears by reducing the uncertainity in the image detected.

It is not possible to distinguish between the shear distortion caused by dark matter and the intrinsic ellipticity of the original shape of the galaxy[10]. Light from associated galaxies will follow a similar path, passing through the same dark matter gravity well and gain the same shear distortion. If the galaxies were originally aligned randomly then the average ellipticities of all the galaxies would give the shear signal. However, groups of near-by galaxies have probably formed within the same large-scale gravity field. This will cause them to have some intrinsic alignment between them[10]. This must be accurately determined and removed to prevent a systematic error in the shear calculation. The removal of this intrinsic alignment is generally done using one of two main techniques. The first, nulling, places extra steps into the image processing weighting signals to remove the intrinsic alignment signal, but requires knowledge of the redshift of the galaxies. Alternatively, a model can be created for the intrinsic alignment of a given survey which is then added to the predictions used to measure the shears of a given galaxy[11].

Figure 1.1 shows a schematic of a light path due to weak lensing. The light from a distant source is bent by an intervening gravity potential. Assuming that this happens over a small distance it can be likened to the thin lens approximation. The distance to the source of the gravity potential, χ, is dependent on both a spatial distance as well as the redshift of the light. This makes it appear that the source has moved, making its actual position uncertain. This makes it impossible to probe the gravitational potential using the change in angle. The distortions placed into the image by the dark matter are used instead[9].

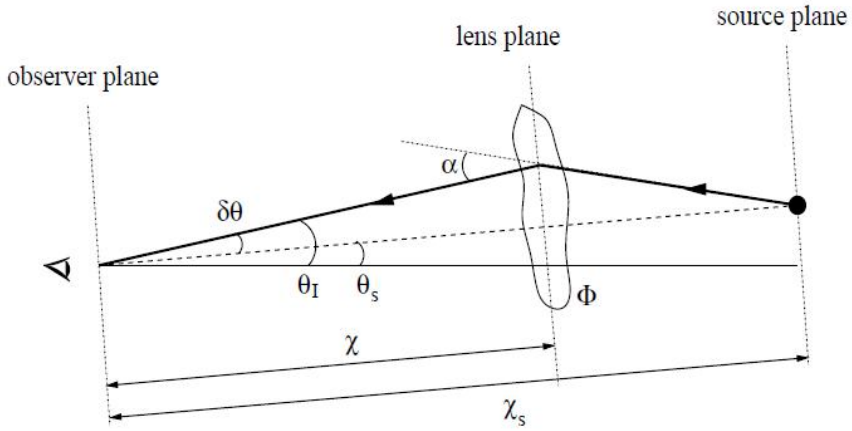

Figure 1.1: Schematic of weak lensing[9]. A light ray is deflected by an angle α from a source at distance χ_S by the gravitational density, Φ, at a distance χ. θ_S is the intrinsic position of the object and θ_I is its observed position.

1.2 Previous Optical Correctors

In the past few years several wide-field correctors of similar size to DECam have been constructed. Here a brief overview is given of a few recent modern wide-field correctors that use similar design techniques to DECam.

1.2.1 MMT

The Multiple Mirror Telescope (MMT) underwent an upgrade to be converted into a single 6.5m primary mirror. A three element refractive corrector near the Cassegrain focus has been added, giving a 1° field of view designed to look at wavelengths between 0.33 and 1.1 microns[12]. The fused silica lenses vary in size between 0.52-0.83m in diameter[13], slightly smaller than those used in DES. The lenses are supported in cells made from Invar 39, with a coefficient of thermal expansion (CTE) of 2.3x10^{-6}/°C which are attached to a carbon steel barrel with a CTE of 12x10^{-6}/°C. Flexures were used to attach the cells to the steel to compensate for the CTE difference between the two metals[12], similar to those used in the DES design.

Room temperature vulcanising silicone rubber (RTV) was used to mount the lens in the axial direction to absorb machining irregularities within the cell and provide a 24 point support for the lens to rest on[13]. Precast axial pads were used with a thin layer of glue, when attached to the cell they had a height variation of less than 25μm. The optic was lowered onto the cell with alignment tolerances of the centring of the lenses to the cells of 75μm, similar to those tolerances required by DECam.

To create an athermal system in the radial direction, RTV560 was used to mount the lenses within their cells. The thickness of the RTV pad was designed to match the thermal expansion difference between the lens and the cell[12]. Once the lens had been aligned in its cell the RTV radial pads were placed around the lens circumference, bonded to mounting brackets[12], a schematic of this is shown in figure 1.2.

The DECam design also uses several features similar to those employed by the MMT optical corrector. These are the use of a specialist, low thermal expansion material for the holding cell with RTV pads creating an athermal system and flexures to compensate for the difference between the cell and its support structure. DECam will also use RTV pads to rest the lens on in order to create multiple support points.

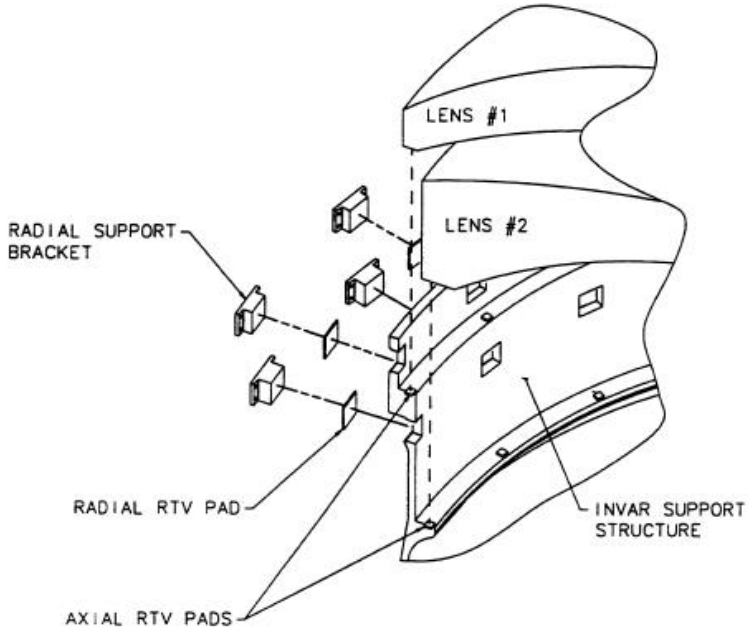

Figure 1.2: Expanded view of the RTV radial mounting system used on the MMT[12].

1.2.2 LBT

The Large Binocular Telescope (LBT) has two optical imagers, one optimised for the UBV bands (the Blue channel) and the other is optimized for the VRIZ bands (the Red channel). They are designed to look at the same area of sky allowing both the optics and the CCDs to be optimised for a smaller wavelength range. Different types of CCDs are used in each imager to give maximum signal output. Each optical corrector has six lenses with a maximum diameter of 0.8m and 8 filters. The optical designs are similar but with different glasses (fused silica in the Blue channel and BK7 in the Red channel) to allow optimal transmission of light in the blue and red channels[14].

The lenses are mounted in Invar cells connected to a steel barrel via flexures to account for the CTE difference between the two materials. The two largest lenses, with diameters of 0.8m and 0.4m, are mounted into their cells with RTV pads to compensate for the difference between the co-efficients of thermal expansion (CTEs) of the glass and cell[14].

To ensure that the lenses did not shift during transportation between the laboratory where they were assembled and the telescope site, an optical test was used to check the back-reflections. Figure 1.3 shows the equipment used for the alignment of the lenses in the laboratory. The lenses are in their black barrel within a white handling frame. In the foreground the optical set-up can be seen, a close up of this is shown in figure 1.4. The sixth lens was not used during this test due to its low optical power as it acts as the cryostat window; it was aligned to mechanical precision due to loose alignment tolerances.

At the telescope the optical corrector was aligned to the mechanical rotational axis of the prime focus' derotator. The back-reflection was used to generate Newton rings from five lenses with the largest lens then being cut off and a new image generated from the remaining four lenses. These Newton ring images were compared to ones taken previously at the laboratory before transport. A comparison of the images showed a probable decentre of the largest lens by 80μm decentre[16] which was then corrected.

DECam will use a similar laser system to determine the final alignment of the lenses within their barrel. It will be required when placing the lenses into the barrel as at this point some of the mechanical metrology surfaces will no longer be available. It will also be used once DECam has arrived at the telescope, to ensure that there has been no change in the positions of the lenses during transport.

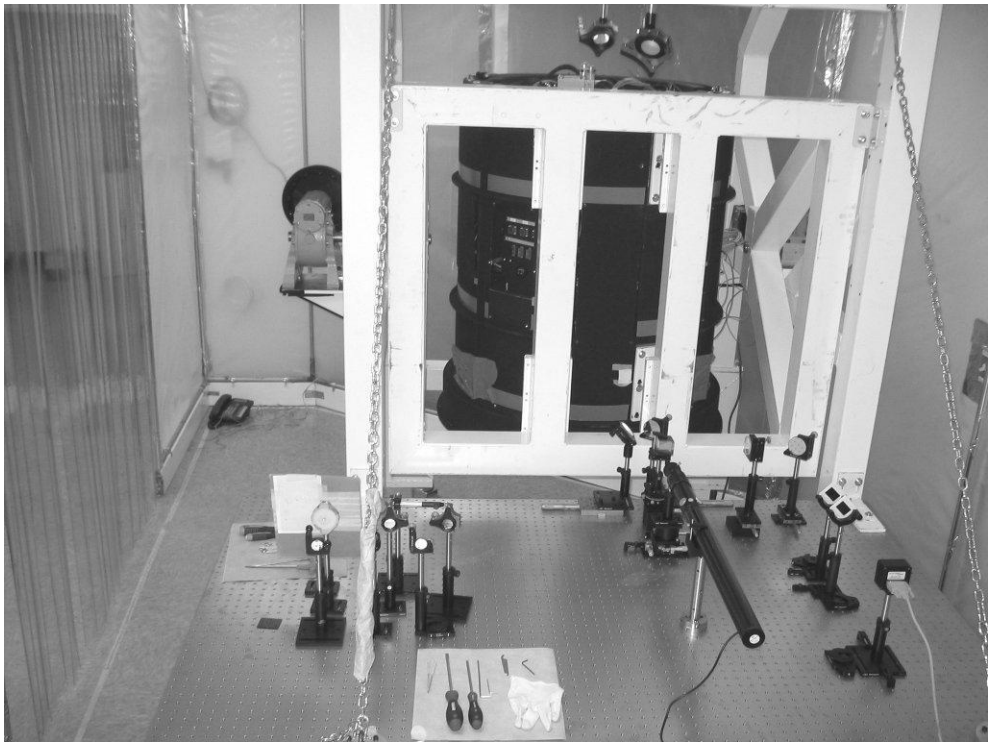

Figure 1.3: The optical alignment of the LBT[15]. The lenses are within their black barrel and held in a white handling frame.

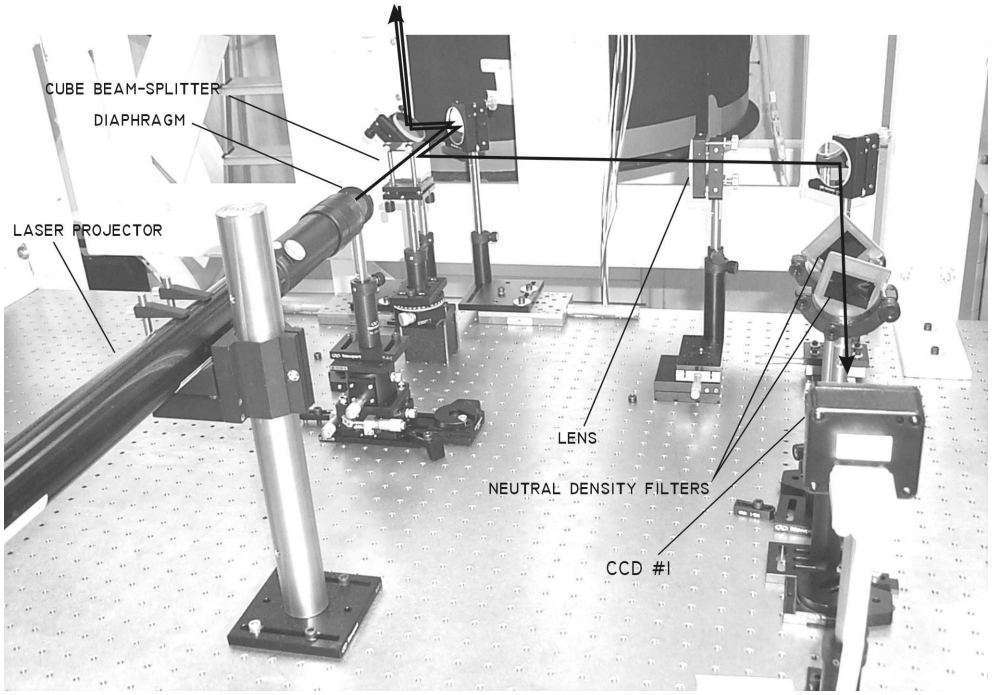

Figure 1.4: The optical bench set-up for the alignment of the LBT[15].

1.2.3 Pan-STARRS

The Panoramic Survey Telescope and Rapid Response System (Pan-STARRS) is designed to generate deep field images that are repeated every week allowing moving or variable objects to be recorded. This survey aims to catalogue objects within the solar system, especially near Earth asteroids[17], as well as look into the formation history of the Milky Way, and refine the dark energy equation of state from weak lensing, baryonic acoustic oscillations, galaxy cluster abundances and supernovae Ia lightcurves[18]. The completed system will have four telescopes with the first of them, PS-1, also being the prototype.

PS-1 is a Cassegrain style telescope with two mirrors and three lenses, the last of which forms the cryo-stat window[17]. The diameters of the lenses vary from 0.6m to 0.4m with the mirrors being 1.85m and 0.9m in diameter. It contains filters for wavebands between 400-1100nm and has a very large 7 square degree field of view. The first two lenses (L1 and L2) are held in steel cells with an RTV layer used to hold the lenses athermally. They are held in a different structure to the last lens (L3) and the camera. The camera section can rotate independantly of the first two lenses allowing misalignments to be isolated to either the L3/camera structure or the L1/L2 holding structure[19].

The original specification on the image quality was to have a spot size with a full width-half maximium (FWHM) of 0.4"[18] but the first images had a 5" FWHM. After investigation using out of focus donuts, where a linear relationship between intensity and optical aberrations can be found, alignment errors were discovered. The L1 and L2 lenses had been placed 5.6mm further from the focal plane than expected and there was a spacing error between L1 and L2 of 0.49mm. The location of the optical centre of the lens had an error of 0.8mm as well as issues with the flatness of the focal plane due to differences in the CTEs of the materials used. Between 2007 and 2008 two major adjustments of the optics were undertaken as well as work to control the temperature within the telescope's dome. This gave image quality of approximately 1.75". A third run was done after the camera was completely cooled, reducing heat under the mirror and allowed the image quality to reach 1.6"[19]. Further adjustments have given PS-1 an image quality of 0.6" across the telescope's entire field of view[18]. Pan-STARRS's image quality issues highlight the importance of precise metrology of all components within the DECam as well as the need for exact alignment of component parts.

Chapter 2

The Design of the Dark Energy Camera

In theory there is no difference between theory and practice. In practice there is.

Jan L. A. van de Snepscheut

DECam is comprised of multiple subsystems that will be combined at the observatory to produce a working camera. The subsystems are: the telescope's primary mirror; and the primary cage above the mirror; a hexapod structure for fine motions between the cage and barrel which holds the optics; the filter; and the imager. This chapter summarises these subsystems and presents the design of the optical system. All the work presented here was either completed before the author joined the collaboration or was done by groups the author was not involved with.

Figure 2.1 is a model of the completed DECam system, showing the primary cage with the hexapod, barrel, filter and imager subsystems clearly visible. The first optic (grey) can be seen within the barrel (blue). The large pink section is the imager behind the grey filter changer. The pale yellow hexapod is wrapped around the barrel.

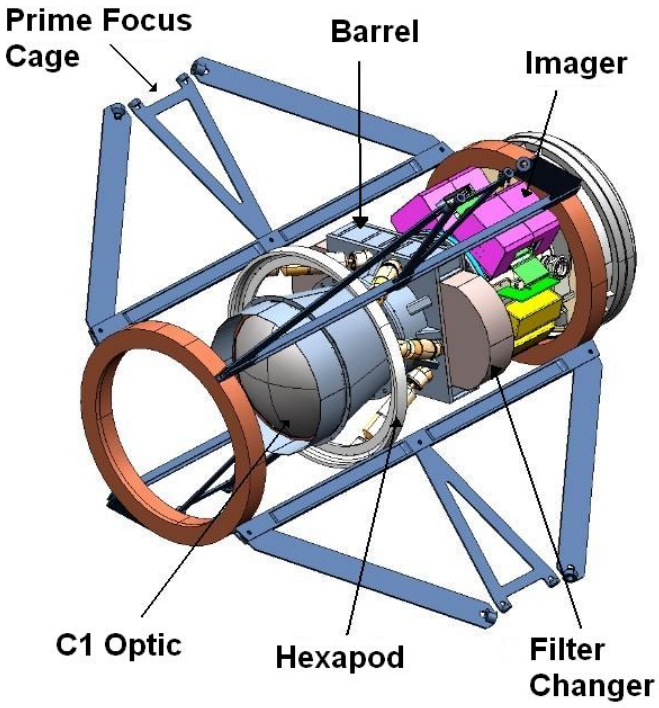

Figure 2.1: Model of the completed DECam in the prime focus cage[20].

2.1 The Blanco Telescope

The Victor M. Blanco telescope is a wide-field Ritchey-Chretien design with a prime focus at f/2.7, pictured in figure 2.2. The telescope itself required some upgrade work to allow DECam to function optimally. Some of the improvements it is currently undergoing are upgrading the mirror support, and recentering and stabilising the primary mirror to reduce coma. Finite element analysis was performed to determine movement in the prime focus cage that must be removed by the hexapod system[21].

The telescope control systems are also undergoing an upgrade to allow the telescope to slew 3° in 20 seconds, a greater amount than the DECam requirement of 2° in 17 seconds. The telescope positioning must be better than 0.5 arcsec/min and the jitter is to be no more than 0.1 arcsecond R.M.S[22].

2.2 The Hexapod System

The hexapod system connects DECam to the prime focus cage. It allows compensation of misalignments between the instrument and telescope axis which can occur through changes in gravitational loads and thermal expansion. Adjustment of the instrument's

Figure 2.2: The Blanco dome[23] and the telescope[24] at CTIO, Chile.

position may be required in six directions; movement in the X,Y and Z axes as well as rotation around these directions. In the Z direction there is a range of movement of 60mm and in X and Y directions a range of 30mm. For the tip (rotation around the X axis) and tilt (rotation around the Y axis) the hexapod can move by up to 200 arcseconds[25]. Adjustment in the rotational directions is likely to only be performed once during the initial alignment of the camera to the primary mirror. The X and Y axes will dominate in the correction for structural sag or thermal compensation with the Z axis being used for active focusing of the camera[26].

2.3 The Barrel

The barrel provides a stable mounting platform for the optics, filters and imager. It is split into three main parts as shown in figure 2.3, all of which are made from steel. The body of the barrel is reinforced to take the weight of the camera through to the hexapod. It also contains the filter changer and shutter which extend out of the body. Four of the lenses will be mounted in or on the outside of the body section. The largest lens, C1, will be mounted on the cone section with the shroud providing protection. Access ports in the side of the barrel allows the lens-to-lens spacing to be checked and also gives access for cleaning[27].

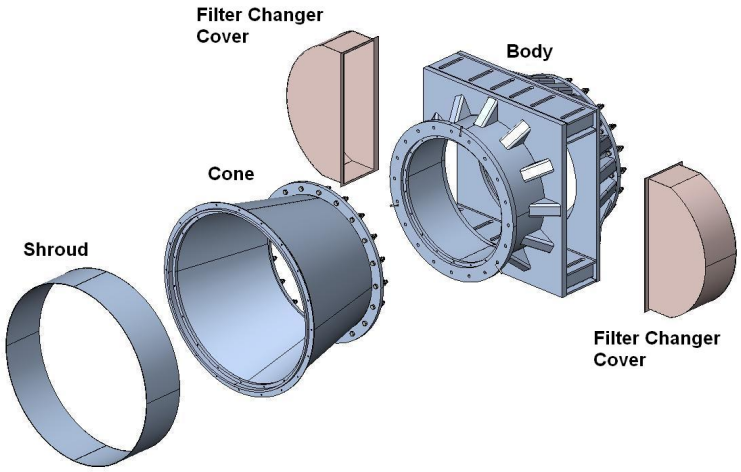

Figure 2.3: Exploded view of the component parts of the barrel[27]. Far left is the shroud followed by the cone then body. Covers for the filter chamber flank the body of the barrel.

2.4 The Imager

The focal plane has a 3 square degree field of view and is made up of 74 chips. 62 2k×4k science chips are arranged in a hexagon, as shown in figure 2.4, with 12 2k×2k guidance and focusing chips arranged around the edge of the science chips[28].

The imager is in a cryogenic vacuum vessel, 24 inches in diameter, designed to keep the CCDs between -120°C and -80°C when in operation. As well as containing the CCDs there is an internal cooling system and a vacuum interface board (VIB) that transfers the CCDs output to the readout crates (FEE crates)[29]. A model of this system can be seen in figure 2.5 with the completed system in figure 2.6.

The temperature requirements for the CCDs to function optimally, and with minimum noise, are that the temperature must remain stable to 1°C over a single CCD for 12-18 hours with less than 10°C variation over the entire CCD plane[31]. The focal plane also has tight tolerances with a peak-to-peak variation in the CCDs to be no more than 30μm. On scales of less than 1cm^2 this flatness should be less than or equal to 3μm. Between adjacent 1cm^2 areas the flatness can vary by no more than 10μm[32].

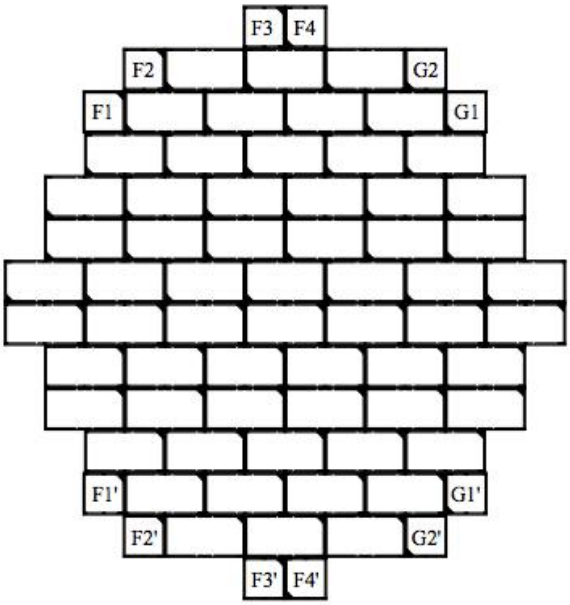

Figure 2.4: CCD layout on the DECam focal plane. Chips marked 'F' are for focusing and alignment. Those marked 'G' are guidance chips and the unmarked chips are the science CCDs[28].

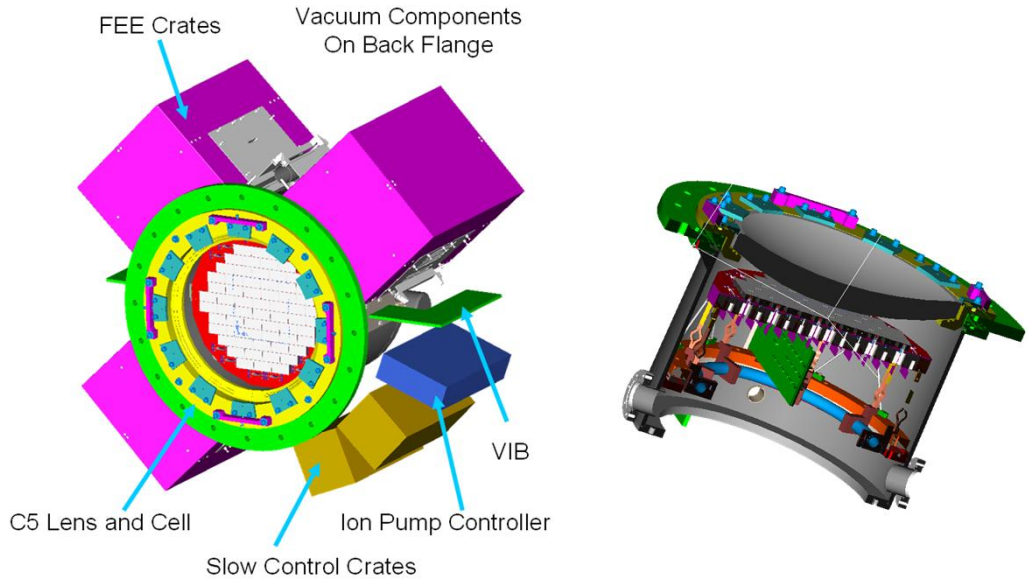

Figure 2.5: Model of the imager vessel[29]. On the left is an isometric view of the imager and on the right is a cross-section through the image vessel, showing the CCDs and C5 lens and cell.

Figure 2.6: The completed CCD imager vessel[30].

2.5 The Filters

The filters for DECam are very large, with a minimum clear aperture of 600mm and are specified to be no thinner than 13mm, with a transmitted wave error on any given 125mm diameter sub-aperture of better than $\lambda/4$[33]. The wavebands used in DECam cover the optical range and head into the IR. These wavebands are broadly similar to those used in the Sloan Digital Sky Survey. Table 2.1 summarises the wavelength requirements of the filters with a graph of the bandpasses in figure 2.8.

Filter	Centre wavelength(nm)	Wavelength Range (nm)	FWHM(nm)	Average absolute transmission
DES g	475	415-535	150	85%
DES r	635	575-695	150	85%
DES i	775	715-835	150	85%
DES z	925	865-985	150	85%
DES y	Approx. 1000	985-1005	100	85%

Table 2.1: Filter wavelength specifications for the DES filters[33][34].

These filters are placed into a filter changer mechanism (FCM), shown in figure 2.7, which attaches to the body of the barrel. This can hold eight filters, allowing later addition of filters if needed by the astronomical community[28]. A filter can be stowed and a new one deployed in under 10 seconds[34].

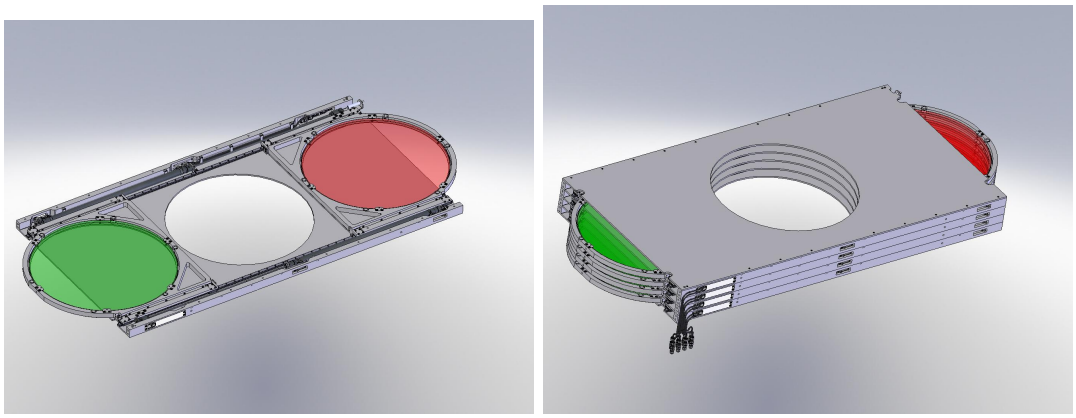

Figure 2.7: The filter changer mechanism[34]. Shown on the left is a single layer with two carriages, each containing one filter. The central hole is along DECam's optical axis and when in use the filter will be positioned there. On the right is the completed FCM comprising of four layers within the cartridge.

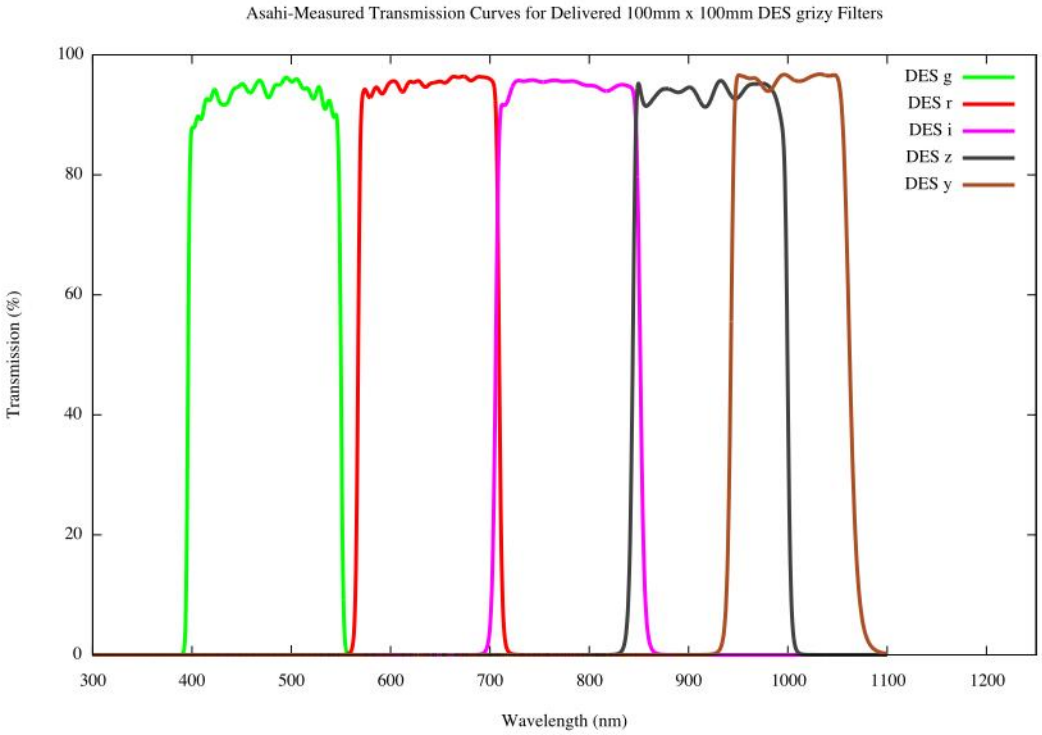

Figure 2.8: Filter band passes that have been achieved by the manufacturer on samples 100mm square[28].

2.6 The Optics

The camera optics consists of five singlet lenses named C1 to C5 in order of position in the camera. C1 is the front lens, C2 and C3 are mounted as an air spaced doublet, the filters are situated between C3 and C4, with C5 acting as the cryostat window. The lenses are held in cells that connect to the barrel. The barrel will be constantly purged with dry nitrogen to give a stable and dry environment for the optics and their coatings[4][35]. Figure 2.9 shows the optical layout of these lenses with the primary mirror to the right. There are two aspheres in the system, the first on the concave surface of C2 and the second on the convex surface of C4. The challenge in the alignment of these lenses comes from their size and weight, given in table 2.2. C1 should be noted for its very steep radius of curvature.

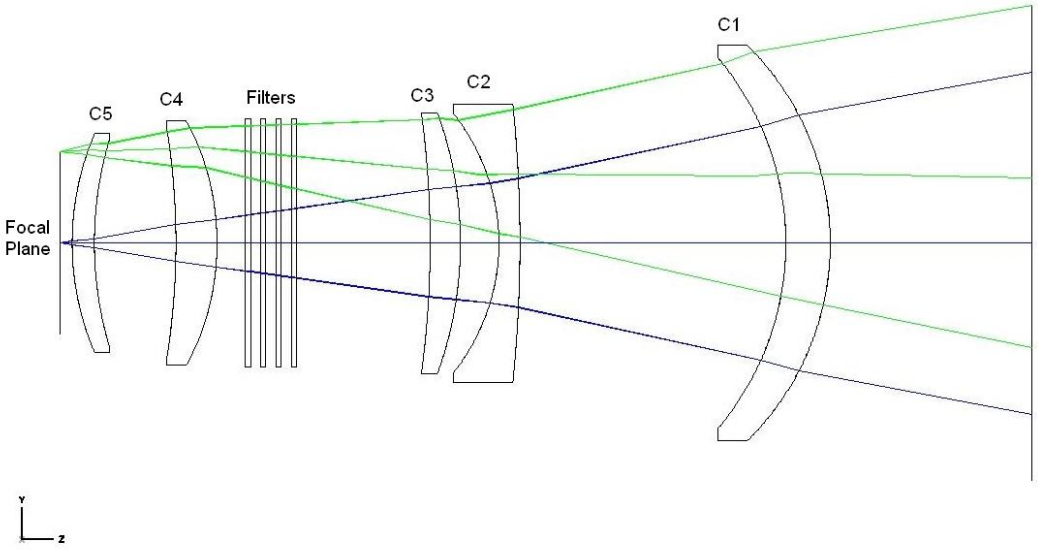

Figure 2.9: Optical design for DECam as designed by Rebecca Bernstein and Sue Worswick.

The lenses are made from HPFS 7980, a standard grade of fused silica made by Corning[36]. It is a non-crystalline and colourless glass with a thermal expansion coefficient of 0.57ppm/K between 0-200°C[38]. Inhomogeneities within the glass were specified to be under 2ppm for lenses C2-C5 and under 5ppm for C1, the looser requirements set by the slumping process that C1 underwent to shape the blank[36].

Lens	Radius of curvature on Surface 1 (mm)	Radius of curvature on Surface 2 (mm)	Centre Thickness (mm)	Edge Thickness (mm)	Diameter on Surface 1 (mm)	Weight (kg)
L1	685.821	711.827	112.1	74.34	980.74	172.36
L2	3387.346	507.055	51.285	148.11	690.12	87.20
L3	943.975	2415.952	75.1	38.27	652.54	42.62
L4	662.779	1797.683	101.68	52.48	604.99	49.69
L5	-900.000	-685.127	54.68	36.19	512.00	24.37

Table 2.2: Dimensions of the DECam lenses as requested for manufacturing at SESO[36][37].

2.6.1 Optical tolerances

Weak lensing requires the accurate measurement of the ellipticity of galaxies and it is this science that drove the tolerancing budget. These shapes are affected by the point spread function (PSF) of the atmosphere, telescope and camera. To remove as much uncertainty as possible from the shear measurements the PSF across the instrument must be as stable and uniform as possible. The requirement placed on DES was to have a PSF with a full width half maximum (FWHM) no greater than 0.55 arcseconds. It is expected that this will give an error on the shear measurements of 0.1%, corrosponding to an error in the weak lensing ellipticity of 0.06 arcseconds for a 1.2 arcsecond galaxy (DECam's limit of resolution). To meet this target a PSF budget has been compiled, shown in table 2.3, that was then used to calculate the tolerances on the optics and for alignment[39].

The PSF budgets were converted into tolerances in arcseconds and microns for every component in DES. The lenses had manufacturing, assembly and dynamic tolerances. The assembly and dynamic tolerances are given in table 2.4. The assembly tolerances are the accuracy to which the lenses must be aligned to the optical axis of the camera, this was further broken down into the budget for the fiducals holding the barrel to cell and the lens to cell alignment, this sub-section is shown in table 2.5. The dynamic tolerances limits the amount the lens should be able to move when the telescope is tracking across the sky. In both cases these are measured with respect to the central axis of the barrel, which was reproduced in the laboratory by a rotational axis of the cells and lenses.

These tolerances were based on the root mean squared (RMS) spot size in ZEMAX optical modelling software. The optics have been optimised for the r band filter. When in perfect alignment the central spot size for the r-band had an RMS of 8.42 microns. During the tolerancing it was assumed that the focus (primary mirror to optical corrector distance) can always be adjusted and that a one-off adjustment of the tilt on the focal plane can be performed with the use of the hexapod[41].

A 'worst case' alignment scenario was calculated that determined the relative lens positions which resulted in the worst image quality, whilst still having all the lenses within their tolerances. This was found by the movement of C1 to its maximum tolerance with each subsequent lenses moved until the aberrations were maximised. The resultant directions for the worst possible image quality are therefore all relative to the initial lens movement. Table 2.6 gives these relative directions.

Source	FHWM (arcsec)	Comment
Dome Seeing		Absorb in contingency
Telescope Guiding errors	0.03	Same as focus errors
Wind Shake Corrector	0	Assume calm night
Design	0.26	Average of r, i
Manufacturing tolerances	0.1	(Radii, index, thickness)
Glass homogeneity	0.065	
Assembly errors	0.0571	(decenter, tilt)
Flexure	0.035	
CCD Focal Plane flatness	0.05	Peak-peak 30 micron z error
Thermal performance	0.0466	Worst-case change of 30C (Steel)
CCD Diffusion	0.31	expected performance
Depth-of-focus in	0.03	(i depth of focus only)
CCD Primary Mirror figure	0.16	CTIO mirror testing report
Primary mirror support (static)		Absorb in contingency
Primary mirror support flexure		Assume active optics are perfect
Telescope Collimation (static)	0.05	200 micron offset of primary mirror
Telescope flexure/mirror translation		Absorb in Contingency
Focus	0.03	Scaled from 2.5m performance
TOTAL (Tel+Instrument)	0.47	
Contingency	0.29	Primary mirror support, dome seeing etc
Requirement	0.55	

Table 2.3: The PSF budget for DECam[39]. The telescope and instrument are broken down into component parts and a PSF allocation is given to each as a FWHM of the size of the PSF in arcseconds.

Lens	Assembly Tolerances		Dynamic Tolerances	
	De-centre Tolerance (μm)	Tilt Tolerance on diameter arcsec (μm)	De-centre Tolerance (μm)	Tilt Tolerance on diameter arcsec (μm)
C1	100	10 (48)	25	5.6 (27)
C2	50	17 (56)	25	8.1 (27)
C3	100	20 (63)	25	8.4 (27)
C4	100	20 (58)	25	8.6 (25)
C5	200	40 (105)	25	10 (25)

Table 2.4: Decentre and alignment tolerances of the lenses for the assembly and the stability during operation [36]. These include the barrel and cell fiducial tolerancing as well as the cell to lens centring tolerances.

Lens	tilt specification (μm)	decentre specification (μm)
C2	± 31	± 12.5
C3	± 29	± 25
C4	± 33	± 25
C5	± 75	± 100

Table 2.5: Specification of the mechanical assembly tolerances for the lens to cell alignment only[40].

Lens	Decentre	Tilt
C1	+ve	+ve
C2	-ve	-ve
C3	+ve	-ve
C4	-ve	-ve
C5	+ve	-ve
Primary mirror	-ve	-ve

Table 2.6: Relative direction of lens displacements that yields the worst image quality due to co-addition of aberrations[41].

2.6.2 Holding cells for the optics

There are two main designs for the cells that hold the lenses. One design is for lenses C1 to C4 and the other is for C5, the cryostat window. C5 must create a vacuum seal, which will prevent movement during operation of the telescope, whereas lenses C1-C4 must be held in position by the mounting to their cells.

To reduce stresses in the lenses, the lens-cell assembly for C1-C4 was designed to be athermal which required compensation of the difference between the lens and cell's expansion due to temperature changes. Although the lenses will be aligned and mounted at $20°C$ the average temperature at CTIO will be around $10°C$. To create the athermal design an intermediate layer of RTV was used, which in turn puts its own constraints on the lens-cell design. The thinner the rubber pad, the harder it is to manufacture repeatedly yet a thick rubber pad provides less support to the lens allowing large movements during telescope operations. RTV 560, a silicone rubber solution, has been in used in previous optical correctors, e.g. the MMT[12], for the same purpose. Unpublished FEA models created for this project show that a radial RTV 560 pad 1-2mm thick will provide enough support to the lenses to keep their movement during telescope operations to within the tolerances[42].

The material for the cells was then chosen using the constraints placed by the lenses having a co-efficient of expansion (CTE) of 0.57ppm/K[38] and a thin rubber pad with a co-efficient of thermal expansion (CTE) of 200ppm/K[43]. As the barrel is made from steel, this would remove the need for thermal compensation between the barrel and cell. However, steel's CTE is approximately 11ppm/K[44]. This would require a rubber pad thickness of 9.94mm[42], which is much too thick to provide the radially required support to the lens. Invar is very well known for its low thermal expansion; it contains 36% Ni with trace elements and the remainder iron (other low expansion materials are sometimes referred to by the trademark name of Invar). Invar takes advantage of an unusual CTE curve; as the ratio of nickel to iron is varied, a sharp decrease in the CTE is seen at approximately 35% nickel, as shown in figure 2.10. Whilst it is generally above 10ppm/K, between 30%Ni and 45%Ni the CTE can drop significantly lower, minimising at 36%Ni with a CTE of 1ppm/K[45]. Using Invar with a 36% Ni content would require a rubber pad thickness of 0.37mm thick. This is too thin to manufactor repeatably. By using a pure nickel-iron alloy, and moving up the graph in figure 2.10 to 38% nickel, 62% iron[36],

a CTE of 3ppm/K is formed, this requires a pad thickness of 1.48 mm to ensure the lens-cell system is athermal. Material with a pad thickness of 1.48mm allows identical reproduction as well as being stiff enough to hold the lens in position. Therefore this non-standard ratio of nickel-iron alloy was used for the cell material. This created a thermal expansion mismatch between the cell and the barrel, with the barrel expanding much more than the cell over the same temperature range. To prevent stresses travelling through to the lens from the cell-barrel interface thin flexures were put into the cell design. As they have a thickness of 1mm they can flex as the barrel moves due to temperature changes taking up the difference in expansion. This places the majority of stress from the thermal expansion differences in flexures rather than the lens. However the flexures are also strong enough not to bend under a varying gravity load. Feet on the top of the flexures allow for secure bolting of the cell to the barrel.

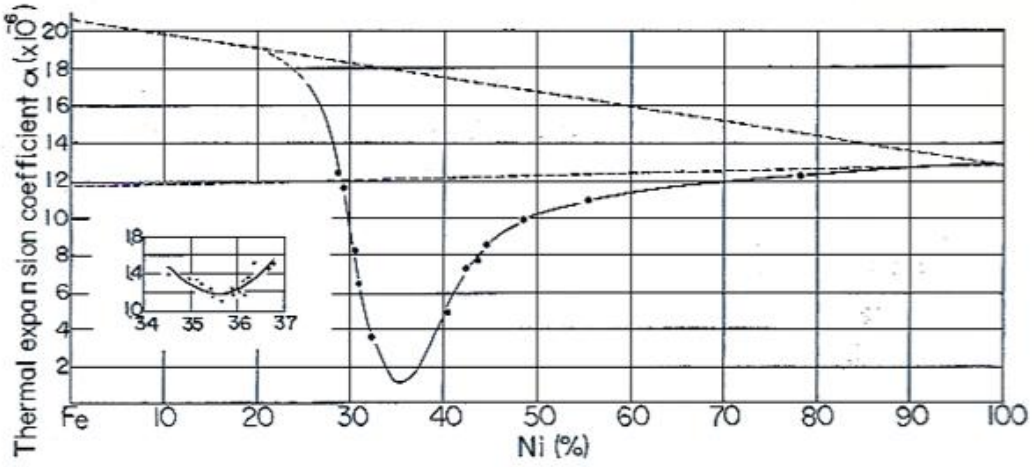

Figure 2.10: Variation of the CTE of a nickel-iron alloy with the nickel percentage[45].

A generalised design for the holding cells C1, C2 and C4 is shown in figure 2.11 with the design for C3 in figure 2.12. The difference between these designs arises from C2 and C3 being mounted as an air spaced doublet. As such C3 will bolt directly onto C2 removing the need for the flexures.

The mating ring is the reference surface for both the alignment of the cell to the barrel and for the lens to the cell. The spacer between the mating ring and the barrel allows for small changes in the inter-lens spacing. Baffles will be used to prevent excess scattering of light that may adversely affect the background light level. The retaining ring is an emergency back-up in case the radial pads, that glue the lens to the cell, should fail and the lens fall during transport or installation. The retaining pads should prevent any

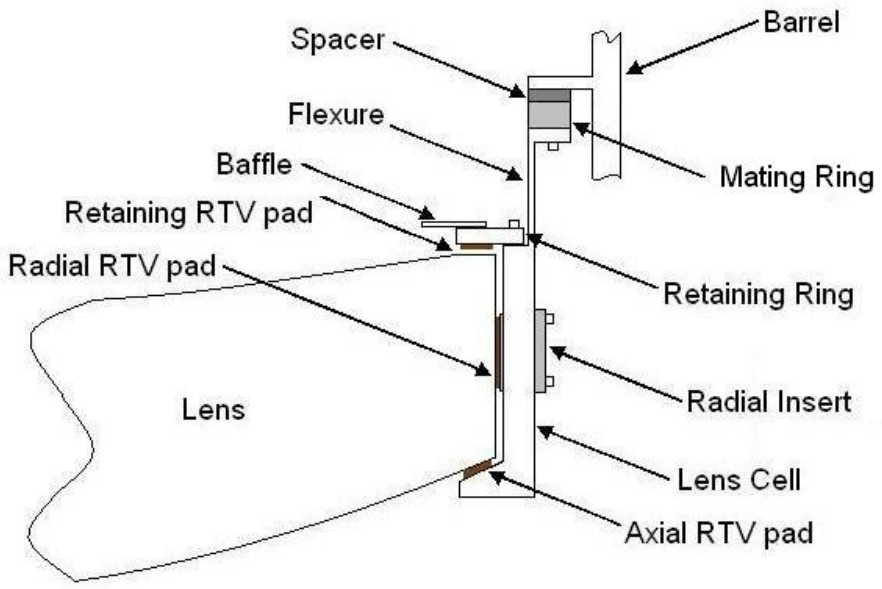

Figure 2.11: Cross-section schematic of the cell design for lenses C1, C2 and C4.

damage occurring to the lens.

RTV pads are used to hold the lenses in position within their respective cells. The rubber compound can bond to both metal and glass via primers. On the axial surface the pads are bonded only to the metal with the weight of the lens compressing the pads to give contact over the total area of the pad. The radial pads are bonded to both the lens and cell. Inserts, made of the same material as the cell, are placed into specially drilled holes and screwed in. This allows the gluing of the lens once it has been aligned in its cell. The face of the insert that gets presented to the lens has a cylindrical shape, matching that of the lens and giving a constant gap.

The C5 cell is made of steel and attaches directly to the barrel. As it will be placed under vacuum the lens is not glued into position but sits on a single O-ring. Plastic mounts fit between the side of the lens and the cell which are designed to prevent any change in alignment of the lens during transportation and cycling of the vacuum.

Figure 2.14 shows a cross-section of a model of the completed optical corrector. C1 is mounted on the cone at the front with the lens being protected by the shroud. C2 and C3 are mounted at the front of the body with the filter change behind. C4 is behind the filters attached to the end of the body with the C5 cell bolted to the barrel.

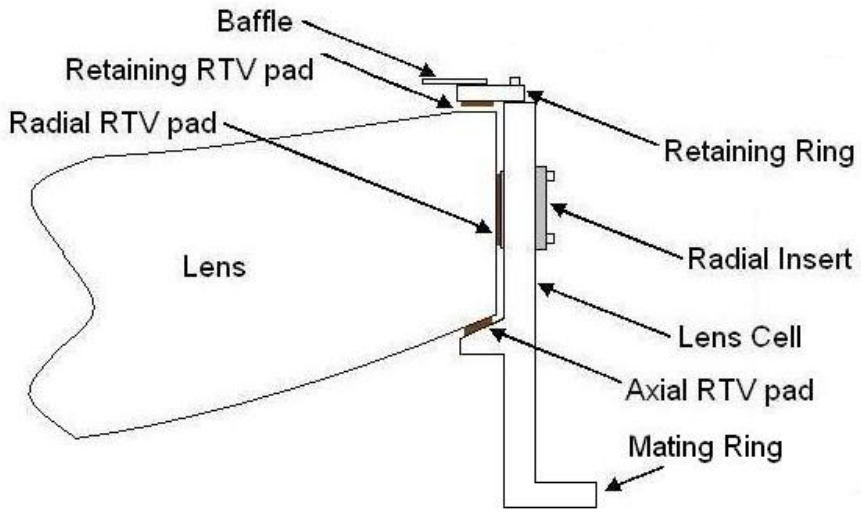

Figure 2.12: Cross-section schematic of the cell design for the C3 lens.

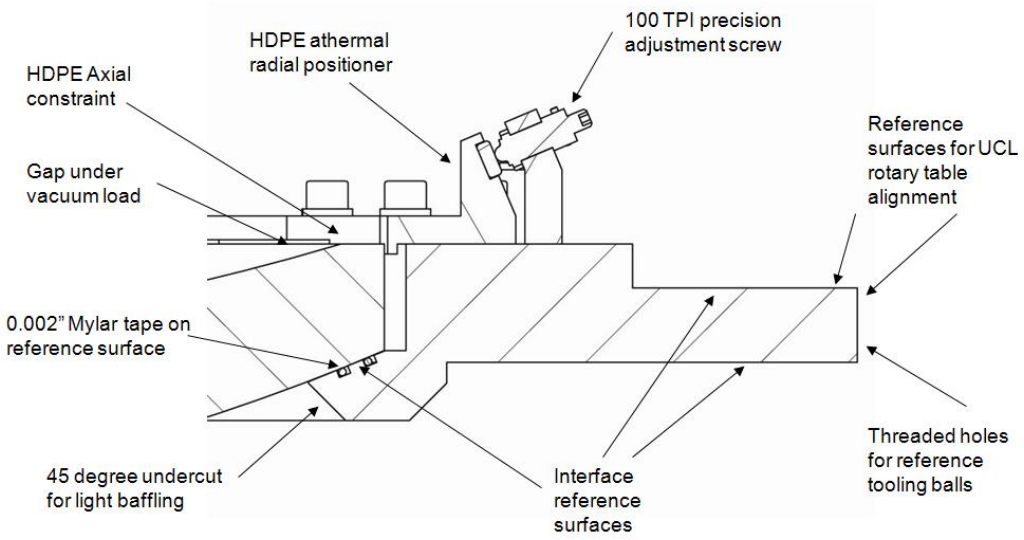

Figure 2.13: Cross-section schematic of the cell design for the C5 lens[46].

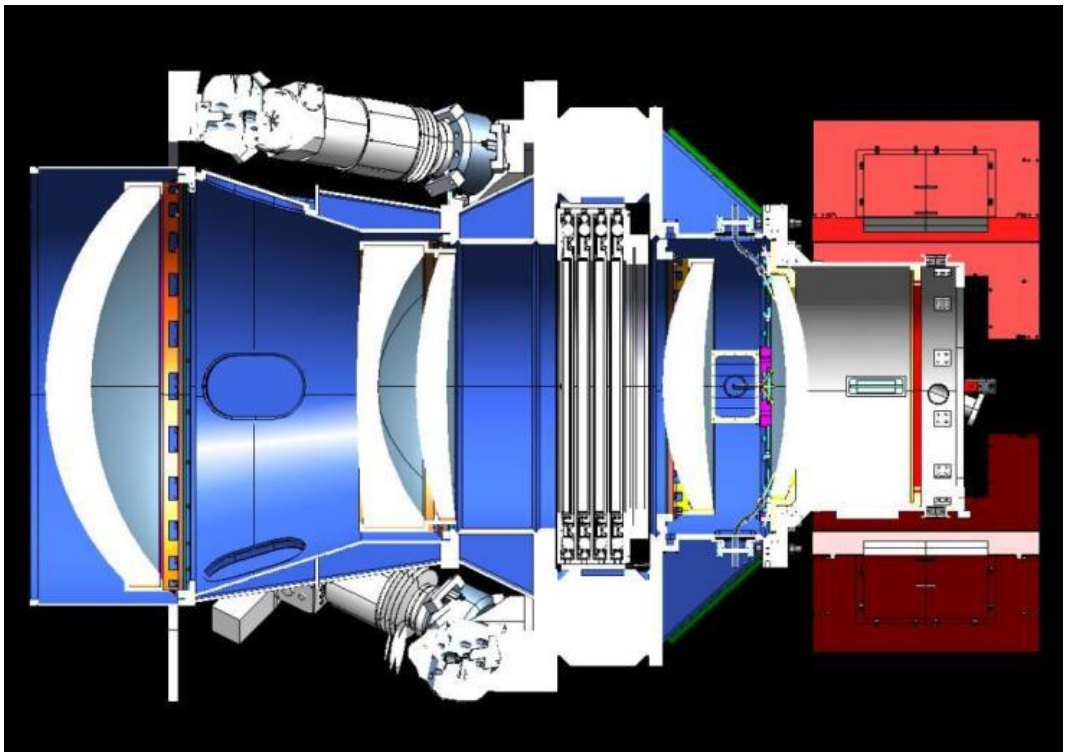

Figure 2.14: Cross-section schematic of the completed optical corrector. The primary mirror is to the left[28].

2.6.3 Lens to cell alignment technique

Dr Brooks designed the baseline concept for the alignment of the lenses to their cells[47], using the mechanical method of clocking the lenses within the respective cells. Clocking is where the element is aligned to a rotational centre through the minimising of its run out. To create a rotational centre a rotary table is required. This needs to be at least a metre in diameter, and able to take a two tonne load in order to fully support DECam. The run out on the table cannot be more than a few microns to avoid this affecting the alignment of the lenses. Movement in the X and Y directions will be by linear rails set at 90° with respect to each other mounted on flat plates. Mounted screw threads will adjust these plates over a range of about ±25mm. Movement in the Z direction is achieved via multiple bottle jacks allowing tilt adjustment as well. A schematic of this alignment set-up is shown in figure 2.15. Digital dial gauge indicators (DDGI) will be used to measure the rotational symmetry and the tilt of the lenses and cells. These need to have an accuracy of 1μm and be securely mounted so their support does not affect the readings. The change in run out as the rotary table moves allows iterative adjustment of the lens and cell until a minimal run out is achieved, at which point the cell or lens is aligned with the rotary centre. In order to compensate for wedges in the lens both the top and bottom surfaces must be clocked[47].

The lenses will never touch the cell directly. RTV is used on both the axial and radial surfaces and it is these pads that will define the position of the lens. This allows small variations in the cell surface to be taken up by the compression of the pad. Measurement of the surface created by the pads is difficult due to limited access, and the discontinuous nature of the pads, and so will have to be measured indirectly through the cell.

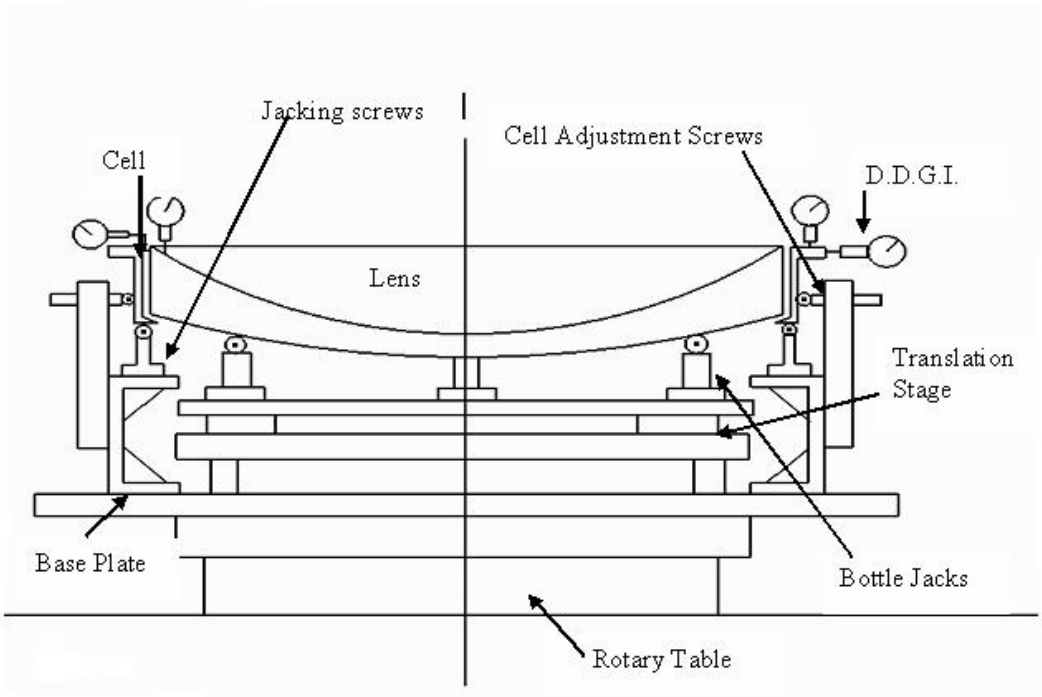

Figure 2.15: Schematic of the alignment rig to be used for the lens to cell alignment[47].

Chapter 3

Production and Testing of Thin RTV Pads

Computers are useless. They can only give you answers.

Pablo Picasso

This chapter discusses the confirmation of the compression modulus of thin pads of the room temperature vulcanising silicon rubber compound, RTV560, as well as the methods developed to control the pad during its construction to ensure its final properties are well defined. Two of RTV560's properties, the compression modulus and the coefficient of thermal expansion, were considered to be especially important. This is due to the fact that the rubber pads will be used in two positions in the cell, each for slightly different purposes. As discussed in Chapter 2 the RTV will be placed on the axial surfaces where the compression of the pad becomes the driving factor of the pad size. When it is used in the radial position the CTE will be the driving force, although the pad must remain stiff enough to avoid the lens shifting as the telescope slews across the sky. The expansion difference between the lens and holding cell was calculated and the thickness of the RTV pad was set such that it expanded to fill this difference, creating an athermal design to reduce the stresses within the lens.

During this chapter pads only a few millimetres thick are used. Two different scenarios were investigated, double glued and single glued. Double glued is where the pad has

been glued to plates on two opposing faces, normally those with the largest surface area. Single glued is where a pad has been glued on a single face, again normally one with the largest surface area. The glue used is the RTV560 solution, the same material as the pads themselves are made from. By coating glass and metal with an appropriate primer, RTV560 cured on top will bond to the material forming a strong bond[43]. No primer is required for the RTV to bond with previously cured RTV 560.

3.1 Theoretical Modelling of the Pads

As no experimental data was found for the compression modulus of thin pads of RTV560 it was necessary to confirm that the pads followed the expected theoretical results. In order to do this it is first necessary to understand the shape factor, also known as the S factor. The S factor is given by the ratio of the area of the load bearing face to the size of the area that is free of force giving

$$S = \frac{wl}{2(w+l)t} \tag{3.1}$$

where S is the S factor, w, l and t are the width, length and thickness of the pad[12]. When square pads are considered this can be shortened to

$$S = \frac{w}{4t} \tag{3.2}$$

as the width and length are equal. A low S factor gives a pad that has a large height compared to its width and length making it easy to squash. This gives a lower compression modulus as compared to that of a thin but long piece which has a high S factor.

Despite being effectively an incompressible material RTV does appear to compress under pressure. This is due to the rubber expanding out of the unconstrained sides of the pad meaning that the compression modulus changes for a given S factor. It also changes for pads that are glued on a single side compared to those glued on two as the gluing constrains the movement of the pad, as shown in figure 3.1. To model the compression modulus two methods, empirical equations and finite element analysis (FEA), were used. These were then compared to experimentally determined results in section 3.3.

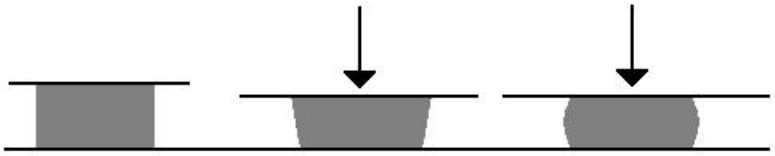

Figure 3.1: A sketch showing the difference in compression between a single glued pad and double glued pad. An uncompressed pad is on the far left, the middle pad is glued on the bottom allowing the top of the pad to expand out as it is compressed and the far right pad is glued on the top and bottom surfaces so the RTV is forced outwards at the middle as it compresses.

3.1.1 Empirical modelling of the pad compression

During the construction of the MMT, Fata and Fabricant empirically calculated the compression of RTV11[48], this technique has been copied for RTV560. The simplest equation is for finding a pad's compression modulus, E_C, when it was glued on two opposing faces is given by[49]

$$E_C = 3G(1 + 2S^2) \tag{3.3}$$

where G is the shear modulus of the RTV560 and S is the pad's S factor. When only one face has been glued the equation is modified to

$$E_C = \frac{10}{9} E_0 \left(1 + \frac{5}{8} k S^2\right) \tag{3.4}$$

here k, an empirical constant, replaces the shear modulus and E_0 is the Young's modulus of the RTV[48]. However, neither of these equations takes into account the compression limit of the pad. This starts at 10% of the bulk modulus, E_B, and at this point the deformation due to the bulk compression is no longer negligible. In order to compensate for this in the model a corrected compression modulus, E_C', is found by[49]

$$E_C' = \frac{E_C E_B}{E_B + E_C} \tag{3.5}$$

where the bulk modulus,E_B[48] is

$$E_B = \frac{2(1+\mu)G}{3(1-2\mu)} \tag{3.6}$$

here μ is Poisson's ratio.

Using these equations the compression modulus was found empirically for S factors between 0.1 to 100. This is a much larger range than was modelled for the FEA or experimentally found as the empirical equations only consider the S factor and not the actual physical dimensions of the pad.

3.1.2 FEA modelling of the pad compression

Finite element analysis models of the pads were created as this is the method that was used to refine the opto-mechanical design of the optical corrector, using the software package NX-IDEAS. FEA works by breaking the system being considered down into small elements. The effect of each element on its neighbour is considered and from here it is built up to determine stress and movement of the entire system.

Pads of various sizes were generated. The majority of the pads were smaller than 40mm in width or 5mm in depth to try and match the physical size of the pads that would be used in the optical corrector. Results were generated over a range of S factors between 0.4 and 50. NX-IDEAS required the input of the Poisson's ratio (0.4995)[42] and a Young's modulus (3000mN/mm)[50]. The models consisted of pads which are placed between two generic steel plates. Two models were generated: one in which the bottom side is bonded and the top side is free; and one in which both the top and bottom sides are bonded. In both cases a force of 100N was applied to the top plate. The deflection of this plate, δ, was calculated by the software and then used in the equation

$$E_C = \frac{Ft}{\delta A} \tag{3.7}$$

where E_C is the compression modulus, F is the force applied to the pad, t the thickness of the pad and A is the area over which the force is being applied[49].

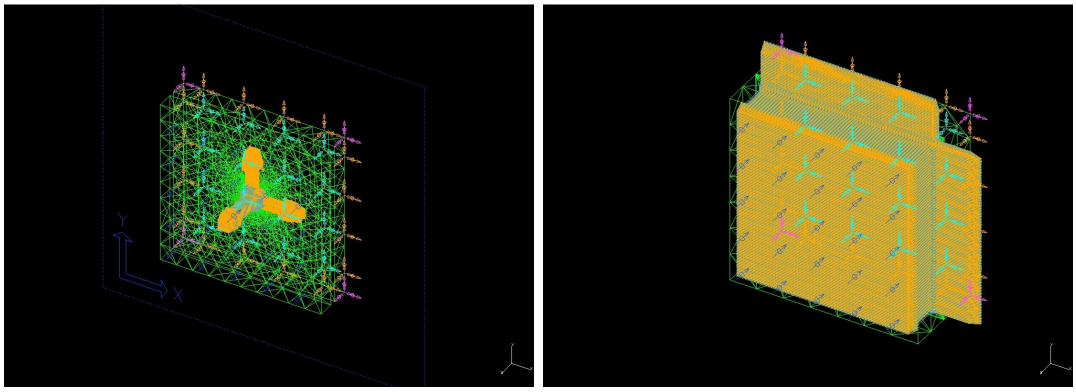

Figure 3.2: Screen shot from NX-IDEAS showing the model of a pad with the conditions that it has been placed under when glued on opposite faces. The arrows show constraints on the surfaces and the lines are the mesh grid that the FEA is computed over. The left hand figure shows a S factor of 0.4 and the right hand figure shows a S factor of 50.

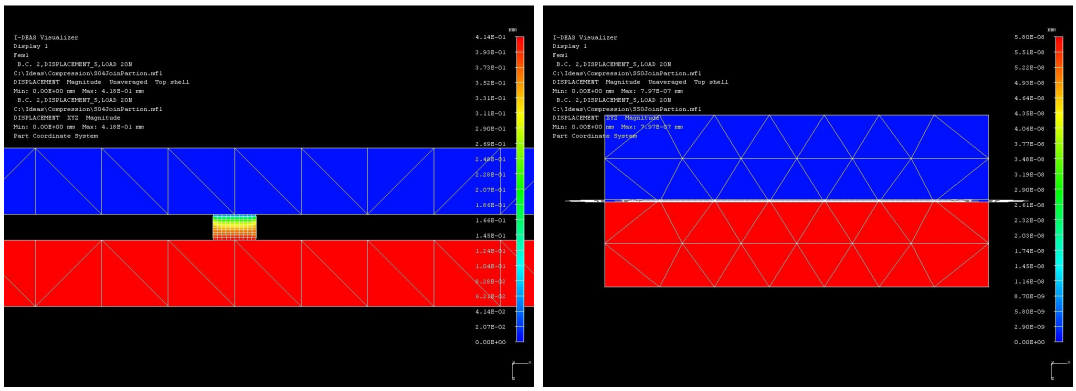

Figure 3.3: Screen shot from NX-IDEAS showing the wire frame model with the solution of the constraints shown in figure 3.2. Here the colours represent the amount that the pad and plates have moved when a force of 100N has been applied to the top plate. The left hand figure shows a S factor of 0.4 and the right hand figure shows a S factor of 50.

3.1.3 RTV pads in tension

The strength of the RTV under tension is dependant on the S factor as well as the cross-sectional area, A, and the shear modulus, G[49]. If the tensile force, F, that is applied satisfies the following when S > 2

$$F = \frac{3AG\left(1 - \frac{1}{S}\right)}{2} \tag{3.8}$$

then the force is insufficient to cause internal flaws. For pads where S < 2 then the equation

$$F = \frac{3AG}{4} \tag{3.9}$$

must be met. A previous study[48] performed destructive testing on pads made from RTV560 and found that the pad failed before the bond.

In the DECam design only the radial pads will be glued to both the lens and the cell. Therefore it will only be the radial pads that will undergo a tensile force. These pads have a range of S factors between 5 (on C3) and 16 (on C2). This means that the expected force required to cause internal damage to the pad ranges from 597N for C3 and 9220N for C2. The heaviest lens is C1 with a weight of 173kg which is distributed over 12 pads. Unsupported this would give a force of 141N per pad, much less than the failure force of 3907N. This supports the FEA modelling done on cells C2 and C3 for earthquake testing, that showed minimal movement when a load five times that of gravity was applied to it.

3.2 Experimental Method

RTV pads were produced to confirm the theoretical models; again these were of similar sizes to those in the optical design. The pad sizes tested ranged from 3.6 x 12.51 x 13.73 mm, giving an S of 0.91 to 0.7 x 27.5 x 27.5 mm, with an S factor of 9.82.

3.2.1 Construction of pads

The first stage in experimentally testing the compression modulus was to cast pads in a variety of S factors. As the compression modulus is dependant on the ratio of the lengths of the sides of the pads, all the pads were cast as squares for ease of construction and calculation. S factors of 0.91 to 9.82 were tested. Lower S factors were difficult to test due to the small size of the pad. Larger S factors would compress by amounts less than could be measured.

The original method as inherited by the author used a pad casting mould much larger than any pad size required, shown in figure 3.4(a). A lid with two holes allowed the excess rubber to escape and changeable spacers between the mould base and lid controlled the thickness of the produced rubber sheet. The thickness of the pads was then set by the use

of spacers between the mould base and the lid. The RTV560 was mixed with a catalyst, required for the viscous RTV to set, placed in a vacuum chamber to outgas until all the air had been removed from the rubber solution and finally poured into the mould. After curing for 24 hours the RTV could then be cut up into pieces of the required size using a specially constructed cutting board, shown in figure 3.4(b), that can be adjusted using a micrometer to allow accurate sizes of pads.

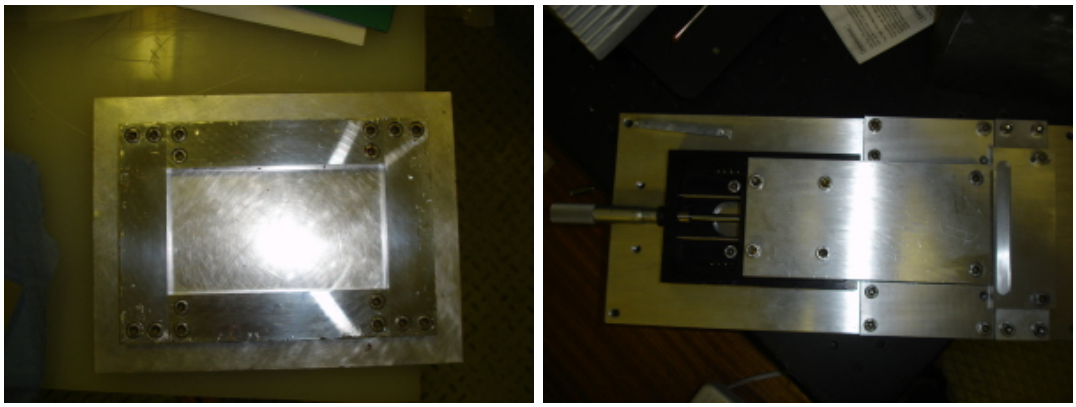

Figure 3.4: The mould, shown on the left, was used to create sheets of RTV at a set thickness. On the right is the cutting board used to cut the RTV sheet to the size required for the pads.

To attach the RTV to stainless steel square plates a primer was painted onto the plates. Once this has dried into a white powder layer RTV can bond to the metal as the RTV cures. Uncured RTV naturally bonds to cured RTV and so no primer is required to on the RTV pad although the surface glaze must be removed with acetone or similar[48]. Pads of the same size were bonded to a single piece of metal and also bonded between two metal plates, creating a single and double glued set of RTV pads. The glue layer was kept as thin as possible because, once the pads has been glued on two sides, measuring the new pad thickness becomes difficult. The top plate was smaller than the bottom plate allowing ease of access of gauges to measure the movement of both plates.

3.2.2 Method used to determine the compression modulus

The completed pad between the plates was placed under a load gauge as shown in figure 3.5(a). Two digital dial gauge indicators (DDGIs) allowed the movement of the top and bottom steel plates to be recorded. It was necessary to measure the base plate's movement as the total amount of movement was often a few microns, at which point any compres-

sion of the support or trapped dust caused a significant variation in results. To increase accuracy the compression stiffness, K_C, was used where

$$K_C = \frac{F}{\delta} \tag{3.10}$$

allowing the gradient of the graph of the force versus the deflection to be used to reduce measurement errors. A typical graph used to determine the compression stiffness is shown in figure 3.6. The experimental results did not produce completely straight lines, with occasional cases where the RTV pad appeared to 'expand' as the force was increased. It is believed that this was caused by working close to the accuracy limit of the DDGI and so small slippages or vibrations could cause the readout to change. Where there appeared to be multiple gradients on one graph subsections were taken, as in figure 3.7, and multiple gradients from each graph were averaged to determine the compression modulus.

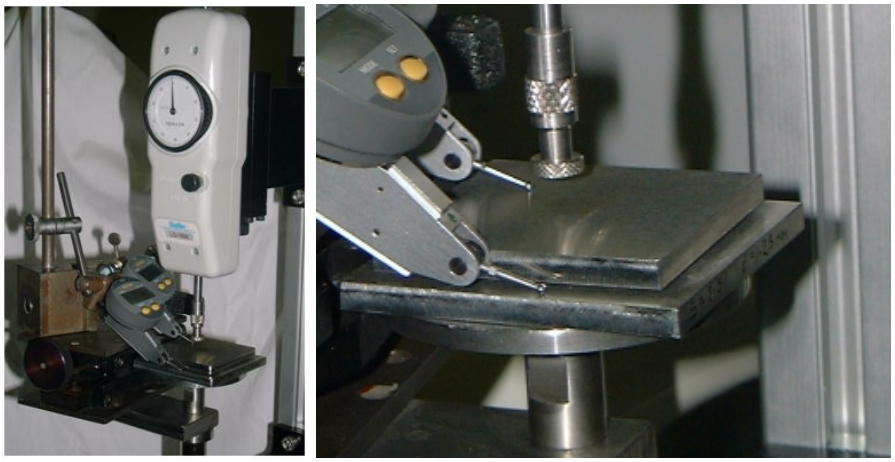

(a) (b)

Figure 3.5: Setup of equipment used to measure the compression stiffness. The left hand panel shows the metal plates underneath the load gauge with two DDGIs. The right hand panel shows a close-up of the metal plates used. The pad is glued between the centre of these two metal plates.

3.2.3 Difficulties encountered

There were several difficulties that were encountered during the deflection measuring process. The most significant error came from being near the measurement limit of the DDGIs. Despite having a resolution of 1μm their repeatability was not always to this limit, often being nearer 3μm, giving the start position to be 2 or 3μm different from

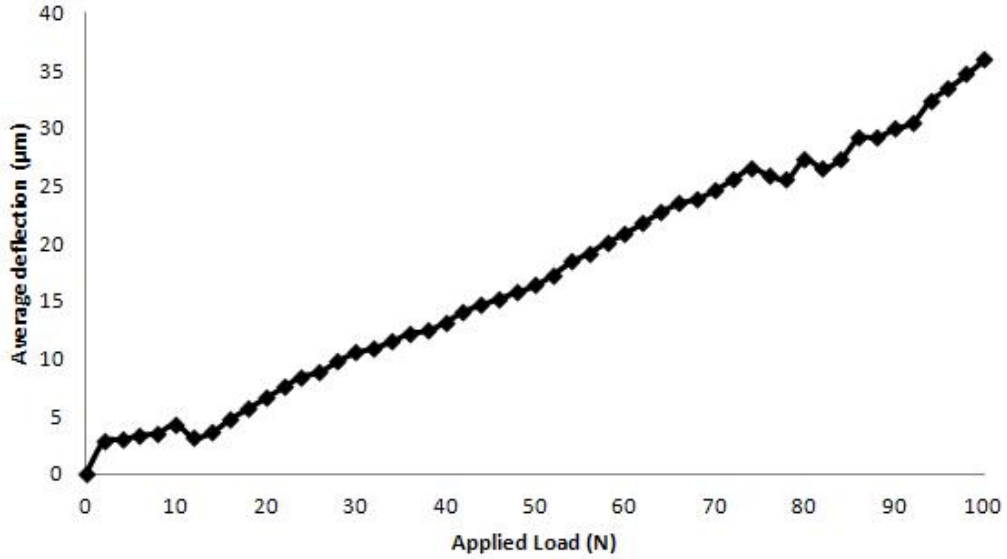

Figure 3.6: Typical deflection versus force graph. This shows the average result over five compression cycles for a single glued pad with an S factor of 3.11. The averaging can cause features in the data where the pads appears to expand. To try and remove these, the gradients are taken where the graph seems most linear and then averaged once more.

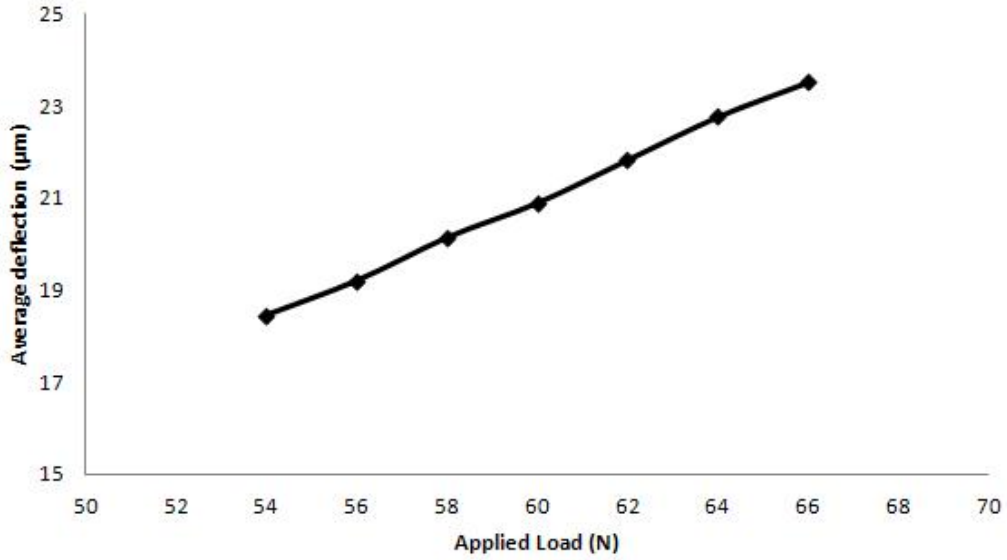

Figure 3.7: A linear zone in the compression stiffness between 54 to 66N for a single glued pad with and S factor of 3.11. Multiple compression stiffness's are used to find the average to be used to calculate the compression modulus.

its original measurement. This effect became more pronounced as the pads got stiffer, a problem as these pads also had the least movement in them, sometimes calculated to be under 10μm. For a double glued pad with an S factor of 9.82 the expected deflection was 0.3μm, which is undetectable by our system. This leads on to the next problem which is that a deflection was being seen here. This was thought to happen due to a larger and thinner the pad being harder to glue flat. A flat surface is essential so that the force is applied evenly over the surface; otherwise the higher areas compress first, giving a lower than expected compression modulus.

Another difficulty came from placing the plates squarely on the pad to prevent them naturally resting at an angle. The smaller the S factor of the pad, the smaller the surface area of the pad and the more likely it was for the plate to be resting at an angle. This held true for both single and double glued pads. However, it was determined that a small wedge is easily tolerated and has little affect on the compression modulus. Although the pad will initially compress more, it will rapidly level out. By rejecting the very start of the measurements, the same compression modulus is found. Rotation of the plate to present a different area to the DDGI did not affect the results. The variation between readings was no different to that found between repeated measurements. Gluing tools were created for the DECam axial and radial pads to ensure that a flat and even glue layer was created. These were weights that conformed to the radii of each axial surface or insert, helping to spread out the glue over the entire pad, reducing the risk of air gaps and an uneven glue layer.

The cutting board did not produce completely repeatable pads, due to difficulties in ensuring a straight cut. It was easy to angle the razor blade giving a non-square pad. If not enough force was applied it would not cut all the way through the pad, ripping the last part. For pads that were longer than the length of one razor blade, approximately 5cm there was an additional problem in that cuts would not be to exactly the same position, giving jagged edges. In order to ensure uniformity of the pads used in DECam individual moulds were created for each pad size required. This meant that each pad was of the same size and had square, straight edges.

3.3 Comparison of Results

The experimental data was plotted against the theoretical results to determine the best estimate of the RTV's behaviour. This plot can be seen in figure 3.8, where the empirical (dashed lines) and FEA (solid lines) models are plotted against the experimental values for both single glued (grey) and double glued (black) pads. There is a slight divergence between the FEA and empirical models. The FEA calculating the double glued pads to be softer, and the single glued pads harder, than the empirical equations predicited. It appears that the experimental results agree more with the FEA predictions, although the large error bars on them do fall within the range of the empirical model.

For low S factors the experimental results appear to be in good agreement with both the empirical and FEA theoretical models. The experimental results for the single glued pads stayed closer to the theoretical values for longer, up to S factors of 6. This compares to the S factors of 3 for the double glued pads, where the measurement limits of the DDGIs are reached. The measurement limits are reached later with single glued pads as the lower compression modulus means the pad compresses more than when its double glued.

At high S values (S = 9.82) the results give a much lower compression modulus than expected. A highly probable cause of this is the thinness of the pads, less than one millimetre thick, with an uneven glue layer, meaning the top plate sits on three high peaks rather than flat over the entire pad. When a load is applied the higher part of the pad is compressed first and, as it is less constrained, it compresses further than expected giving a lower compression modulus.

3.4 Calculating the Radial Pad Size Required

As the axial pad size is set by the compression of the pad, the radial pad thickness is set by the expansion of the pad due to temperature changes. RTV560's CTE is dependent on the shape factor of the pad[13][48][51]. To determine the effective CTE, α, a correction factor, K_T, must be used[48], a graph of which is shown in figure 3.9. This value was then placed into the equation

$$\alpha_{eff} = K_T \alpha_{RTV} \tag{3.11}$$

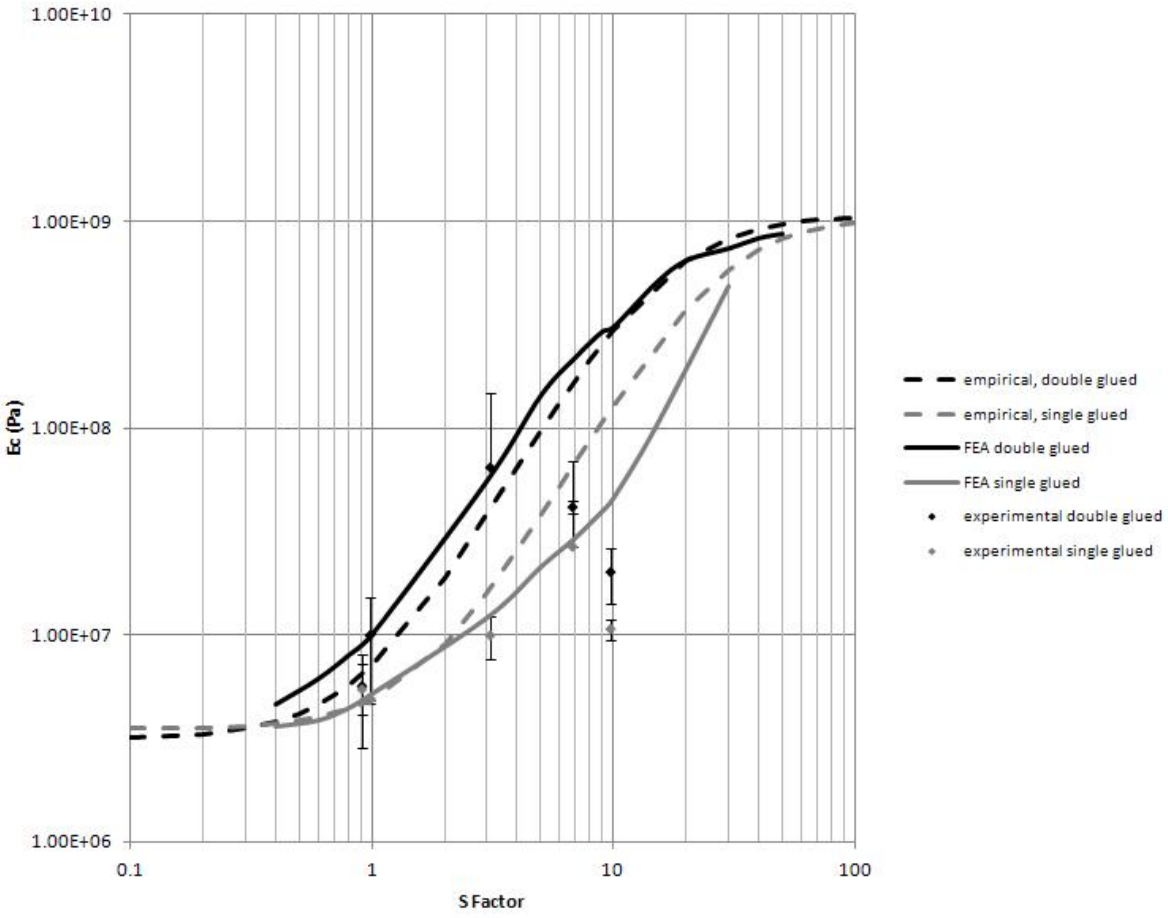

Figure 3.8: Graph showing how the compression modulus of RTV560 varies with a change in the S factor. Solid lines indicate results from FEA, dashed lines give the empirical results and the dots are experimental data. Black denotes the RTV was glued on both opposite sides and grey is where only one side of the pad was glued.

where α is the CTE, to gain the effective CTE of the RTV560. This could then be used to find the required thickness by using[42]

$$t = \frac{R(\alpha_{cell} - \alpha_{lens})}{\alpha_{eff} - \alpha_{cell}}. \tag{3.12}$$

As K_T is dependent on the shape factor, and the thickness is set by the above equation, it is simple to work out the appropriate width and length of the RTV560 pad[42].

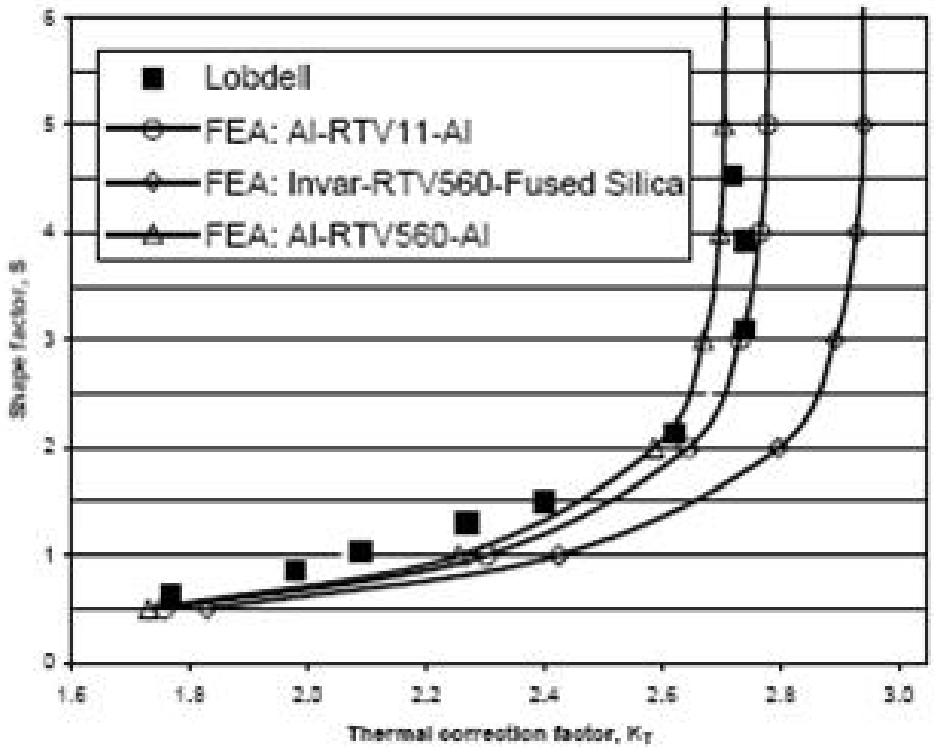

Figure 3.9: Graph of the correction factor required to determine the correct CTE of RTV[13].

As any pad with an S factor of over 2.9 is in the exponential area of the graph, the K_T effectively remains constant. This means that large S factors can be used to gain the high Young's modulus required to reduce the sidewards movement of the lens during operation of the telescope. To allow this S factor to be at a maximum circular pads were decided upon. For a circle the area over which force is applied, πr^2, the force free area is the circumference multiplied by its thickness. If the diameter of the pad is set to equal

the width of a square pad, w, then it is found that

$$S = \frac{\pi(w/2)^2}{\pi w t} \tag{3.13}$$

which can be condensed to

$$S = \frac{w}{4t} \tag{3.14}$$

the same is for the square pad in equation 3.2. This means that to increase stiffness of a pad yet remain within the confines of the inserts a circular pad works well.

3.5 Moulds and Tooling

The original method of creating pads gave great flexibility in the size of the pads created and allowed many different sizes to be used in testing the compression modulus of the material. However the cutting board presented a few difficulties. Although it was controlled by a micrometer this did not compensate for the thickness of the guard, and the razor blade can easily slip at an angle. In addition, several cuts were required to go across the entire strip of RTV560 which results in slightly uneven edges and often angled. The alternative to individual multiple cuts was to drag the razor blade across the RTV but this meant that the strip had a tendency to buckle giving an uneven cut. There was one further disadvantage when cutting a thick pad as the razor blade would not necessary slice all the way through the RTV560 pad and the rest would rip off giving a very uneven edge. The solution to these problems was to create a separate mould for each pad size required, as only a few sizes were needed.

3.5.1 Axial pad moulds

Moulds for the axial pads were created to the required dimensions and had a single open side for escape of the excess glue with the thickness is set to be 100μm smaller than is required to allow for the glue layer. Syringes were used to fill the mould from the bottom, pushing air out in front of the RTV and out the top of the mould so reducing air bubbles with excess being scraped off giving a flat side. Outgassing of the RTV560 is done in the syringe to prevent air being forced into the RTV560 during the process of getting it into the syringe. Photos of the mould created for the C1 axial pads are shown in figure 3.10.

Once the pad has cured it can be removed from the mould. A small amount of trimming is required to get the desired shape. This is a quick and easy process that does not damage the sides of the pads. However there are two disadvantages to this method. Firstly, the moulds need to be made highly accurately and as such they are expensive. Secondly, they cannot be easily adjusted for any changes in the size of the pads so they are very inflexible.

Figure 3.10: The moulds used to create the C1 axial pads. The left hand panel shows a fully assembled mould and the right hand panel shows both an open and complete mould. The RTV560 is forced into the mould through a needle to the bottom of the mould. The top is left open and the excess removed with a razor blade.

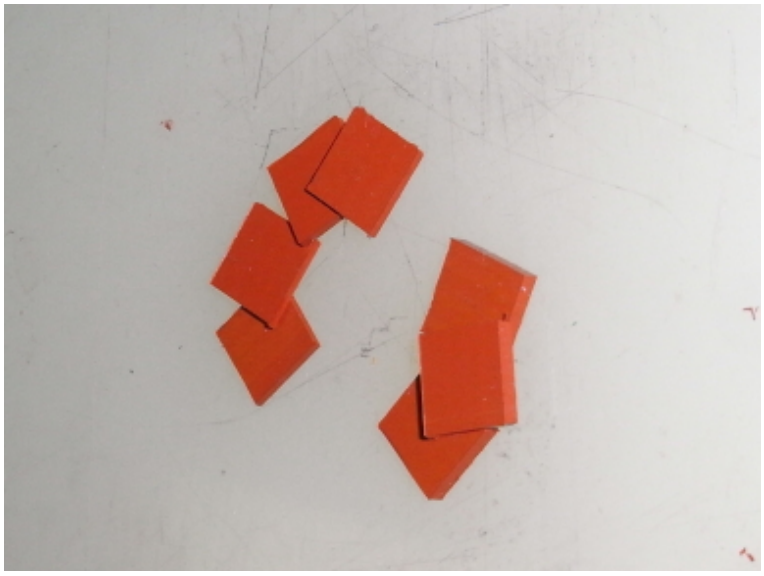

Figure 3.11: Axial pads 0.9mm thick on the left hand side and 1.9mm thick on the right hand side.

3.5.2 Radial pad moulds

The original cell designs had square radial RTV pads but a decision was made to change these to circular pads. The S factor of a circular pad unit radius, a, is the same as for a square pad of width, a. As the inserts are circular, the maximum S factor that can be gained is when the pad is also circular, allowing stiffer radial pads. This reduces the risk of the lens moving as the telescope slews across the sky during operation. The increase in S factor does not affect the CTE as we are in the exponential area of the graph in figure 3.9.

The moulds for the radial pads have a much larger open surface. The RTV is poured in when the mould is lying open horizontally, as shown in figure 3.12. This method was chosen over syringe injecting due to the large quantity of RTV required for a radial pad. Injection is a slow process and the RTV has only approximately 20 minutes from the addition of the catalyst untill it is too thick to pass through the syringe's needle. Testing of the injection method resulted in incomplete pads as the shear volume of RTV required meant that the process took too long. Once the RTV had been poured in, a metal top plate is then pressed down and screwed into place. This forces the excess RTV out through the top of the mould. The mould is then placed vertically, so RTV does not flow out due to gravity whilst it is curing. Once cured the excess spout, seen in figure 3.13, is trimmed from the pad leaving a circle of RTV, as shown in figure 3.14.

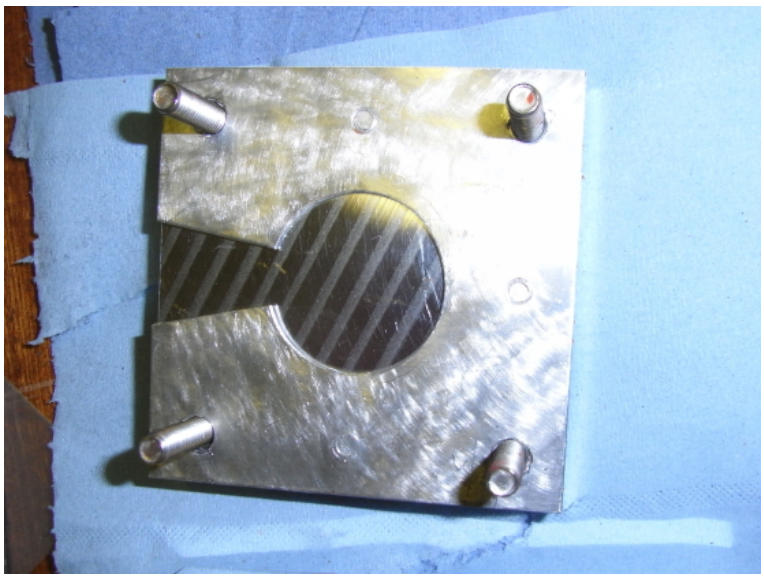

Figure 3.12: An open radial pad mould. A plate is placed on top which forces excess glue out of the spout. Tapped holes in the top plate allow ease of removal.

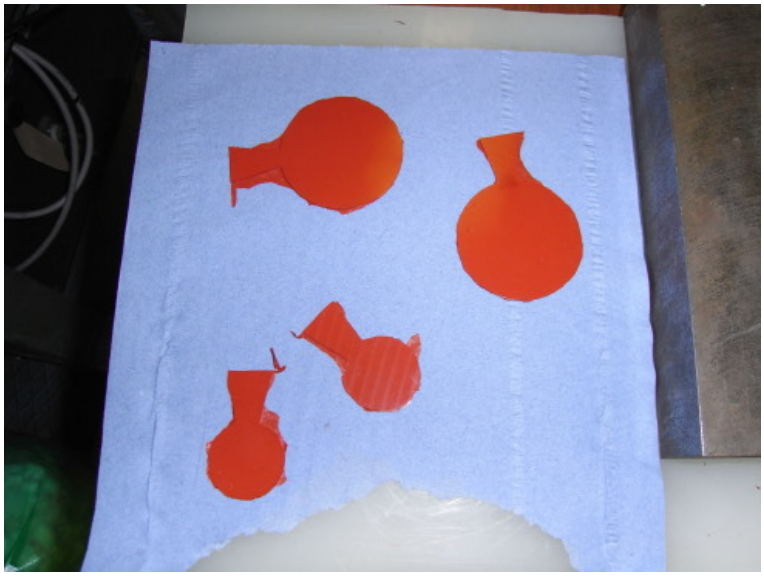

Figure 3.13: Radial pads just out of the mould. The excess stalks must be removed and the edge of the pad trimmed to remove thin excess that slipped between the mould plates.

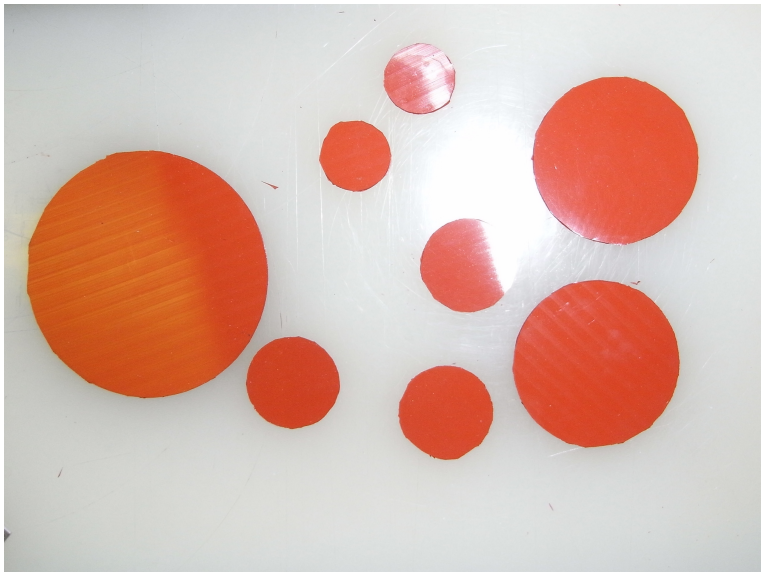

Figure 3.14: Radial pads of various sizes ready for gluing to inserts. The largest pads are for C2, the next largest are for C1, then C4, with the smallest for C3.

3.5.3 Repeatability of pad sizes

The pads were measured as they came out of the moulds to ensure that the moulds were working as intended to give identical pads, the results of which are tabulated in table 3.1. Due to the contact measurement method used it is believed that the width variation measured is greater than it truly is. This is due to the pads being very long and thin and hence bending easily in the width direction. The thickness is a more critical measurement. In the axial direction it controls how the lens sits, and in the radial direction there is a limited gap for the pad between the lens and cell. Pads that are slightly thinner than expected are easily compensated for with an increase in the glue layer thickness. Should the pads be thicker than expected then they must be discarded.

Pad	Designed Diameter/Width	Measured Diameter/Width	Designed Thickness	Measured Thickness
C1	60	59.94 ± 0.25	1.6	1.54 ± 0.02
C2	90	89.64 ± 0.27	1.42	1.15 ± 0.04
C3	25	25.43 ± 0.21	1.34	0.98 ± 0.06
C4	33	33.34 ± 0.31	1.24	1.06 ± 0.1
Axial 1mm	10	10 ± 0.1	0.9	0.93 ± 0.01
Axial 2mm	10	9.96 ± 0.07	1.9	1.92 ± 0.01

Table 3.1: Size of the pads produced by the moulds. Lengths are in mm.

3.5.4 Tooling for axial pads

It was necessary to ensure that the glue layer attaching the axial pad to the sloped surface of the cell was of the correct height and evenly distributed. Any height variation will feed directly through to the lens, possibly adding a tilt across it or giving an uneven stress distribution. To guard against this tools were made with the same cone surface as the sloped axial surface, cut through with a slot of the same width as the axial pad and with a depth of the final height of the pad. This meant that each cell had to have its own tooling. Figure 3.15 shows this glue tooling for the C3 cell, with a pad in each gluing tool. Precise machining meant the pad was held in position whilst being glued and the repeated use of the tools gave repeatable results around the cell. Syringes were used to put a calculated amount of glue onto the pad where it was spread out to ensure an even glue coating.

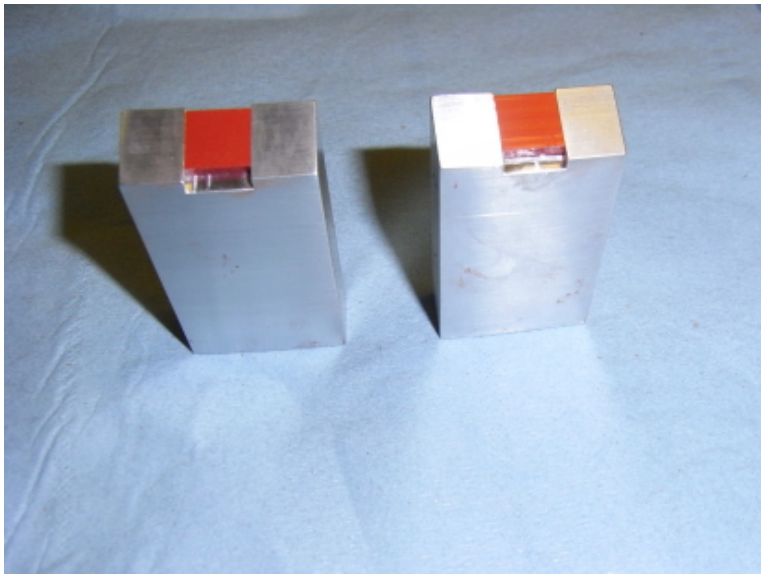

Figure 3.15: Height tooling for the C3 axial pads. The pads are in place and required the glue layer to be added before placing on the cell.

3.5.5 Glue layer repeatability

To determine the repeatability of the glue layer from the gluing tools, pads were glued onto a flat metal plate using the C2 tool. Due to the angled surface on the C2 tool thee tilting rotary table was used to place the plate at the correct angle. Once the pads had been glued into position, they were passed under a laser displacement sensor to determine their height. Sample 1 and sample 2 were measured at 90° with respect to each other.

The output from the laser probe is shown in figures 3.16(a) and 3.17(a), where the plate is just below 1.6mm from the sensor and the two downward drops are the two pads glued to the plate. They appear as dips due to the laser displacement sensor measuring as a distance away. Here it was placed above the sample plate and so as the pad rises it gets nearer the sensor, reducing the recorded distance. Figures 3.16(b) and 3.17(b) shows the plate was not aligned perfectly with the laser gauge and was being brought through its measurement range at an angle. Figures 3.16(c), 3.17(c), 3.16(d) and 3.17(d) are close-ups of the pad surface variation. The straight lines show the fit to the averaged position, giving a nominal flat. In general the pads do not vary more than $\pm 20\mu$m from their nominal flat.

3.6 Summary

From the work presented in this chapter three main conclusions can be reached. Firstly, the FEA models of the opto-mechanical design reflect the likely movement and compression

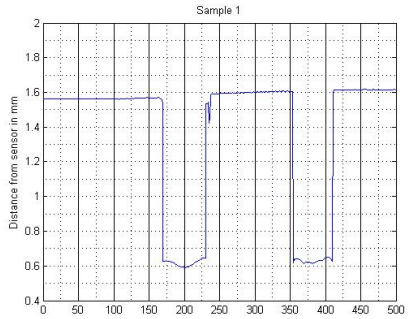

(a) Height variation across sample 1 where the data is being taken perpendicular to the direction of the lens' radius.

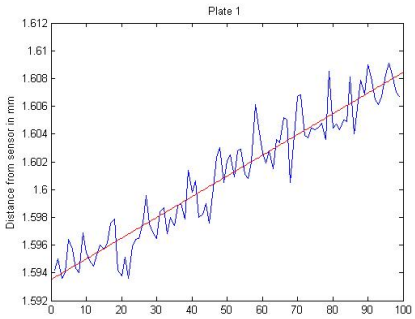

(b) Height variation in the sample plate

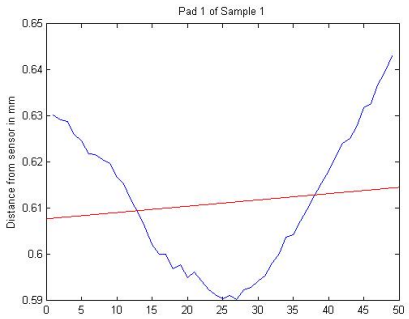

(c) Height variation across the first pad

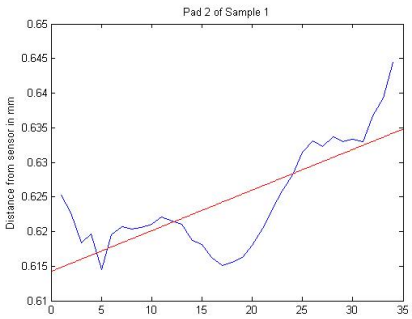

(d) Height variation across the second pad

Figure 3.16: Height variation in the glueing test of sample 1

of the RTV pads. Secondly, pads of the same dimensions can be reproduced, giving the same physical properties. Finally, these pads can be glued to the sloped axial surface in a repeatable and even manner.

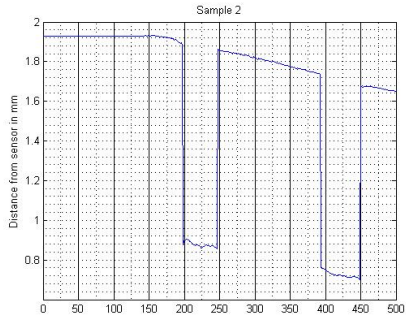

(a) Height variation across sample 2 where the data is being taken along the direction of the lens' radius.

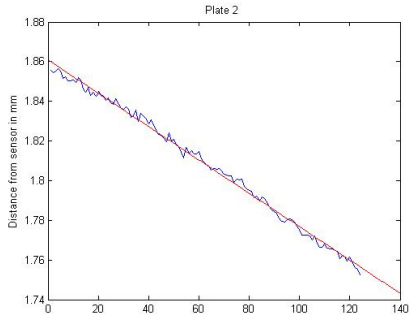

(b) Height variation in the sample plate

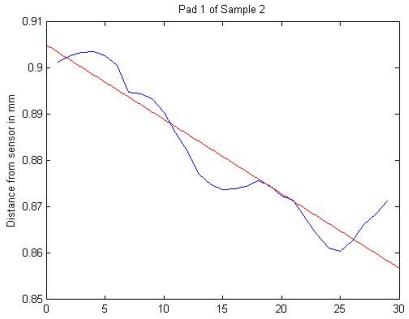

(c) Height variation across the first pad

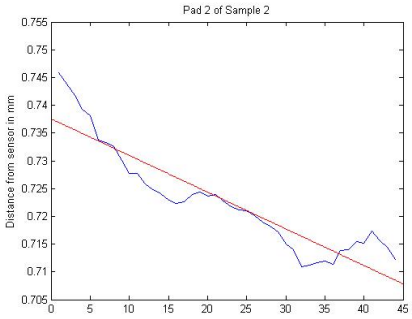

(d) Height variation across the second pad

Figure 3.17: Height variation in the glueing test of sample 2

Chapter 4

Composition and Metrology of the Lens-Cells

The problem with troubleshooting is that trouble shoots back.

Unknown

In this chapter the co-efficient of thermal expansion of the cells is discussed with particular reference to the chemical composition. The detailed metrology of the cells is reported, in particular the circularity of the cells and the mating rings is documented, along with the flatness of the sloped axial surfaces. The final section discusses the work performed at the Fermi National Accelerator Laboratory to align the cells to the barrel.

The production of the cells was contracted out to two companies, Jennings Winch and Foundry, and Ashby Precision Engineering. Jennings cast the cells, a picture of a cell just removed from the cast is shown in figure 4.1, and rough turned them. Figure 4.2 shows a cell just after rough turning. The cells were then sent for X-ray, an example of which is shown in figure 4.3, in order to ensure that no voids were present in the material. This is especially important in the region of the flexures, where a void would create significant structural weakness. Once approved, the cells were sent to Ashby's for fine turning to be formed into the final cell, shown in figure 4.4.

Figure 4.1: A cell after casting.

Figure 4.2: A cell after rough turning.

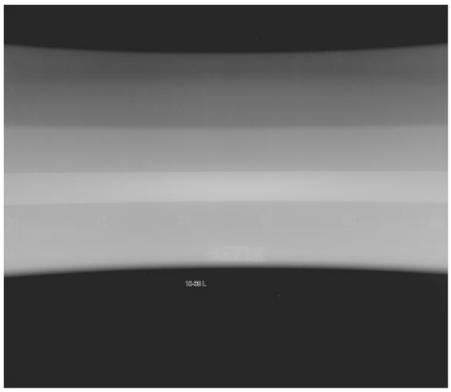

Figure 4.3: A X-ray of the cell after rough turning, showing no voids in the material.

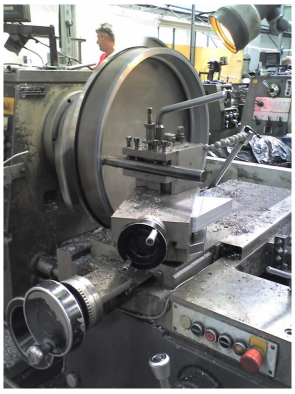

Figure 4.4: A cell undergoing fine turning.

4.1 Testing of the Prototype Cell

To confirm the production techniques and the mechanical design of the DECam lens-cells, a prototype cell was produced. The prototype cell had an inner diameter of 540mm, smaller than DECam cells, but sized to hold a pre-existing lens at UCL. Initally a CTE test was performed on a sample piece of material from the prototype. This was done by heating the sample on a hot plate to 150°C and measuring the expansion using a micrometer. The change in length was used to determine the CTE, α, by the equation

$$\alpha = \frac{\Delta L}{L \Delta T} \tag{4.1}$$

where L is the original length and the change in the length is ΔL. The change in temperature is ΔT[44]. The expansion of the micrometer was calibrated out using the apparent

expansion of a piece of Cervit, a material with an effective CTE of zero over the same temperature range. The expansion of the prototype sample was measured to be approximately 13ppm/K, whereas the expected value was 2.8ppm/K. This result was checked with a piece of Aluminium 5083 with a known CTE of 23.8ppm/K. It was measured to be 26ppm/K which, whilst still higher than expected, is significantly closer to the expected value than the discrepancy found in the measurement of the prototype material.

In order to determine where the CTE measurement discrepancy came from a chemical composition test was performed. This was done using a scanning electron microscope (SEM) machine. When the electron beam hits an atom, an inner shell electron can be expelled, causing an outer shell electron to drop into its place. This process will emit an X-ray. These X-rays are then characteristic of the composition of a sample and the abundance of elements in it. From figure 2.10 in chapter 2 the required composition to give a CTE of 13ppm/K would be approximately 28% Ni with the remainder iron. The actual composition was found to be 30% nickel, as shown in table 4.1, explaining the high CTE. This highlighted the importance of checking the material composition and this was performed on all the subsequent cell material.

Material	Fe	Ni	Si	S	Cr	Mn	O
Actual Values	56	30.1	0.7	0.7	10.2	1.1	1.2
Values Requested	62	38	0	0	0	0	0

Table 4.1: Results from chemical composition testing of the prototype cell material. Composition test was done at the Archaeology department, UCL.

As well as having a low nickel content there was also a surprising amount of chromium (10%)in the material as well. It is not known why this is present as the requested mix only contained nickel and iron. A screen shot from the SEM program is shown in figure 4.5 where the chemical composition is determined over the boxed area. The darker areas are inclusions, where the material is higher in impurities. It is not believed that these inclusions will adversely affect the performace of the material.

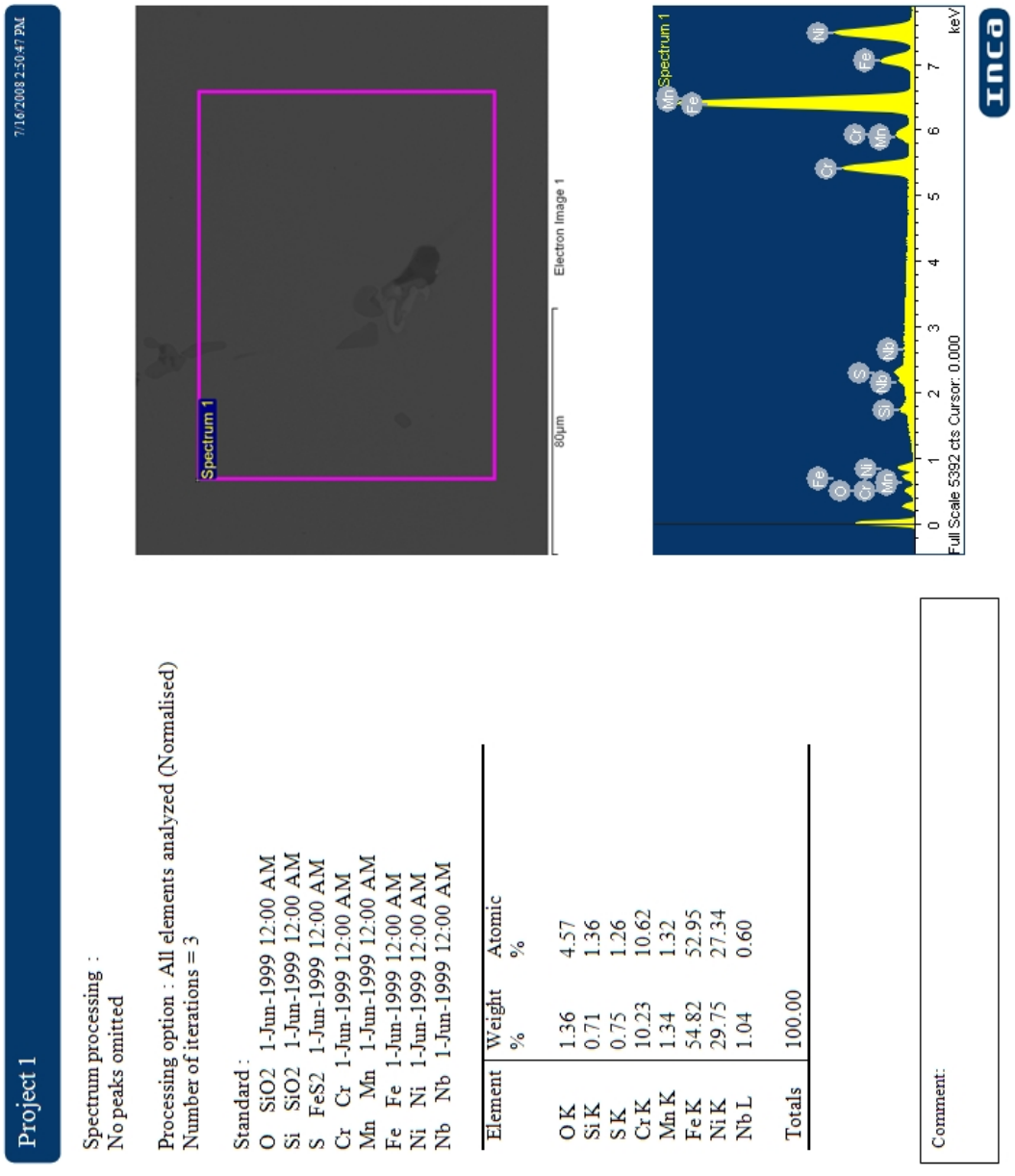

Figure 4.5: SEM spectrum data of the prototype cell showing the unexpected composition readings, averaged over a large area.

4.2 CTE of the Nickel-Iron Cells

The final CTE of the nickel-iron mix is not completely defined by the chemical composition. Previous studies[52] have shown that different heat treatments give slightly different CTE results in the final material. In order to ensure a final CTE of 3ppm/K (parts per million per degree Kelvin) in the cell three annealing techniques were tried on test pieces, hereby referred to as Block 1, 2 and 3. Block 1 was heated for 1 hour at 850°C and then heated for two hours at 730°C. It was then oven cooled and reheated at 315°C for two more hours; it was then either air or oven cooled. Block 2 was heated for 30 minutes at 830°C and air cooled. It was then heated for one hour between 315°C and 371°C. It was air cooled once more and then heated for 48 hours at 95°C. Finally the block was air cooled for a final time. Block 3 was heated for 30 minutes at 290°C and then water cooled. It was then heated for 1 hour at 315°C air cooled and then heated for between 24 and 48 hours at 95°C. All blocks started out with a CTE of 3.2ppm/K and the CTE of all the blocks dropped after the annealing treatment. Block 1 dropped to 2.8ppm/K, Block 2 to 2.3ppm/K and Block 3 to 2ppm/K. These results influenced the final method chosen for the production of the cells, in order to create a method that would produce a CTE of 3ppm/K. The process used was to heat the cast nickel-iron mix to 850°C in an oxygen-free environment and then oven cooled, also in an oxygen-free environment.

4.3 Chemical Composition of the Optical Corrector Cells

Samples of the lens-cell material underwent the same SEM chemical composition tests as the prototype material. Results were taken in both the Wolfson Archaeological Science Laboratories (UCL) and the Earth Science department (UCL). Carbon was removed from the results taken at UCL, as it was not possible to tell if the carbon was an impurity in the sample or came from contamination during the sample preparation process. For all results taken at UCL spectra were taken at several points and the mean value used. However, during the chemical composition testing at UCL the images of the material's surface were found to be covered in inclusions where there was low amounts of nickel and very high amounts of silicon. Data from these inclusions were not used in calculating the mean averages. The error on the SEM measurements is approximately 1%. Samples were taken whilst the cells were at the casting firm, Jennings Winch and Foundry, before they were sent for the milling. One sample set was sent to an outside firm called Exova

for independent testing and a second sample was sent to UCL. Table 4.2 summaries the findings of the chemical composition tests.

As two different machines were used for chemical composition testing at UCL, a sample piece was run to check that the machines were giving the same result. A difference of 1% was found in the nickel content and a 0.16% difference in the silicon content. This was considered to be within the measurement errors. For the C4 insert material chemical testing by UCL was done on a casting sample rather than from the insert material itself. The nickel content showed a difference, with Exova's results being 1.7% larger. The UCL results were trusted on the bases that UCL's chemical composition test matched the CTE results. Screen shots of the SEM results for the C4 cell material are shown in figures 4.6 and 4.7. Figure 4.6 shows the average chemical composition over the boxed area including a few inclusions, figure 4.7 was taken at a single point over the inclusion to illustrate the impurities in the metal.

Cell	Material Company	Fe	Ni	Si	S	Mo	Cu	C	Cr	Mn	P
C1	Exova	Base	37.2	0.09	0.045	0.02	0.05	0.05	0.04	0.05	0.01
C1	Archaeology	61.84	37.73	0.36							
C2	Exova	Base	38.9	0.17	0.018	<0.01	0.01	0.026	0.03	0.05	<0.005
C3	Exova	Base	38.4	0.55	0.045	0.01	0.06	0.014	0.05	0.19	<0.005
C4	Exova	Base	39.4	0.03	0.2	0.04	0.03	0.01	0.02	<0.01	<0.005
C4	Exova	Base	38.6	0.02	0.031	0.02	0.03	0.013	0.03	<0.01	<0.005
C4	Archaeology	61.64	37.82	0.47							
C4	Earth Science	59.39	38.96	0.31							
C4 insert	Exova	Base	39.9	0.02	0.01	0.01	<0.01	<0.01	0.02	0.02	<0.005
C4 insert	Archaeology	62.74	37.14								

Table 4.2: Results from the chemical compositions testing of the cells by percentage weight.

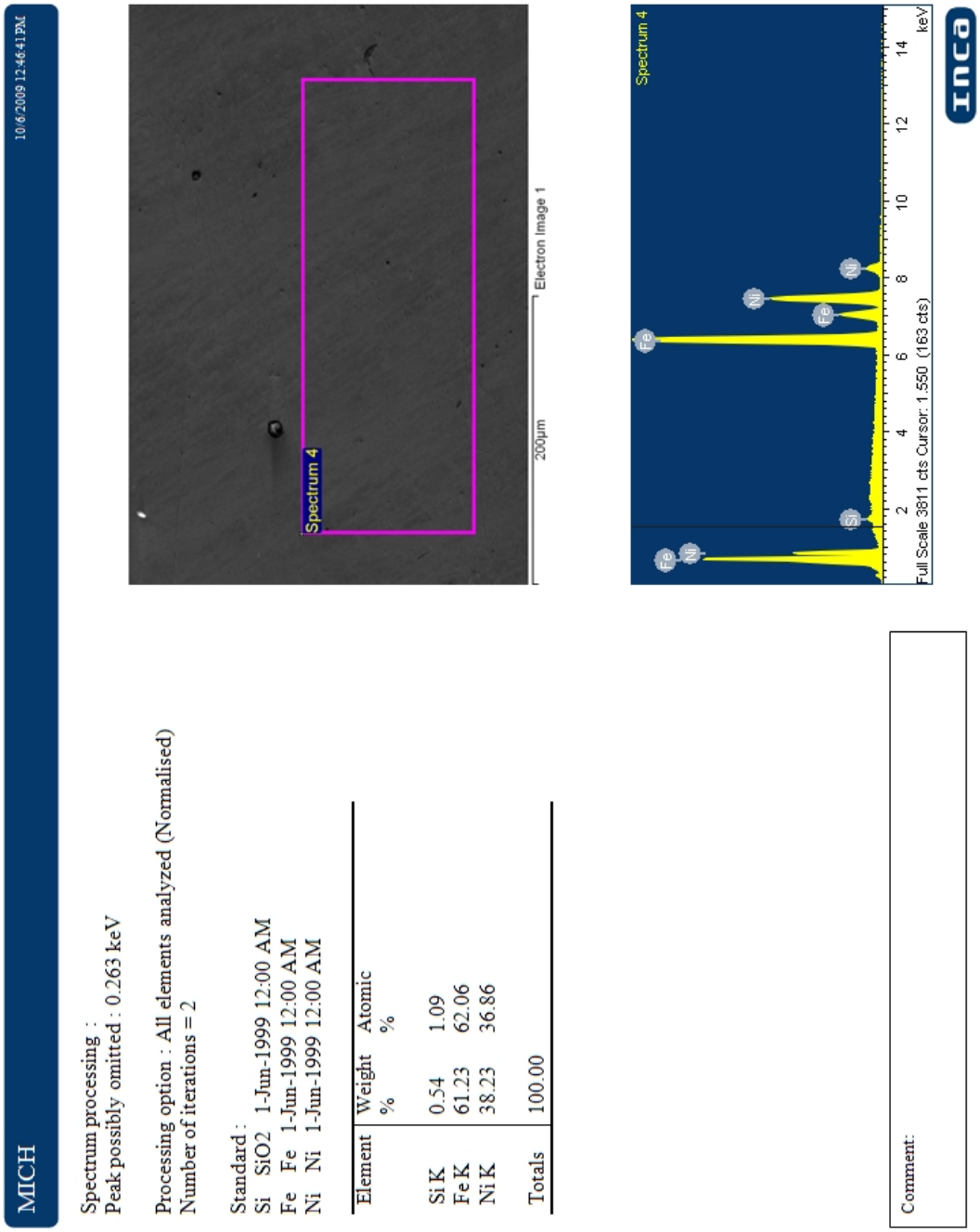

Figure 4.6: SEM spectrum data of the C4 cell material showing the average composition of the material inside the box.

Figure 4.7: SEM spectrum data of the C4 cell material showing composition at an inclusion.

4.4 CTE testing of cell material

CTE tests were performed at UCL using the same samples provided for the chemical composition testing. This caused some difficulties with measurements, due to the small size of some of the samples, as they often came from the holes required for the inserts. Whereas for the chemical composition testing a sample size 1cm cubed was required, for the CTE measurements a sample between 25 mm and 50 mm in length was needed. Any sample smaller than 25mm and the change in length would be too small to determine the CTE. It was not possible to measure lengths beyond 50mm.

The CTE of C1 was found to be 3.1ppm/°C, as measured at UCL on a hotplate. To check the accuracy of the CTE measurements at UCL the C1 sample was sent to the National Physics Laboratory for testing of the material's thermal expansion. Their result for the CTE was found to be 2.70±0.06 ppm/°C. The CTE of the insert material for C2 was measured to be 3.2 ± 0.3ppm/°C. The CTE of the insert material for C4 was found to be 2.8 ± 0.4ppm/°C.

For C2 and C4 a reliable CTE was not able to be found due to the size of the sample. The sample's change in length due to temperature change was within the measurement error, giving highly variable results. The insert material to be used in C1 and in C3 also failed to give a reliable CTE. This was due to the small size of the sample, meaning that the change in size of the material due to the temperature change was within the measurement error. No sample of the C3 cell was sent to UCL. Due to time constraints and the acceptable chemical composition results by Exova, it was decided to accept the material.

4.5 Cell Measurements and Retaining Ring Alignment

The references for the metrology are provided by four surfaces on the cell. The axial surface (A in figure 4.8) is the key surface, as it is the surface that the lens will sit on. Variations in this surface will cause the lens to tilt and also distribute its weight unevenly on the pads. To avoid any decentre in the lens the central axis of this surface should be aligned to the rotational axis of the barrel. The retaining ring contains the remaining three metrology surfaces (B, C and D in figure 4.8). The ring needs to be flat as this is the surface that will be bolted to the barrel. Any distortions in this surface will transfer into the axial surface when bolted and so distort the lens. The ring is also required to be

circular, with its central axis down the centre of the barrel. The inner diameter of the ring is used to align the cell to the barrel and the outer diameter is used to align the cell to the lens. The radial inserts are milled individually and so can compensate for non-circularity in the cell.

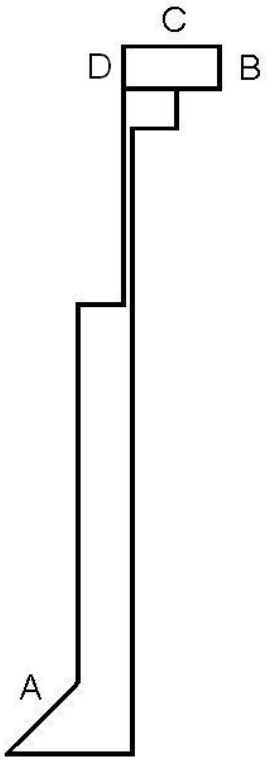

Figure 4.8: Cross-section of the C1 cell showing the four surfaces that are required for the cell to lens and cell to barrel alignment. A is the axial sloped surface that the lens will rest on. This surface must be flat to avoid tilting the lens and aligned to the rotational axis to prevent a decentre of the lens. B and D are respectively the outer and inner diameter of the retaining ring, which must be centred to the rotational axis to ensure that there is no decentre of the lens. C is the top of the mating ring, which is the interface surface between the cell and the barrel. When being mated to the barrel this surface will be forced flat, so any distortions may travel down to the axial surface.

The cells were delivered to UCL in two parts; the nickel-iron holding cell and the steel mating ring. These parts were measured at UCL to ensure they complied with our specifications and were then aligned with each other and bolted into position. No coordinate system was used, only a direction, either clockwise or anticlockwise which was arbitrary. This was kept constant by marking the cell, as only relative distances could be measured. Digital dial gauge indicators (DDGIs) were used to measure the

cells. The measurement accuracy of these instruments is 1μm, although repeatability of measurements was of the order of a few microns. Despite errors bars not being shown on the following graphs made at UCL (figures 4.9 to 4.32, data came from repeated readings and the values should not trusted to more than $\pm 3\mu$m.

The alignment of the cell to mating ring is important because a decentre of the cell will be seen as both a tilt and decentre by a perfectly aligned lens; due to the lens sits on the sloped axial surface. This arises when the mating ring and cell's centres are different. At a given radius from the mating ring's centre a different height on the sloped surface will be reached. This will result in an apparent tilt to the lens when it has the same centre as the mating ring. However, this can also be used to deliberately place a tilt on the lens, of the same size as the lens' wedge, allowing the back surface to sit parallel to the mating ring if required.

4.5.1 C1 Cell Measurement

Initial measurements of the C1 cell found that the sloped axial surface has an unusable height variation of over 1mm, as shown in figure 4.9. Due to this it was returned to the manufactures to be re-milled.

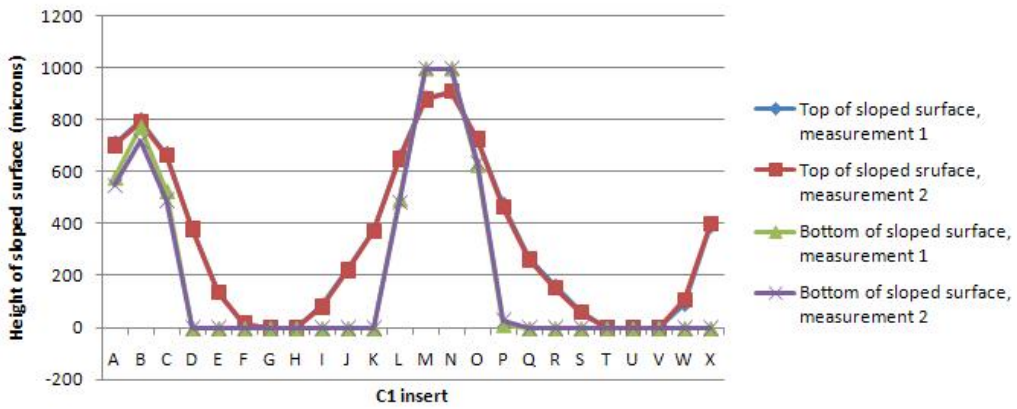

Figure 4.9: The original height variation in the C1 sloped axial surface when the cell was first delivered. The maximum range of the measuring device used was 1mm, causing plateaus at both the peak and trough of the graph as the cell went out of range of the DDGI. The results for the top of the sloped surface's first measurement (blue line with diamond) cannot be seen due to the second measurement (red line with squares) overlaying them exactly.

Once returned to UCL, C1's sloped axial surface was aligned to the rotary table's rotational axis. The ring was measured on the inner and outer diameter surface, with

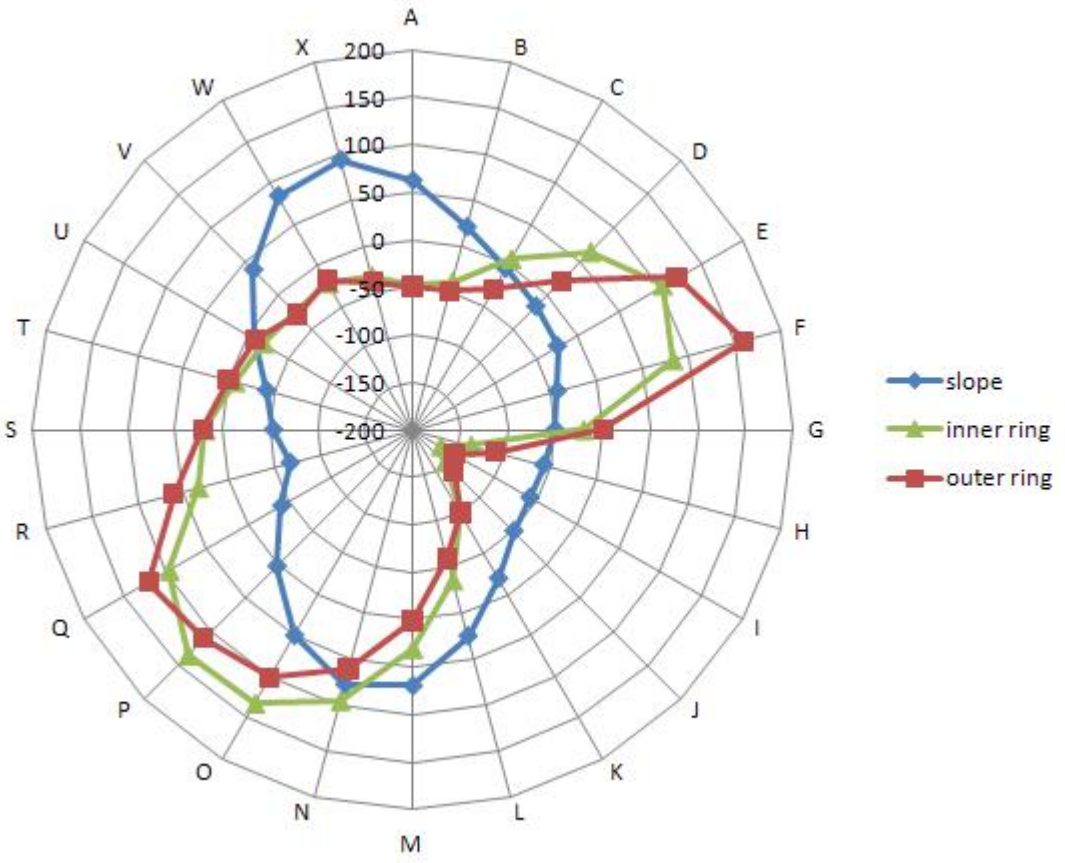

Figure 4.10: C1's relative alignment of the sloped axial surface to the inner and outer dimensions of the ring when the weight is taken by the retaining ring. Units are in μm.

their shape and alignment, with respect to the rotational axis, is shown in figure 4.10. In general the inner and outer diameters followed each other, but they are elongated in a different direction to the sloped surface. This could be changed by rotating the ring with respect to the cell but this risks increasing the height variation in the sloped surface when the cell is suspended by the ring. The ring has a variation from its nominal zero point of $\pm 150\mu$m. This is in more of a kidney bean shape than an oval, making it not ideal for alignment. The cell was checked to see if this was more circular than the mating ring with its shape shown in figure 4.11. The cell has a shape similar to that of a figure of eight, with the outer cell (more useful for alignment than the inner cell due to access issues) much worse than the circularity of the inner cell. The outer cell diameter varied by $\pm 300\mu$m, although part of this variation is from the outer cell having a different central axis to that of the sloped surface.

The alignment of the inserts with respect to the sloped axial surface was also checked, with the results shown in figure 4.12. The inserts are off-centred with respect to the sloped

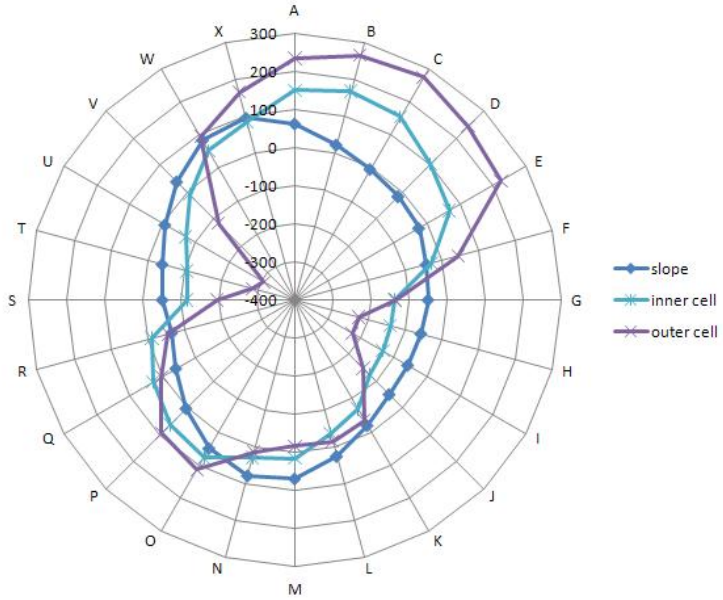

Figure 4.11: C1's relative alignment of the sloped axial surface to the inner and outer cell's diameter. Units are in μm.

surface and are in a trefoil shape. They have a variation of $\pm 150\mu$m. This does not cause any issues, as all the inserts are removalbe untill they are glued into position and so will be re-milled to the correct thickness once the lens has been placed in the cell.

The cell and ring were originally aligned with the weight taken by the cell. Whilst this allows for easy movement and placement of the ring, any wedge in the ring will, once bolted to the barrel, come through and distort the sloped surface. The sloped surface was aligned to the rotational centre of the rotary table and then the ring positioned to reduce the overall saddle shape that was in both the sloped axial surface and the retaining ring. This can be seen in figure 4.13. The difference between the ring and the sloped surface height variation was found as a prediction of what would be seen when the weight was taken by the retaining ring, as shown in figure 4.14. Once the ring and cell had been bolted together the cell was turned upside down and recentred on the sloped surface. This meant that the retaining ring should be sitting flat and all distortions would be going through to the sloped surface, as would occur when the lens-cell is mounted to the barrel. A height variation of 150μm was found, as shown in figure 4.15. The peak and trough that created this height variation occur over half of the sloped surface. Whilst it might be possible to slightly reduce this variation by better centering of the sloped surface, its large value was very worrying as the pads are designed to only compress by 100μm, leaving a possibility that some pads would not touch the lens. To compensate for the variation in the slope

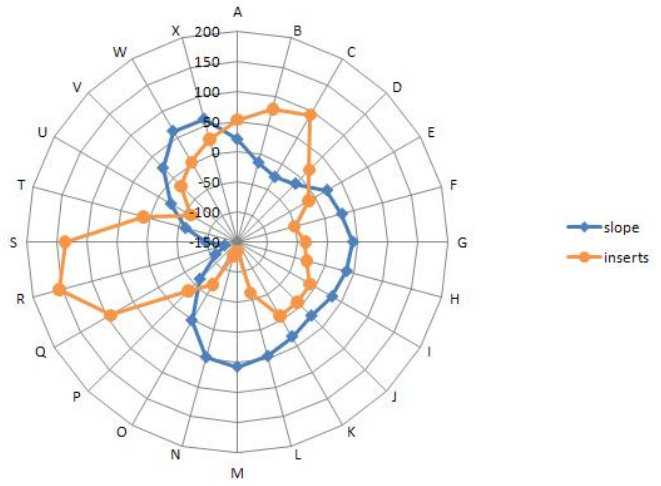

Figure 4.12: C1's relative alignment of the sloped axial surface to the inside face of the inserts. Units are in μm.

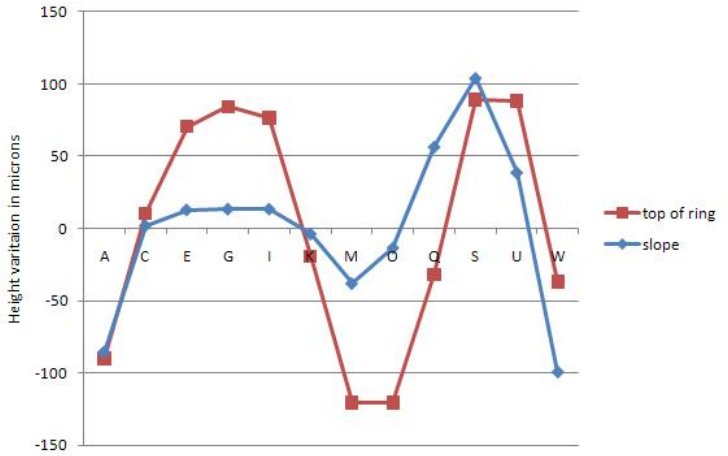

Figure 4.13: C1's height variation of the sloped axial surface and the top of mating ring when C1's weight is being supported by the cell.

surface the thickness of the axial pads covering this area will vary. The thickness will be calculated to provide a flat surface for the lens to sit on. In order to maintain the same compression modulus over all the pads, the area of the axial pads will be increased by the correct ratio in order to keep the same S factor.

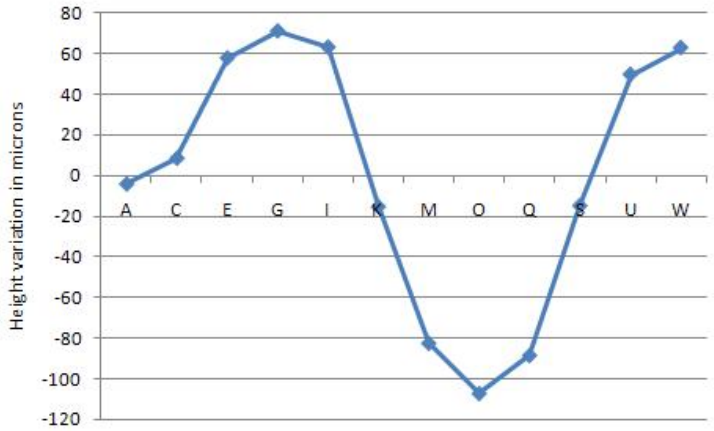

Figure 4.14: The expected height variation of the sloped axial surface when cell 1's weight is being supported by the mating ring. This prediction was generated from the data in figure 4.13.

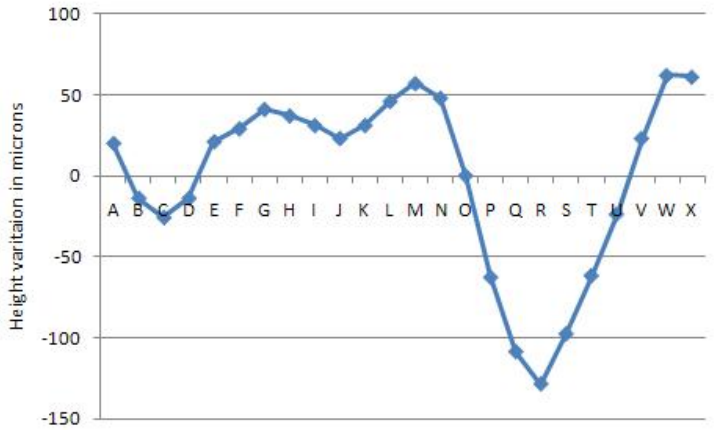

Figure 4.15: The measured height variation of the sloped axial surface when C1's weight is being supported by the mating ring.

4.5.2 C2 Cell Measurement

C2 has twelve very large inserts, unlike the other lenses that have twenty-four smaller inserts. For the other lenses, measurements were taken at the centre of these inserts. However as the inserts are so large on C2 the middle of the flexures was used instead. This allowed 24 points around the cell and mating ring to be measured. The lettering system used normally refers to the inserts, for C2 the flexures were lettered. AL refers to the left flexure over insert A, and AR refers to the right flexure over insert A. Again, these were marked on the cell for consistency.

C2 also has a kidney bean shaped mating ring. This distortion was less pronounced then C1's ring, with a maximum of 80μm and a minimum of -120μm, as shown in figure 4.16. Again, the inner and outer diameters of the ring are in good agreement. The cell, as shown in figure 4.17, has a smaller variation, but is a much more irregular shape. This makes it impossible to find a reasonable centre by run out alone. No data was taken on the positioning of the inserts relative to the sloped surface.

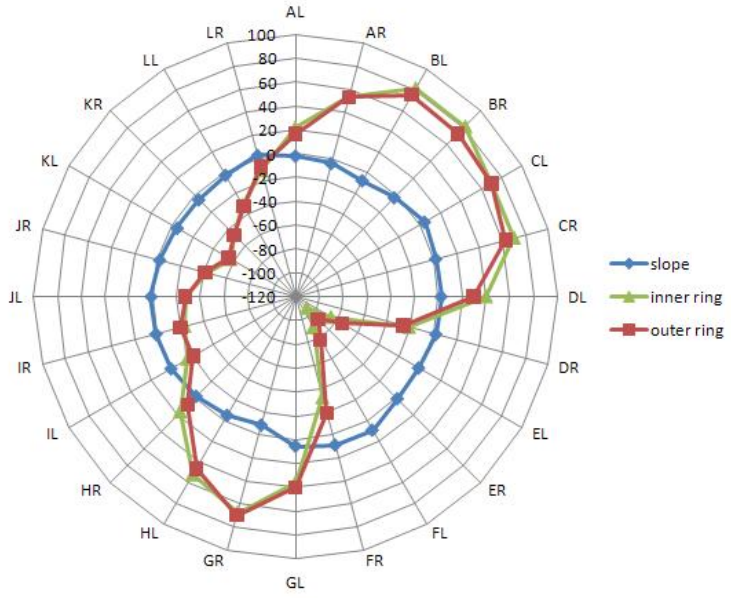

Figure 4.16: C2's relative alignment of the sloped axial surface to both the inner and outer diameter of the retaining ring with respect to the rotational axis. Units are in μm.

The height variation in the sloped surface and the top of the retaining ring, were measured when the weight was being supported by the cell. The variation is shown in figure 4.18, with a small variation in the sloped surface and approximately 80μm variation in the top of ring being found. The expected height variation is a wedge of approximately

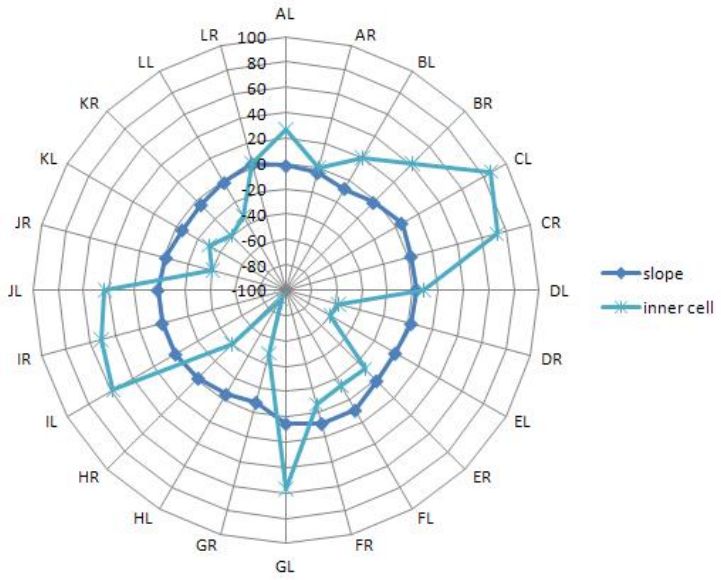

Figure 4.17: The relative alignment of the sloped axial surface to the inner cell's diameter with respect to the rotational axis. Units are in μm.

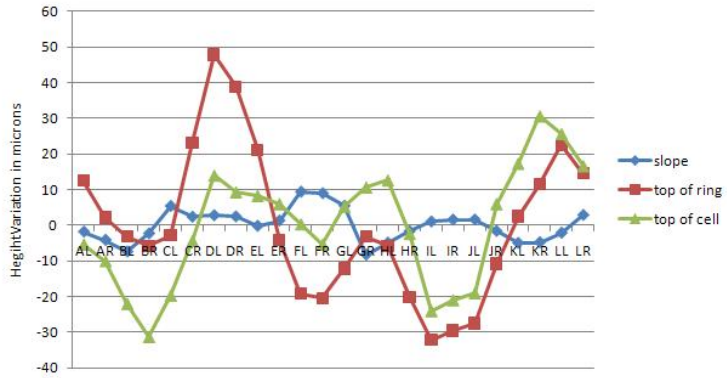

Figure 4.18: The height variation of the sloped axial surface and the top of retaining ring when C2's weight is being supported by the cell.

70μm as shown in the model in figure 4.19. The wedge across the diameter of C2 is 70μm, which should allow the wedge in the lens to be cancelled out. This allows C2's aspheric surface to be positioned perpendicular to the barrel's rotational axis.

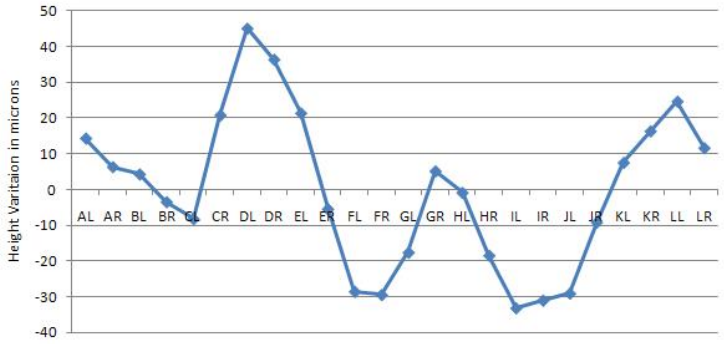

Figure 4.19: The expected height variation of the sloped axial surface when C2's weight is being supported by the mating ring.

4.5.3 C3 Cell Measurements

Due to being mounted onto C2 rather than the barrel, the C3 cell differs from the other cells in that the mating ring and cell were cast as a single piece. This means that it cannot be realigned to the cell to reduce any wedge in the ring or slope, nor to align the rotational centres of the mating ring and axial surface. Two sets of measurements were taken, firstly when the outer ring diameter was aligned and secondly when the sloped surface was aligned. Both times the cell was resting on the mating ring on the rotary table.

C3's ring was initially aligned with respect to the rotational axis of the rotary table. The sloped axial surface was measured at the top and the bottom of the slope to see if there was any wedge or angle in it. As can been seen in figure 4.20 the sloped surface is off-centre relative to the outer ring by approximately 60μm. This is probably caused by the wedge in the ring of about 100μm that is shown in figure 4.21. Figure 4.22 shows the variation in the top and bottom of the sloped surface, with the decentre to the rotational axis clearly visible. However, the top and bottom follow each other closely, giving a flat surface for the lens to sit on.

C3 was then recentered so that the axial sloped surface was aligned with the rotary axis. The outer ring's variation was then remapped as this is the position the cell will be required to be in when attached to C2. Figure 4.23 shows the new shape of the outer ring when the sloped surface is aligned. However, it was found that further machining of this outer diameter was required; this is discussed in chapter 6, section 6.8. Figure 4.24 shows that the cell follows the alignment of the mating ring rather than that of the sloped surface. This means that we are probably compensating for a wedge in the ring by decentring the sloped axial surface. However, figures 4.25 and 4.26 show that there is very little difference between the height variation of the top and bottom slopes and that the overall wedge is reduced to about 40μm, which is well within our error budget of 68μm.

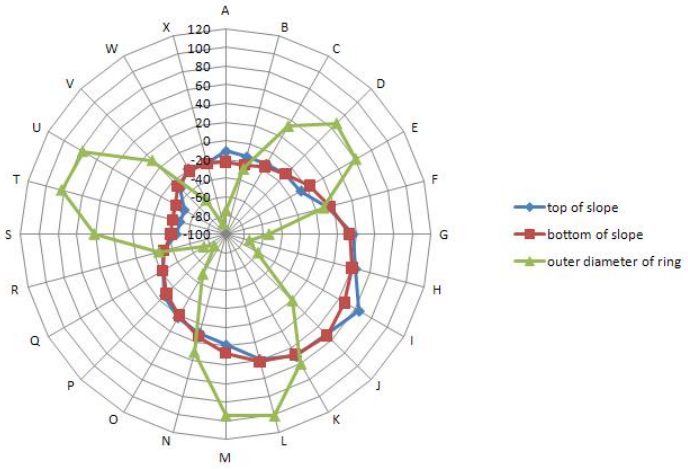

Figure 4.20: C3's ring is aligned to the rotational axis, the sloped axial surface is decentred by approximately 60μm. Units are in μm.

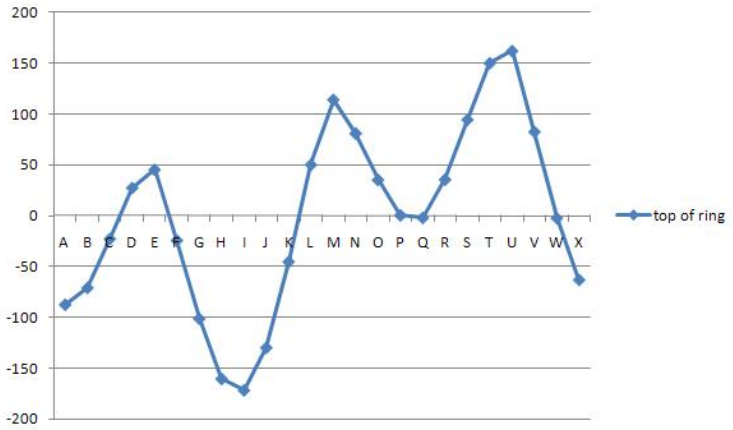

Figure 4.21: Height variation of the top of the C3 ring. The sine wave shows that there is a wedge present in the ring. Units are in μm.

Figure 4.22: Variation in the C3 axial surface at the top near the cell and bottom near the edge of the lip. The decentre of this slope is clearly visible as a sine wave. Units are in μm.

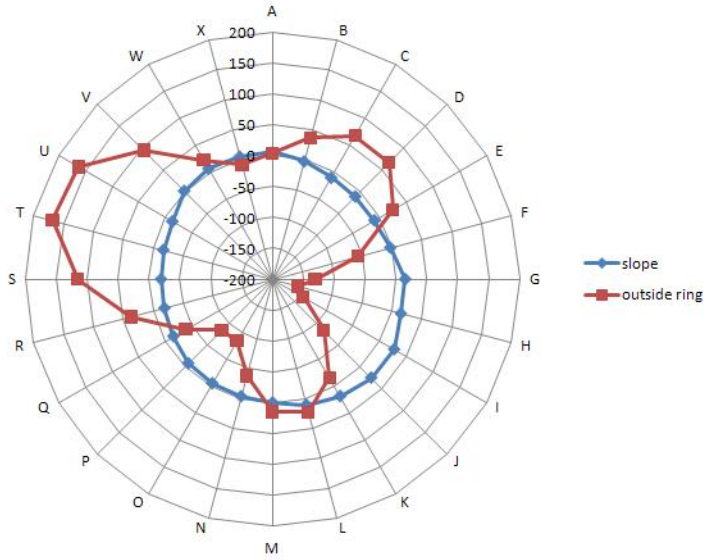

Figure 4.23: Alignment of the C3 sloped axial surface to the outer ring diameter when the sloped surface is aligned to the rotational axis. Units are in μm.

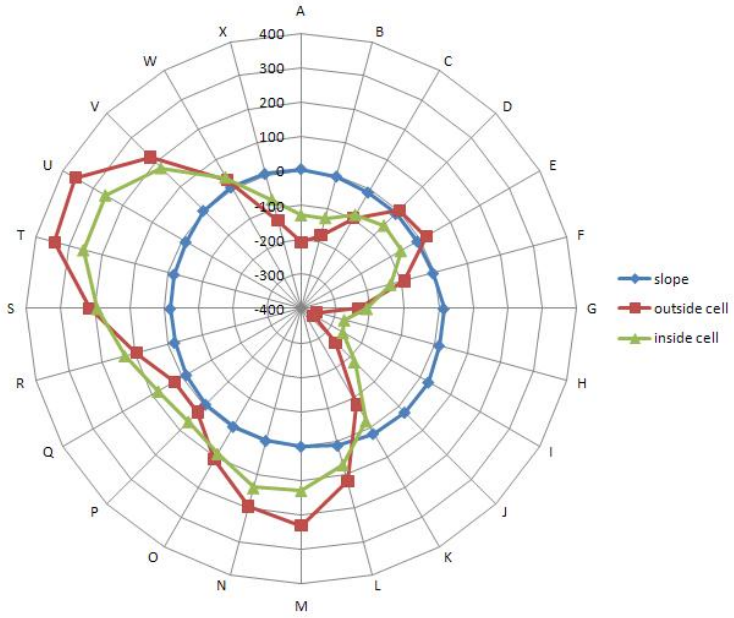

Figure 4.24: Alignment of the sloped axial surface to the cell diameters when the C3 sloped surface is aligned to the rotational axis. Units are in μm.

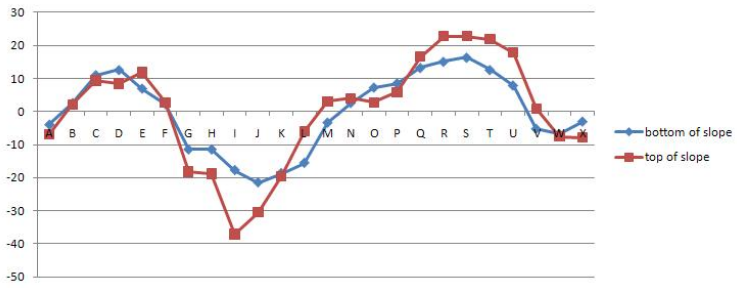

Figure 4.25: Height variation of the top and bottom of the sloped axial surface on the C3 cell. Units are in μm.

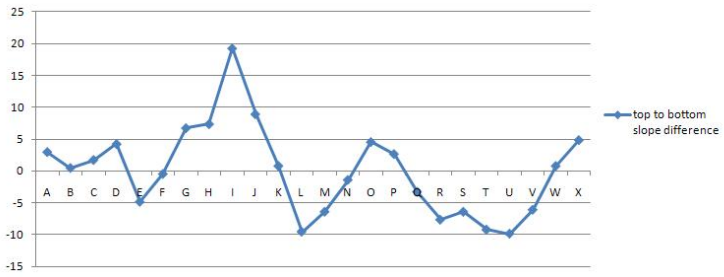

Figure 4.26: Difference between the height variation of the top and bottom of the sloped axial surface on the C3 cell. Units are in μm.

4.5.4 C4 Measurement

Initial alignment of C4's mating ring to the cell was done with the weight being taken by the cell rather than the ring, which will take the weight during operation. As such after the initial alignment the cell was flipped so the wieght was being taken on the ring and re-aligned with the rotational axis. It was found that this caused an unexpectedly large tilt in the sloped surface when the cell was supported by the mating ring, although it did allow for easy alignment of the ring. It is believed that this tilt comes from a tilt in the bottom of the cell so when the sloped surface is aligned with respect to the rotational axis this decentres the cell to compensate for the tilt. To remove this the C4 cell was placed on lab jacks, which were then adjusted to minimise the run-out on the top of the mating ring, the surface that will be attached to the barrel as shown in figure 4.27. Once the top of the mating ring was levelled the ring and slope surface were aligned with respect the rotational axis whilst on the lab jacks. After alignment the cell was removed from the lab jacks and the slope height variation measured with the mating ring supporting the weight on the rotary table.

Using this set-up the ring was aligned to the sloped surface giving the alignment shown in figure 4.28 and the corresponding graph for the cell is in figure 4.29. An estimate of the expected variation in the height of the sloped surface was then generated as shown in figure 4.30.

The cell was then inverted and the weight of the cell was placed on the mating ring and once again aligned to the table's rotational axis. The mating ring was clamped into position in order to measure the variation in the sloped surface that would be seen when the cell is attached to the barrel. This clamping meant that only the inner diameter of the mating ring was measured against the sloped surface, as shown in figure 4.31, with the slope variation found to be 50μm as seen in figure 4.32.

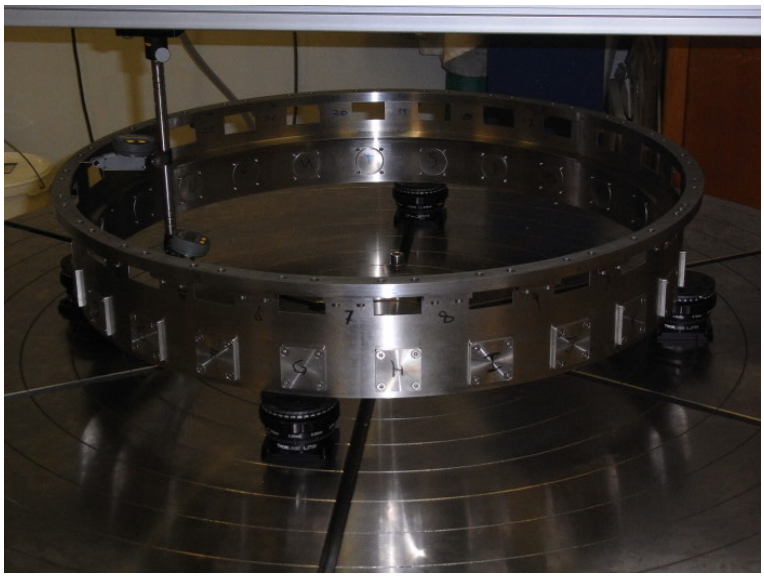

Figure 4.27: C4 cell raised on lab jacks to remove the uneven cell surface for alignment of the ring to sloped surface.

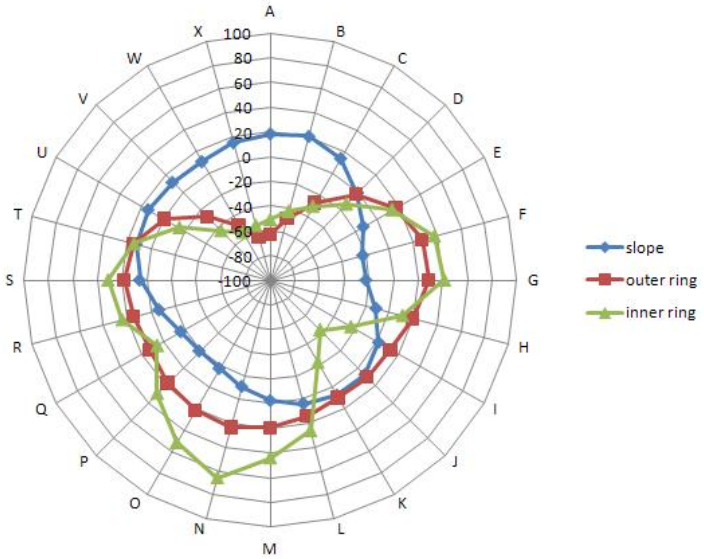

Figure 4.28: Alignment of the inner and outer diameter of the mating ring to the sloped axial surface when the C4 cell is placed on lab jacks. Units are in μm.

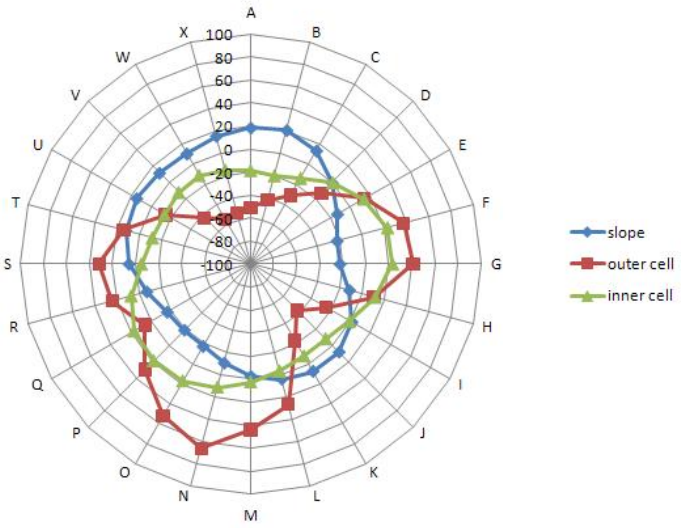

Figure 4.29: Alignment of the inner and outer diameter of the cell to the sloped axial surface when the C4 cell is placed on lab jacks. Units are in μm.

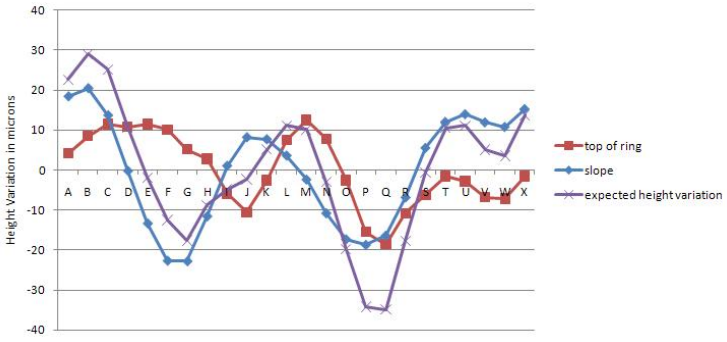

Figure 4.30: Height variation in the ring and the sloped axial surface on C4. This has been used to estimate the height variation that will be seen in the sloped surface when the cell is attached to the barrel.

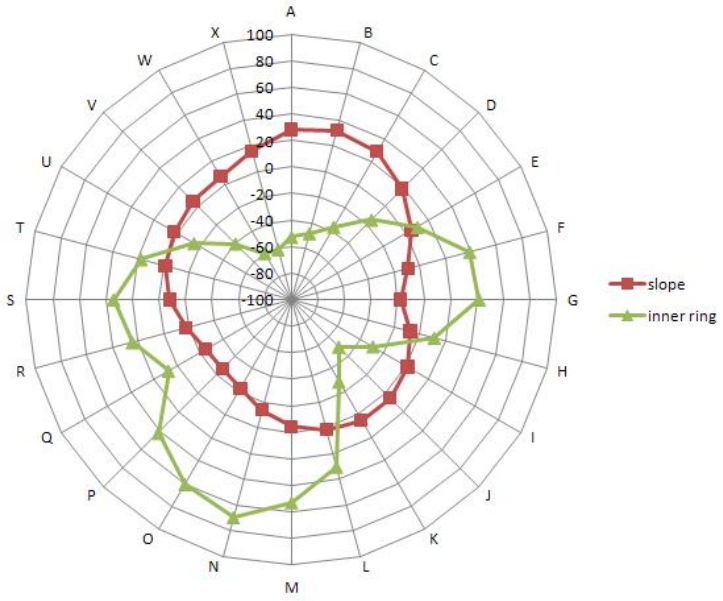

Figure 4.31: Alignment of the C4 sloped surface to the mating ring when the ring is clamped and aligned to the rotary table. Units are in μm.

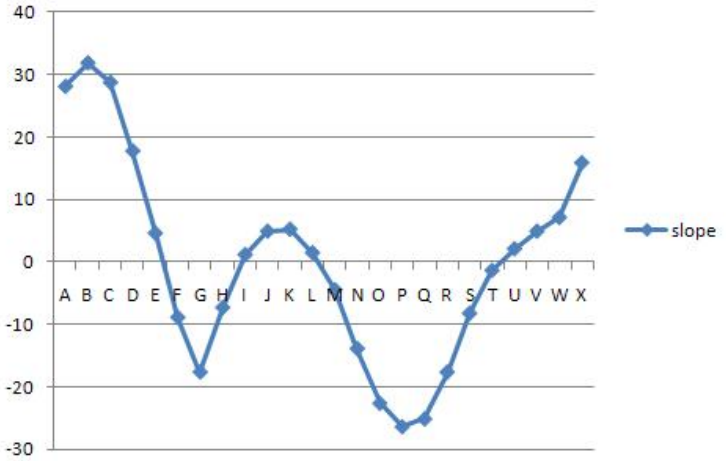

Figure 4.32: Height variation of the C4's sloped axial surface when the ring is clamped and centred. Units are in μm.

4.6 Cell to Barrel Alignment Measurements

Once the mating rings had been attached, the cells C1, C2 and C4 were shipped to Dr Gutierrez at the Fermi National Accelerator Laboratory, henceforth referred to as Fermilab, for alignment with the barrel. The inner diameters of the rings were centred on the barrel's Z axis. The barrel coordinate system is shown in figure 4.33, which relates to the graphs generated at Fermilab by south being in the positive Y direction and east in the positive X direction, as in figure 4.34. Once centred the cells were pinned into position using fiducial dowels. These dowels will allow the cells to be returned to the aligned position once the lenses have been glued within. The C3 cell was not sent to Fermilab due to it being mounted as an air-spaced doublet on the C2 cell.

Fermilab used a Coordinate Measuring Machine (CMM) to determine the centres of the cells and their alignment to the barrel. Due to their equipment they were only able to reach the inner diameter of the mating ring. Measurements were originally taken when the cell was not attached to the barrel, shown as filled dots on figures 4.35 to 4.40. Once the barrel was pinned into position open circles were then used. The barrel was rotated and the measurements repeated, with each measurement then plotted in a different colour. The measurements of the position of the inner diameter had an nominal value of 500 added to them to allow clear plotting. The sloped surfaces had a variable nominal value added, which is the radius at which the reading was taken. This allowed three readings on the sloped surface to be taken at different radii (a small, medium and large circle). This allowed variations in the cone angle of the sloped surface to be detected.

In general the results taken at Fermilab had good agreement with those taken at UCL. As the measurements at Fermilab were taken when the cell was attached to the barrel, these were taken as the definite results and were used for the alignment of the lenses within the cells. To accommodate this the plotting of the cell alignment in chapter 6 is changed to match the style used at Fermilab and allow a direct comparison between measurements taken at Fermilab and UCL.

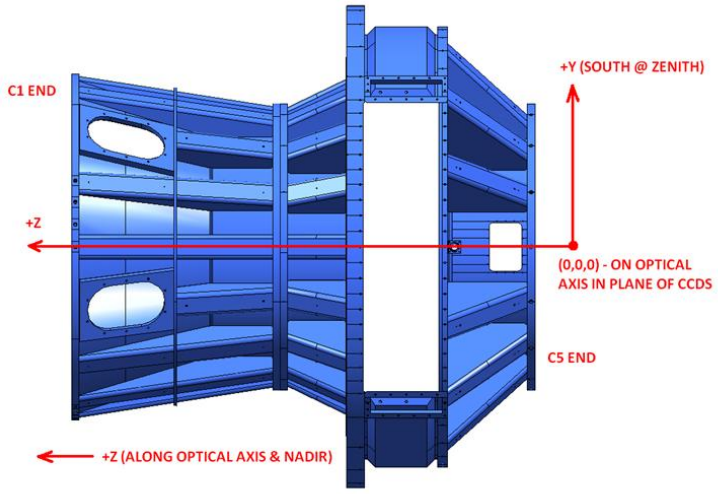

Figure 4.33: Coordinate system used to define the directions of objects attached to the barrel. The cross-section has the primary mirror to the far left[53].

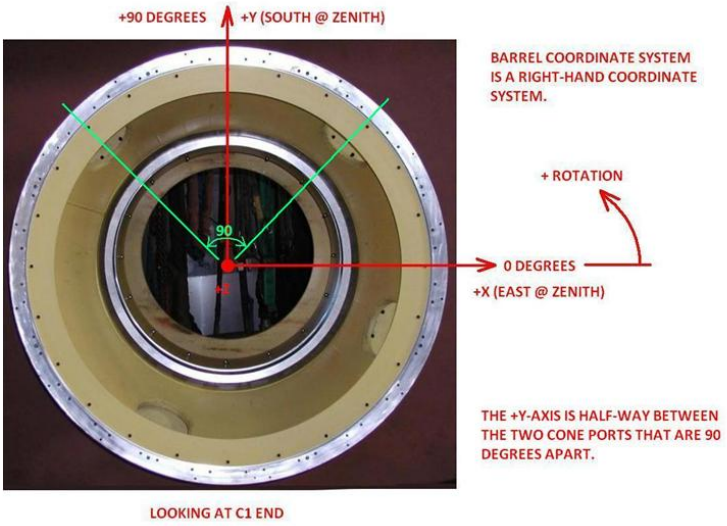

Figure 4.34: Coordinate system as looking into the optical corrector from the C1 end down. South and North are defined as the +Y and +X direction respectively[53] and a right-handed coordinate system is used.

4.6.1 Cell centring and axial flatness

Maps of the measurements taken at Fermilab are shown below. Figure 4.35 shows the shape of the inner diameter of the C1 mating ring when it is aligned to the central axis of the barrel with figure 4.36 showing the height variation in the C1 sloped axial surface. Similar maps were produced for C2 where figure 4.37 shows the inner diameter of the C2 mating ring and figure 4.38 gives the height variation of the sloped surface at this position. The C4 mating ring was realigned at Fermilab to reduce the tilt on the sloped surface. The final tilt on the sloped surface is shown in figure 4.40, with the mating ring aligned as in figure 4.39.

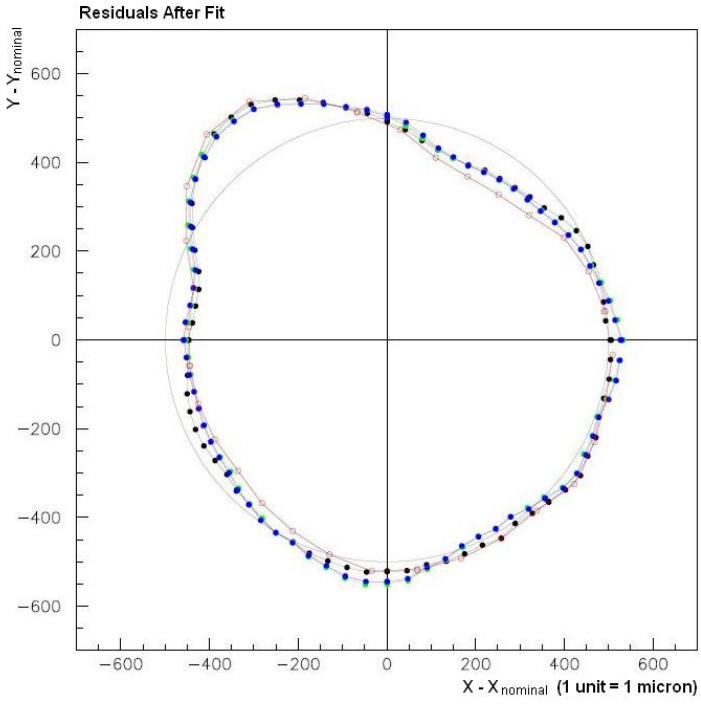

Figure 4.35: Measurements of the inner diameter of the mating ring on C1, taken at Fermilab. The filled dots are when the cell was attached to the barrel and the open dots are when the cell was unconstrained.

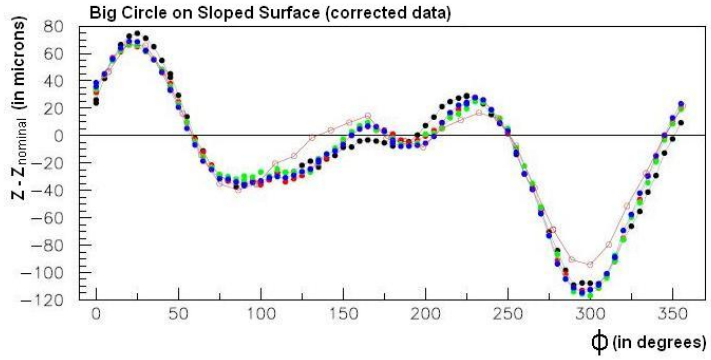

Figure 4.36: Measurements of the sloped surface on the cell C1, taken at Fermilab. The filled dots are when the cell was attached to the barrel and the open dots are when the cell was unconstrained.

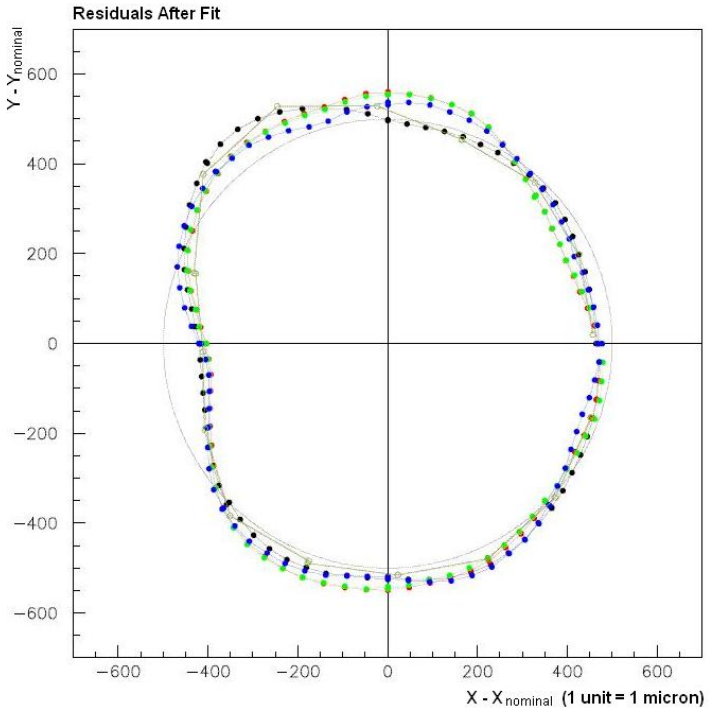

Figure 4.37: Measurements of the inner diameter of the mating ring on C2, taken at Fermilab. The filled dots are when the cell was attached to the barrel and the open dots are when the cell was unconstrained.

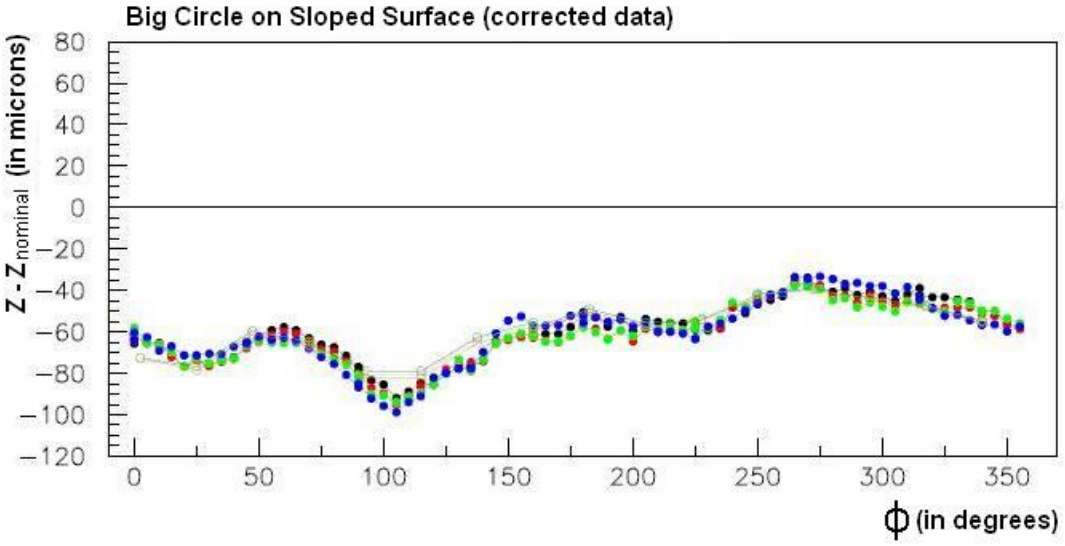

Figure 4.38: Measurements of the sloped surface on the cell C2, taken at Fermilab. The filled dots are when the cell was attached to the barrel and the open dots are when the cell was unconstrained.

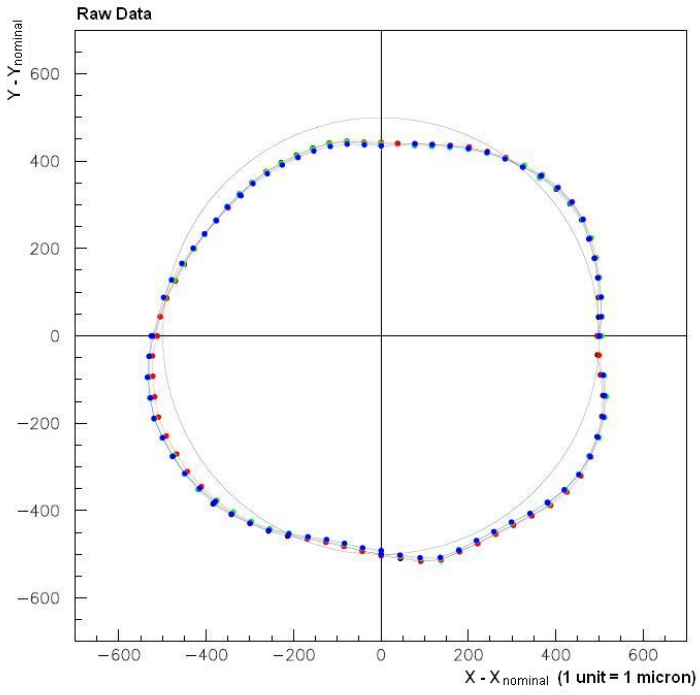

Figure 4.39: Measurements of the inner diameter of the mating ring on C4, taken at Fermilab. The filled dots are when the cell was attached to the barrel and the open dots are when the cell was unconstrained.

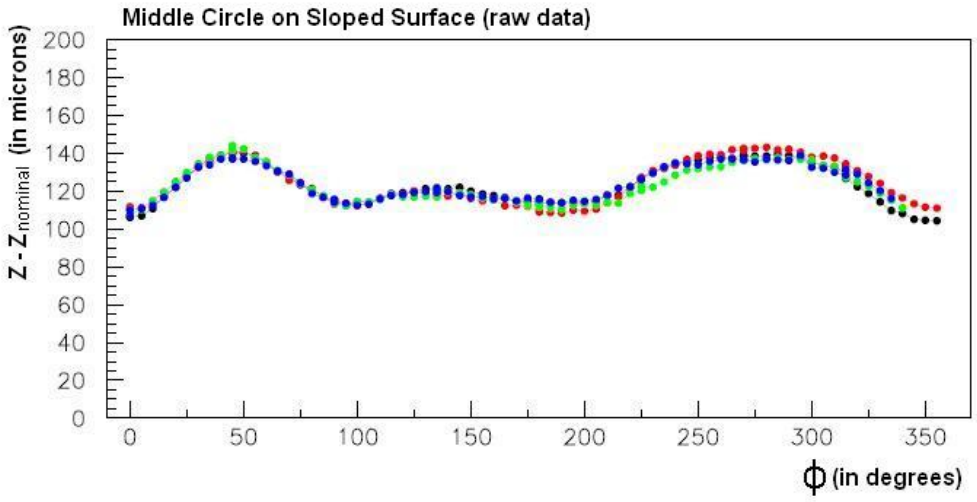

Figure 4.40: Measurements of the sloped surface on the cell C4, taken at Fermilab. The filled dots are when the cell was attached to the barrel and the open dots are when the cell was unconstrained.

4.6.2 On barrel centring

From each set of measurements the centre of the cell was calculated. This was then plotted against the centre of the barrel itself as shown in figure 4.41. It can be seen that all the cells are slightly off centre towards the -Y direction. The hexapod will be able to hold the barrel slightly to the +Y direction to help correct for this.

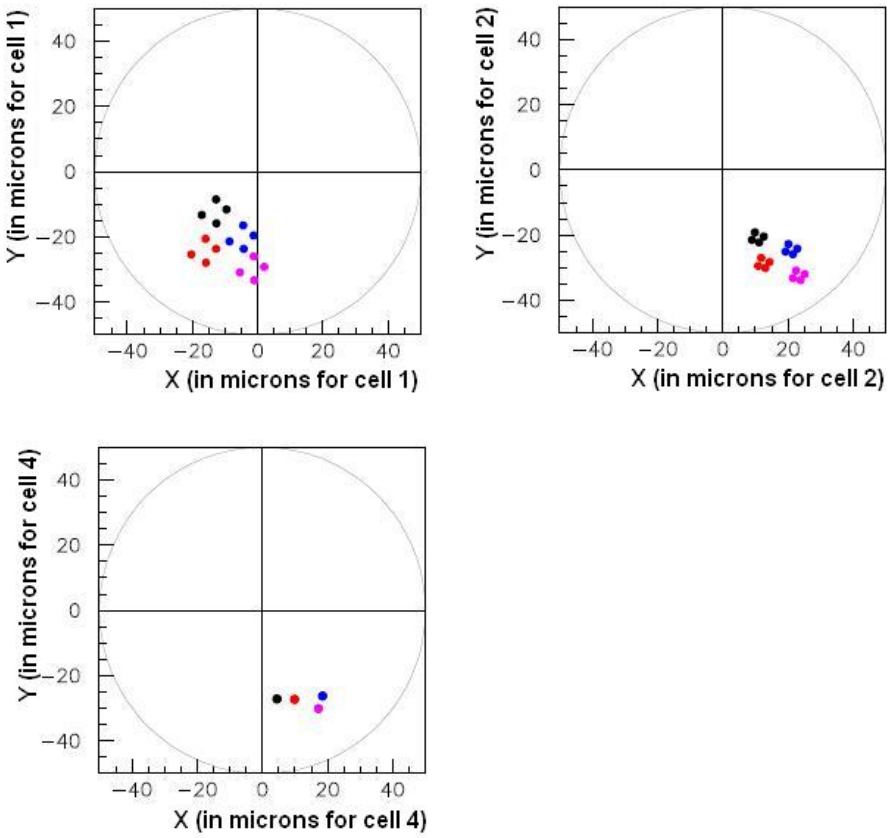

Figure 4.41: Calculated positions of the cell centres when attached to the barrel.

4.7 Summary

The original alignment plan was to centre the lenses by a pure clocking method, with the minimum run-out giving the centre of the cell. However, the non-circular shape of the cell caused this plan to be modified to one of mapping the cell's distortions. The cell was aligned so the sloped surface had a minimum run-out around the rotational axis. The shape of the outer diameter of the retaining ring was then mapped. When aligning the cells to the lenses the position of the outer diameter of the ring was matched to the previous position. This made the cell alignment process more complicated and time consuming then it was originally hoped to be.

Chapter 5

Production of the Lenses

Anything that can go wrong, will go wrong

Murphy's Law

This chapter briefly discusses the production of the lenses and the issues that arose during the polishing and grinding. The lens blanks were produced by Corning Incorporated in the United States and sent to SESO in France for grinding, polishing and coating. During the production of the lenses, several issues arose that required changes to the specifications of the lenses. Before these were approved the optical designs were re-optimised using the proposed changes with the option of using spacing between the lenses to compensate for changes in the lens' thickness. This was done to ensure that the changes did not affect the final image quality of DECam.

The lens blanks were produced by a flame hydrolysis process[38] and made 2mm oversized to allow for the material that is removed by the grinding and polishing processes. The final C2 blank is shown in figure 5.1(a) and the C1 slumped blank in figure 5.1(b). Slumping is where the fused silica is heated until it is malleable at which point it can be moulded to the correct radius for the lens. This process was required due to the small radius of curvature of the lens, although it carries the risk of increasing inhomogeneities within the glass. After leaving Corning, the lenses were sent to SESO for grinding and polishing. Figure 5.2 shows one of the lenses undergoing the grinding process with figure 5.3 showing the C1 lens during the acceptance testing.

Figure 5.1: The C2 lens blank, left, with Brenna Flaugher, and the slumped C1 lens blank, right, as delivered by Corning for grinding and polishing by SESO.

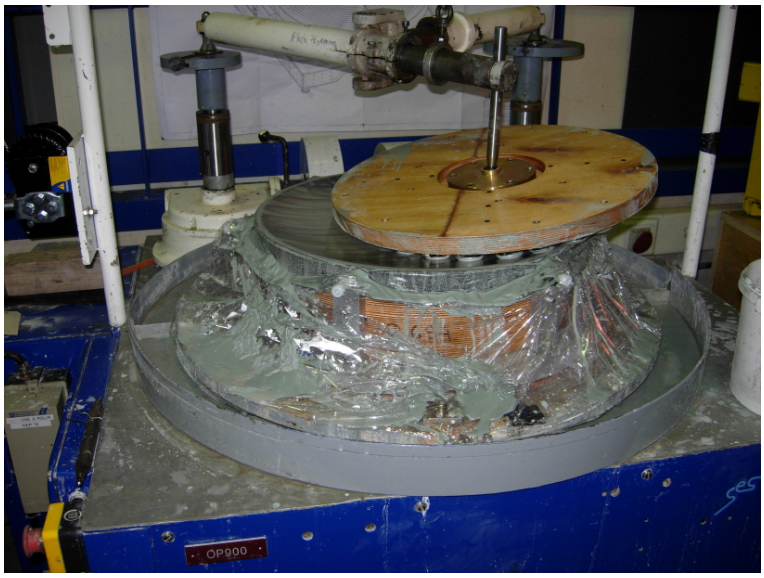

Figure 5.2: One of the lenses being ground at SESO.

5.1 Changes Made to the Lenses

All the lenses had been made with a greater thickness than SESO wished to remove, due to time constraints and handling risks. As such it was agreed that the thickness specifications on all the lenses would be increased. During the grinding, polishing and coating process several errors were made that caused damage to the lenses. No permanent damage was done to the clear aperture of the lenses, allowing all of them to past acceptance testing.

5.1.1 Lens 1

During the grinding process the glue failed on one of the ceramic tiles on the grinding tool. This caused it to fall onto the lens, causing minor surface damage inside the clear

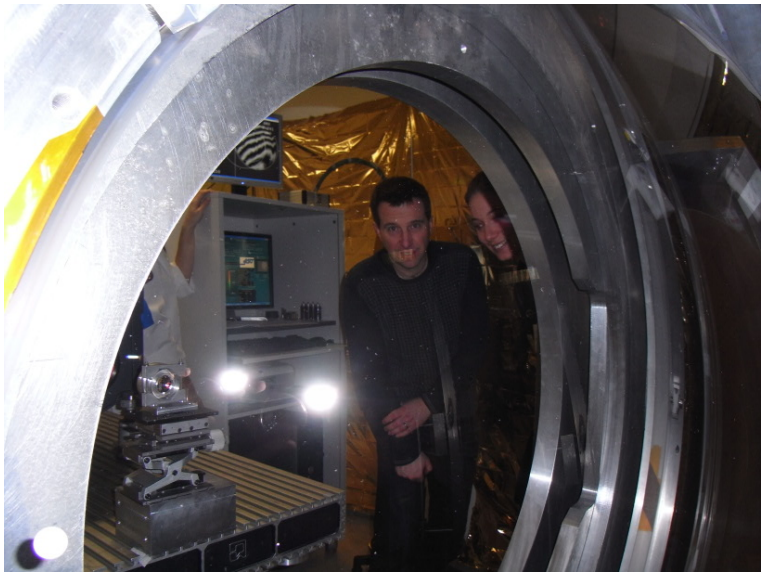

Figure 5.3: The C1 lens undergoing acceptance testing after it has been fine ground and polished.

aperture. This required C1 to be reground and due to this the thickness was reduced to slightly below the specifications. However, this brought it closer to the original, optimal design and there was no degradation in the image quality due to this damage.

5.1.2 Lens 2

Lens 2 is the most badly damaged of all the lenses. A grinding tool slipped off the side of the lens damaging the edge of the convex surface. Approximately thirty degrees of the edge has chips along it, the largest of which stops just outside of the clear aperture. Additionally the outer diameter of this lens was damaged by a fault in the restraining fixture. The screw adjustment system used by SESO to position the lens in X and Y broke through its protection layer marking the outer diameter with 1mm deep pits, 5-6mm in diameter. The spacing of these dents means that it is not possible to evenly space the radial pads without overlapping with some damage.

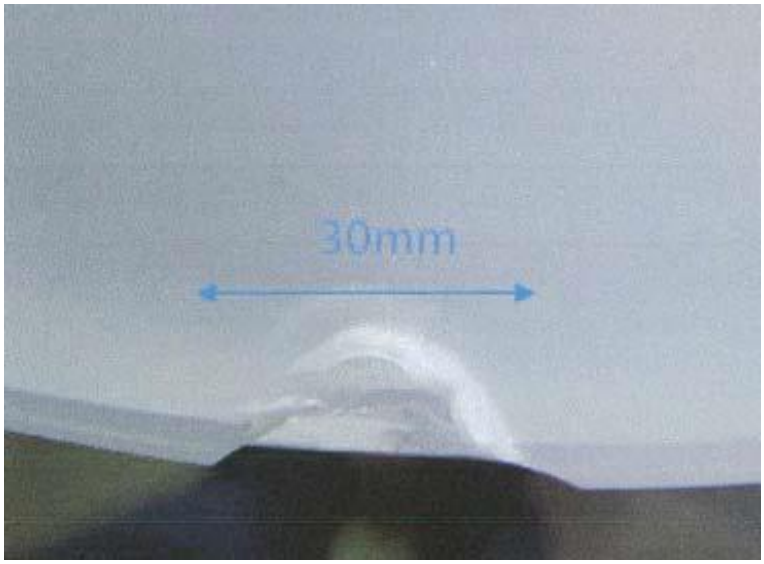

Figure 5.4: C2 at SESO with the damage done to the lens.

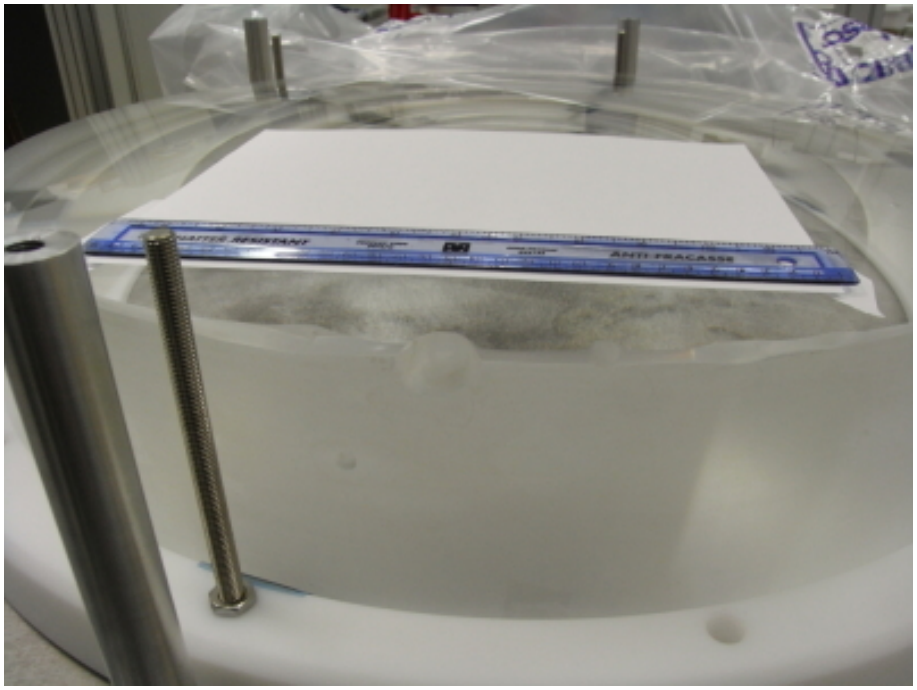

Figure 5.5: C2 with the damage to the convex side of the lens after polishing.

5.1.3 Lens 4

Originally assurances had been given that the asphere on the convex surface of this lens would not cause difficulties in manufacturing. Unfortunately there were problems meeting the slope error specifications at the steep edges of the lens. A further issue arose with the calibration alignment of the wavefront sensor data. This caused a polishing run do be done at the wrong orientation putting in depressions around the edge of the lens which then had to be removed. Combined, these errors caused the production of C4 to be delayed. By the time the lens was ready for coating, SESO's coating plant was just taken out of commission due to an upgrade and so another vendor, Reynard Corporation in the United States, was sourced. Unfortunately during coating outgassing between the tape used to protect the lens caused surface damage to the lens just outside the clear aperture. Figure 5.6 shows the lens during acceptance testing; once the lens was removed from the holding plastic the damage to the lens was obvious. This is shown in figure 5.7 where the regular white markings are surface damage to the lens.

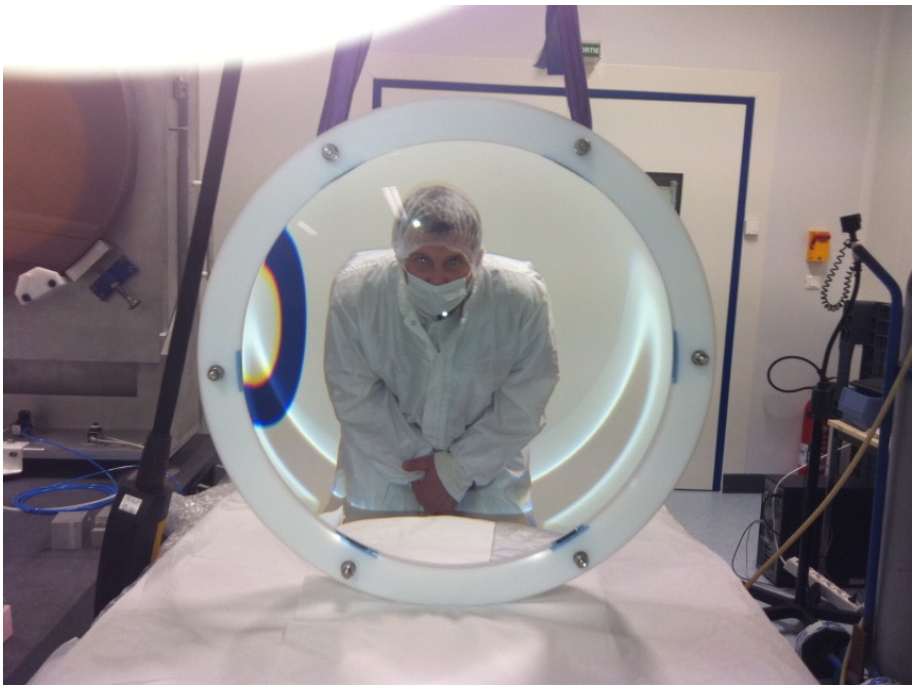

Figure 5.6: Peter Doel with the C4 lens during the acceptance inspection at SESO.

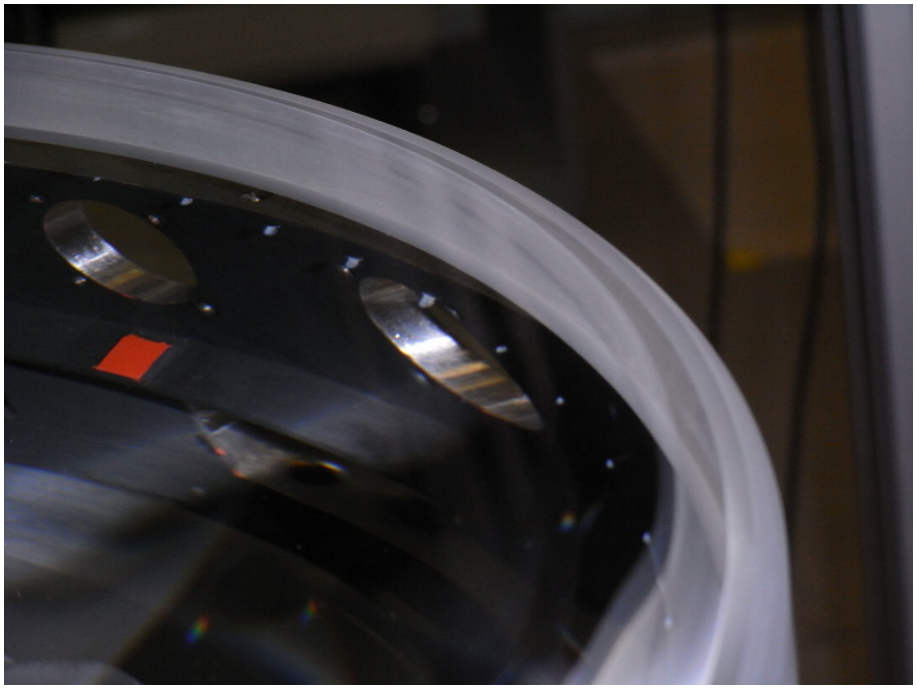

Figure 5.7: The damage to the C4 lens. It is being held lowered into its cell, where the red is one of the axial pads and the white markings at regular intervals around the edge of the lens is the damage.

5.1.4 Lens 5

A failure in a holding support resulted in a grinding tool coming into contact with the edge of the C5 lens for some time, causing damage which is shown in figure 5.8. The ring that was ground into the lens was approximately 2.7mm deep and extended 6mm into the clear aperture.

FEA models were run to determine the effect of this damage and the effect of thinning the lens on the stress and distortion it will undergo when a vacuum is placed on it. To remove the damage, the annular ring was thinned by 3mm and the concave surface had 1.5mm milled off. This allowed the full clear aperture to be restored with minimal effect on the optical performance[54].

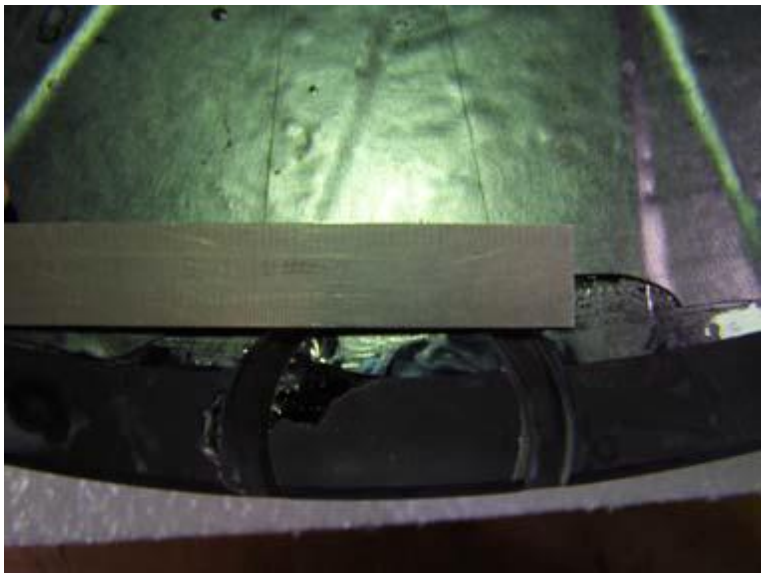

Figure 5.8: Lens 5 at SESO with the damage to the side of the lens.

A scour mark was placed on the side of this lens in order to indicate the wedge. As this lens forms the cryostat window there was concern that a sharp mark on the lens could cause an area of high stress when under vacuum, weakening the lens. The lens was returned for further polishing for this mark to be removed by flattening the side of the lens.

During the initial inspection of the lens in February 2010 small pits, less than 5μm big, were found on the lens. They were not expected to have an effect on the performance of the lens but were removed as a precaution[55].

5.2 Specifications and Actual Lens Dimensions

In table 5.1 the final, measured radius, central thickness and wedge of each of the lenses is compared to the specifications[56]. As the polishing process progressed some of these specifications were changed, those presented here are the modified specifications as agreed between SESO and UCL. Tables 5.2 and 5.3 show the errors on the lenses' slope and form compared to the specifications. Here the difficultly on meeting the requirements at the edge of C4 can be seen.

Lens	Surface 1 Radius (mm)	Surface 2 Radius (mm)	Central Thickness (mm)	Wedge
L1	685.821 ± 0.4	711.827 ± 0.4	112.1(+0.3,-1.9)	< 0.1
	685.98 ± 0.02	711.87 ± 0.02	110.54	0.050
L2	3387.35 ± 2	507.05 ± 0.3	51.0 ± 0.3	< 0.1
	3385.6 ± 0.05	506.944 ± 0.02	51.136 ± 0.01	0.027
L3	944.00 ± 1.5	2417.0 ± 2	75.7 ± 0.2	< 0.1
	943.6 ± 0.05	2416.85 ± 0.2	75.49 ± 0.01	0.043
L4	662.779 ± 0.4	1798.2 ± 0.8	101.661 ± 0.4	< 0.1
	662.43	1798.28	101.461	0.039
L5	900.00 ± 0.6	685.127 ± 0.3	53.0 ± 0.1	< 0.1
	899.815 ± 0.02	685.01 ± 0.03	53.105	0.071

Table 5.1: The lens specifications and the sizes of the lenses as made. The top line gives the specification and bottom line is the as measured values by SESO[56].

Lens	Convex Surface Form	Concave Surface Form	Convex Slope Error	Concave Slope Error
C1	<60nm RMS over 600mm sub-pupil	<60nm RMS over 600mm sub-pupil	<1 μrad RMS	<1 μrad RMS
	122nm RMS on CA (109nm RMS with Astig removed)	129nm RMS on CA (75nm RMS with Astig removed)	<1.25 μrad RMS over 80% <3.5 μrad RMS over 100%	<1.26 μrad RMS over 80% <2 μrad RMS over 100%
C2	Av PTV 0.3λ per 300mm sub-pupil Max PTV per 300mm 0.45λ	<300nm RMS over CA	<1 μrad RMS	<5μrad RMS
	Av PTV 0.3λ per 300mm sub-pupil Max PTV per 300mm 0.5λ	120nm RMS (asphere)	Not measurable	7 μrad RMS over 80% of CA 14 μrad RMS over 100% of CA
C3	<60nm RMS over CA	<60nm RMS over CA	<1 μrad RMS	<1 μrad RMS
	42nm RMS (Av at 0° and 90°)	52nm RMS	<1 μrad RMS over 94% of CA	<1.2 μrad RMS over 80% of CA

Table 5.2: The lens specifications for lenses C1, C2 and C3, with the errors on the surface form, the slope error and the accuracy achieved. The top line gives the specification and bottom line is the as measured values by SESO[56]. CA denotes the clear aperture, Astig is astigmatism, and Av stands for averaged values.

Lens	Convex Surface Form	Concave Surface Form	Convex Slope Error	Concave Slope Error
C4	<500nm RMS over CA	<60nm RMS over CA	<8μrad RMS	<1 μrad RMS
	211nm over CA (asphere)	13nm RMS	<15.15 μrad for 97% <7.74 μrad for 88% <5.63 μrad for 80%	<0.67 μrad for 97%
C5	<60nm RMS over CA	<60nm RMS over CA	<1 μrad RMS	<1 μrad RMS
	22.5nm RMS (Av at 0° and 90°)	14 nm RMS (Av at 0° and 90°)	<0.8 μrad RMS over 100%	<0.74 μrad RMS over 100%

Table 5.3: The lens specifications for the lenses C4 and C5 with the errors on the surface form, the slope error and the accuracy achieved. The top line gives the specification and bottom line is the as measured values by SESO[56]. CA denotes the the clear aperture, Astig is astigmatism, and Av stands for averaged values.

Chapter 6

Alignment of the Lenses Within Their Cells

There are lies, damned lies and statistics.

Mark Twain

This chapter details the procedure used to align the lenses to their holding cells. Initially the alignment of the prototype is discussed and the changes made to the alignment process from the lessons learnt during the prototype alignment. The alignment of each of the DECam lenses is then discussed individually.

6.1 Prototype Alignment

The alignment procedure used on the prototype was based on the methods proposed by Dr Brooks for the DECam lenses[57][58]. Firstly we describe the equipment used and then the placement of the axial pads on the cell as the pads are used to support the lenses. Then the process of bringing the lens into contact with the cell is described. Finally the gluing of the lens into position with the radial pads is discussed. During the prototype's alignment this procedure was refined and adjustments made for the final method used on the DECam lenses. An extra cell manufactured for this testing process was made to the

same design as those from DECam. With an inner diameter of 540mm, it was smaller than the DECam cells but fits a pre-existing lens at UCL.

6.1.1 Prototype alignment structure

As all the alignment is to be done by clocking, the base of the system is a mechanical bearing rotary table. On this table two separate support structures were then placed, one for the cell and one for the lens. Each system requires fine adjustment in the X and Y directions for centring the cell or lens and large movement in the Z direction to allow the lens and cell to be brought into contact. Figure 6.1 shows the alignment set-up used for the prototype with the cell just below the lens. DDGIs are supported from the optical bench for clocking of the lens.

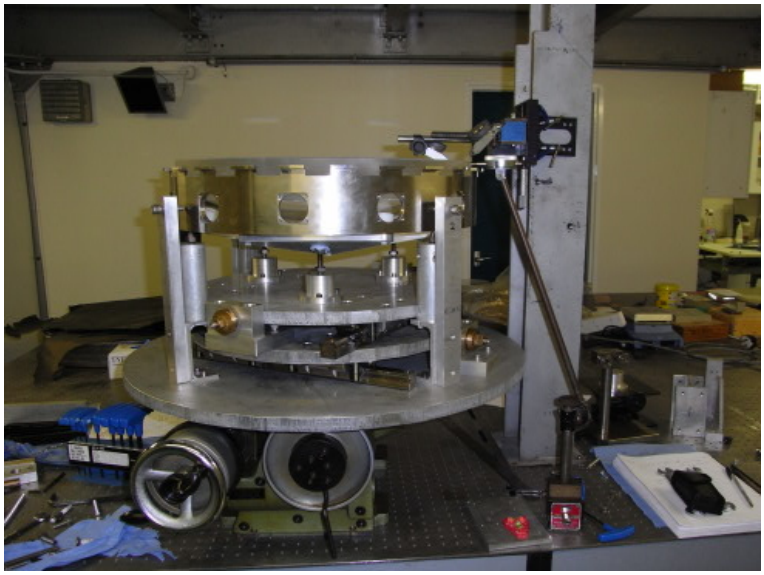

Figure 6.1: Photograph of the alignment of the prototype lens.

For the alignment of the lens two translation plates were placed on top of the rotary table with their runners at 90° with respect to each other. This allows movement in the X and Y directions. Screw adjustments at the end of the runners pushed the translation plates. On the top translation plate three bottle jacks supported the whiffletree structure onto which the lens was placed. Each whiffle plate had three pads on it; one near the centre and two at the edge. The placement of these pads was designed to have each pad taking one ninth of the total weight of the lens.

The cell's alignment structure was much simpler, consisting of four struts placed underneath at 90° intervals. These consisted of a sturdy support with a screw at the top and

bottle jacks attached at the side. The cell rested on the points of the bottle jacks allowing free movement when a sideways force was applied and a large range of movement in Z. Screws above the bottle jacks allowed movement in X and Y for alignment.

6.1.2 Axial pad height of the prototype

The axial pads must be glued to the cell before the alignment can take place. For the prototype, axial pads of the same size as those to be used for C1, 10mm by 10mm with a depth of 0.9mm, were used. These were glued to the prototype cell using a tool to ensure an accurate glue layer of 0.1mm giving a total thickness of 1mm. The heights of the pads were measured using an DDGI which presented several problems. Firstly, using a contact method the probe would give variable readings on non-continuous surfaces as the discontinuities will knock the probe head, changing the zero point on the DDGI. Secondly, the axial surface is sloped, meaning that the reading must be taken at exactly the same radius each time to account for this height variation. In order to attempt to overcome these difficulties a rig was set up on a optical flat that gave a nominal zero position at a set distance from the outside of the cell. However this rig produced very noisy results with a large variability between repeated readings of up to 300μm; swamping the actual height variation between the pads. It was decided that a non-contact method was required to measure the height of the axial pads. As such, no better results for the height of the axial pads was found for the prototype, but equipment was sourced for the DES lenses to prevent this problem reoccurring.

6.1.3 Prototype lens and cell alignment

Once all the axial pads had been glued into position and the alignment rig was assembled; the cell was placed onto the rotary table and the lens placed on its whiffletree. They were then individually aligned to the rotational axis of the rotary table and this common datum allowed then to have a relative alignment.

By clocking only one of the optical surfaces on the lens it is not possible to distinguish between tilt and decentre, making it essential to use either the outer diameter or the lens flat. For this reason micrometer gauges were placed at all three of these positions. Firstly bottle jacks were used to level the lens, secondly the lens was then centred using the translation plates. Once the worst of the misalignment was removed it was necessary to align by increments, as changes intended to correct the tilt tended to create a decentre.

Misalignments were measured using the mechanical method of clocking. By rotating the lens, variations in the tilt and decentre were seen as changes away from the nominal zero point.

No mating ring had been manufactured for the prototype cell, making its alignment more difficult as it is the mating ring that contains the alignment surfaces. These surfaces have tighter tolerances on the flatness and circularity. The top of the flexures were used to determine the tilt on the cell and the outer diameter of the cell was assumed to have the same centre as the sloped surface. This allowed it to be used to determine the decentre. Once again the problem of using a contact probe on a discontinuous surface arose. This could be greatly reduced by setting the DDGI so the tip of the probe just brushes the top of the flexure as it passes under but this vastly reduces the measurement range to tens of microns, requiring the cell to already be in good alignment. Unfortunately the bottle jacks provided a poor support system for the cell and it would easily rock making accurate clocking impossible due to the lack of stability. As such the prototype cell could only be aligned to approximately 400μm at which point it was decided to test the gluing procedure.

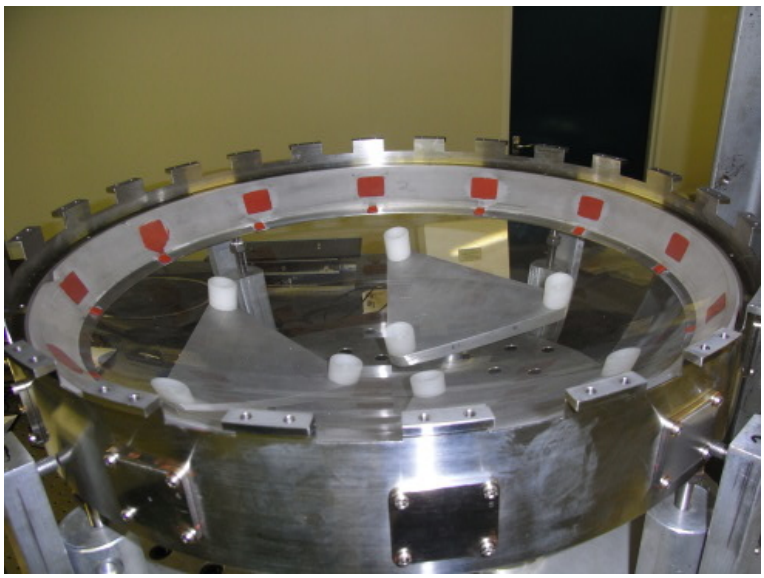

Figure 6.2: Photograph of the completed prototype. The red squares are the RTV glued to the lens. The even colour of the pads shows that there are no air bubbles in the glue layer.

6.1.4 Radial pads of the prototype

As the thermal expansion of the RTV was not going to be tested with the prototype cell, the thickness of the radial pads was set by the gap between the insert and the glass to remove extra milling of the inserts. The glue used for this process was RTV560 itself. The addition of primers to the metal and glass allows RTV to cure to these materials and creates a strong bond. To glue RTV560 to RTV560 a primer layer is not necessary.

A sheet of RTV was cast of the correct thickness, from which square pads were cut. A thin layer of uncured RTV560 was placed on the pad using a syringe and moulded onto the insert by hand to give an even glue layer, with the pad following the insert's curvature. Once dried the next glue layer, for the pad to lens, was applied once more with a syringe and the insert placed through the hole in the cell. As the glue layer came into contact with the lens it was forced to spread out creating an even layer. There was a noticeable colour change as the glue layer touched the lens giving a visible indication that there were no air bubbles in the glue layer and that there was contact over the entire pad. Figure 6.2 shows the pads glued into position on the lens.

6.2 Changes Required for the DECam Alignment

During the alignment of the prototype several difficulties were encountered that required modification of the alignment procedure for the successful alignment of the DECam lenses. New equipment was ordered and modifications were developed for the alignment rig.

The thicknesses of the RTV pads have been consistently difficult to determine. Micrometer readings can vary by up to 100μm as the pad compresses beneath the micrometer. When testing the compression modulus it was possible to measure the height by the difference of position of a microscope focussed on the pad and its plate. Unfortunately this method was too bulky a method to use on the cell itself as there is only a 15mm gap between the inside diameter of the cell and the edge of the sloped surface. Although the DDGIs fit easily into this gap they cannot take accurate measurements when moved over millimetre high objects. To overcome this, a non-contact probe that can fit in a 15mm gap was required and a laser displacement sensor was purchased that met these conditions.

The rotary table used for the prototype required replacing due to its small size; having diameter of 0.75m when an extension plate was placed on it, and old bearings. A rotary table was purchased from Rotary Precision Instruments that has a diameter of 1m, which

was extended to 1.5m by the addition of a top plate, and can take a load of up to 10 tons, far greater than the weight of the completed DECam. It runs on a thin film air bearing making it easy to turn and it has a run out of about one micron. Larger plates can be added if required for the alignment of the cells to the barrel.

Movement of the cell to the lens was a very time consuming task as each turn of the bottle jack only gave a small upwards increment, yet when levelling the cell it would often give too much movement when only a few microns was required. Therefore a system that has both coarse and fine adjustment is required. The cell can be raised part of the way by crane and struts put in underneath, but with a 2mm gap between the cell and the lens it must be done very precisely. Lab jacks, small platforms that can be raised with micron accuracy, have been brought to use for fine height adjustment. Hydraulic jacks and larger lab jacks that can be replaced with solid struts to prevent slipping are to be used to raise the cell the majority of the way with the micron accuracy lab jacks used for the final, fine alignment.

The standard socket screws used in the X and Y directional positioning worked well overall, although great care must be taken to ensure that the cell is not distorted. However those used on the prototype had angled ends, causing variations in how far a single turn would move the cell. To remove this issue differential adjuster screws with rounded ends that allowed an adjustment of 25μm per revolution were used for the alignment of the DECam lenses.

The bottle jacks supporting the cell were not ideal as although there were four supports the cell would determinedly insist on balancing on only two. This meant that it would easily unbalance and rock over, putting in a tilt and changing the decentre. The bottle jacks would often slip from their desired location, or their height would change in the process of locking them into position. As such it was decided that the cell would rest on a ring of ball bearings, allowing free movement in all directions; as the ball bearings were made of plastic and had some small compression there were more points in contact removing the rocking.

6.3 Deflection of Lens Due to Tilting

The ability of the RTV pads to hold the lens in position was tested by tilting the prototype. The flexures of the cell were attached an aluminium plate on the rotary table, a picture of

which is in figure 6.3. The rotary table could tilt by 40°, more than DECam's maximum angle operational angle of 30°. Measurements of the cell's and of the lens' movement were taken when the lens was inclined at 10° intervals between 0° and 40°. Both were measured with respect to the holding frame, so any movement of this structure would not be seen in the results. Table 6.1 shows that the FEA models and the experimental results agree very well, with no movement in the cell and the lens moving by a maximum of 10μm. The lens shifts within the cell causing the back of the lens, the side that has been lifted into the air, to move by a greater amount than the front of the lens, which is brought downwards into the RTV. The agreement between the FEA and experimental data from the prototype gives confidence that the FEA predictions for the DECam lenses, as in table 2.4, are accurate reflections of the eventual performance of DECam.

	Movement due to tilt	
	FEA prediction	Micrometer reading
Cell	0 μm	0 μm
Lens back	10 μm	10 μm
Lens front	4 μm	5 μm

Table 6.1: Comparison of the FEA and the actual deflections for both the cell and the lens when the cell is tilted by 40 °. The front surface of the lens refers to the side of the lens that has been tilted downwards from the nominal zero vertical point and the back surface is the side of the lens that has been tilted upwards from the nominal zero vertical point.

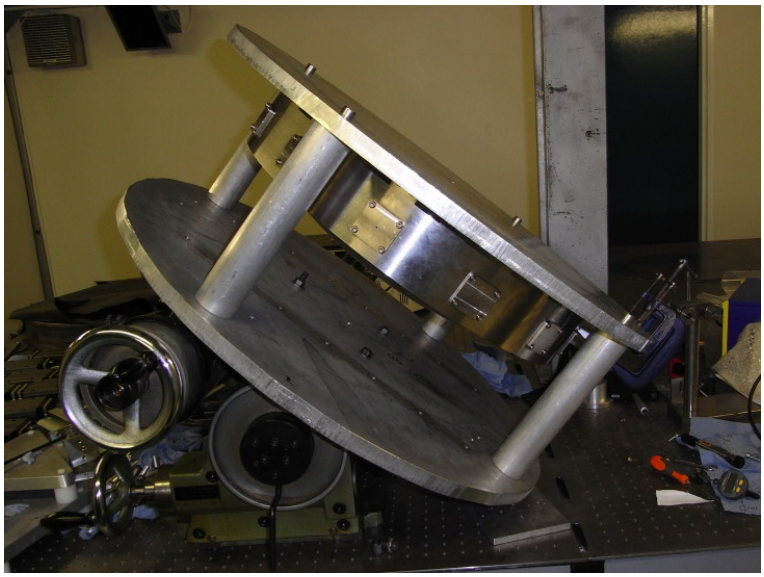

Figure 6.3: Picture of the prototype cell and lens undergoing the deflection due to tilting test.

6.4 DECam Alignment Rig

A new alignment rig was setup for the alignment of the DECam lenses. The rotary table is placed at the centre of the new alignment rig with an extended top which the alignment structure for the lens and cell is placed on. It is surrounded by a framework for the measuring devices as shown in figure 6.4; the long width allows multiple gauges to be placed over the lens and cell as required. The mirror seen over the centre of the framework is for sending a pencil laser beam down through the centre of the rotary table for the alignment of the lenses in the barrel.

Figure 6.4: Alignment rig for the DECam lenses. Here the rotary table can be seen with the new framework being erected.

6.4.1 Deformation of lenses due to the whiffletree support

Each lens must have its own whiffletree to support it with minimal distortions during alignment. The three smallest lenses (L2-L4) have a 9 point support and for the largest, L1, there will be a 18 point support. Nine point supports were used for the smaller lenses as there was no significant difference in the deformation between a nine and eighteen point support, with the nine point support being easier to manufacture and use. L1's large size required the eighteen support points. The equations to create the correct size whiffletree were for flat mirrors and so to ensure this support distribution would work for the curved lenses a FEA model was created to find the sag and stress produced. As the equations were for a flat mirror they did not take into account the change in thickness of the lens,

which creates an non-uniform mass distribution with an increase in the radial distance. In order to try and compensate for this the position of the supports were found by assuming that the lens was a flat disc that had the depth of the lens' central thickness. By knowing the mass density of the fused silica a false maximum diameter was used to produce the diameter of the lens, D_l. The placement of the inner supports is at a diameter[59], D_i, of

$$D_i = \sqrt{D_l^2/6} \tag{6.1}$$

with the placement of the outer supports at a diameter[59], D_o of

$$D_o = \sqrt{2D_l^2/3} \tag{6.2}$$

When an eighteen point support is used, as for C1, then the distance between the two outer supports on the same place is at a distance[59], S, of

$$S = D_o \sin 15^\circ \tag{6.3}$$

The radii found from these equations were then used to generate the FEA model. A 50mm diameter pad made from Delrin was centred over the expected radius and the stress and distortion were calculated. These results can been seen in table 6.2.

Lens	Inner Radius	Outer Radius	Max Stress (MPa)	Distortion (mm)
L1	193	319	0.13	0.00010
L2	144	290	0.07	0.00011
L3	116	232	0.05	0.00016
L4	108	217	0.08	0.00010

Table 6.2: Overview of the size required for the whiffletree and the stress the lens will be put under and the distortion it causes. The radii given is the central position of the pad. The Young's modulus of the fused silica is 72.7GPa, with a shear modulus 31.4GPa[38].

6.5 Wedges

The wedges present on the lenses were originally measured by SESO and then confirmed at UCL by Dr Brooks. In order to produce the optimal image quality, Sue Worswick performed an optimisation on the wedge alignment using ZEMAX optical software to determine the best alignment of the wedges with respect to each other. Figure 6.5 shows

the result of this optimisation where the triangles represent the lenses and the straight line represents the sloped axial surface of the cell. The angled side of the triangle shows the side that wedge should be placed on relative to the cell. All of the wedges should ideally be aligned with the large side of the wedge at south except for C2 which is rotated by 180° and is aligned to the north.

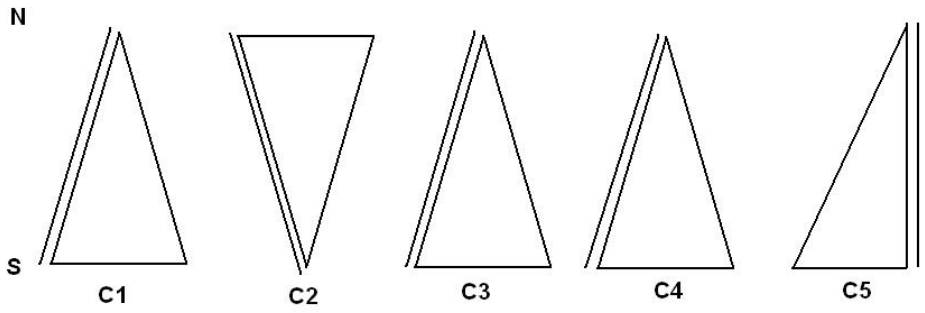

Figure 6.5: Schematic of the lens' wedge alignments.

6.6 C5 Alignment

The first lens to be aligned was C5. As this lens also acts as the cryostat window, it was necessary for testing under vacuum to be done. Firstly, this would ensure that it would not crack under pressure. Secondly, as the cryostat will be cycled during the lifetime of the survey, this will ensure that this process does not cause movement of the lens. It is also necessary to measure the amount the lens sinks on the O-ring to ensure the proper separation between C4 and C5 during telescope operation.

The cell for C5 is significantly different in design and composition to the other cells. It was designed and made by Argonne National Laboratory and shipped to UCL for alignment along with a test vacuum chamber. The cell is made from stainless steel, with a single O-ring to create the vacuum seal, and plastic mounts to prevent movement of the lens during cycling of the vacuum. Plastic stops fit over the mounts to prevent movement of the lens when not under vacuum. These features can be seen in figure 6.6.

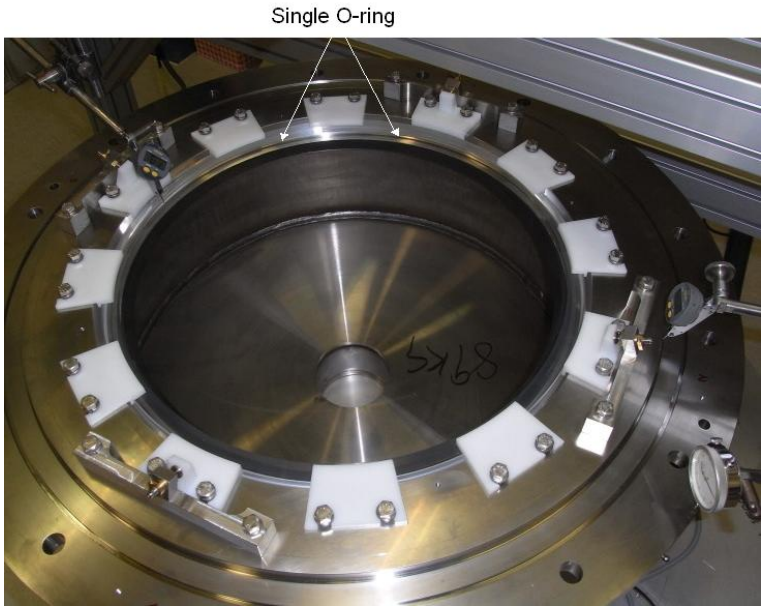

Figure 6.6: Picture of the C5 cell, with the lens aligned within it ready for attachment to the barrel. A single O-ring provides the resting surface for the C5 lens and the vacuum seal. White plastic mounts are used to maintain C5's alignment during vacuum cycling.

6.6.1 Lens to cell alignment

Figure 6.7 shows the lens being lowered into the whiffletree, surrounded by its handling tools. Underneath, the C5 cell can be seen sitting on another ring which contains ball bearing for X-Y positioning. Once the lens was placed on the whiffletree the handling tools were removed from the lens leaving it clear for alignment. A picture of this is shown in figure 6.8.

The lens was clocked and centred to the rotational axis of the rotary table. The cell was then raised until the O-ring was approximately 200μm away from the lens. The cell was then clocked and centred. Figure 6.9 shows the clocking of C5. Once aligned the cell was slowly raised to bring it into contact with the lens, clocking during the process to ensure the cell was not moving in X or Y. The cell was raised until it was taking the full weight of the lens and the whiffletree was free to move. The cell was levelled and centred and the lens was found to be aligned to 10μm in decentre and 40μm in tilt.

6.6.2 Vacuum cycling tests

The C5 lens and cell were then placed onto the vacuum chamber and cycled through vacuum. For each cycle, the deflection of the lens due to the vacuum was measured and

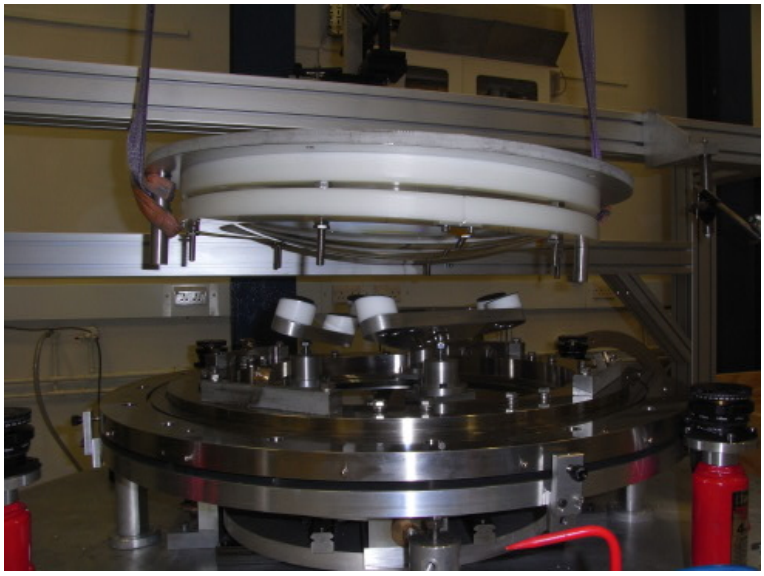

Figure 6.7: Lens 5 being lowered onto the whiffle pads for alignment.

any change in the position of the lens with respect to the cell was noted. Figures 6.10 and 6.11 show the lens undergoing this process. Measurements were taken from surface 1, the surface of the lens facing outside of the vacuum chamber, on the lens flat at the edge of the lens and at the centre of the lens. It was found that the lens moved by approximately 750μm due to compression of the O-ring and deformation at the centre of the lens was 30-40μm, agreeing with FEA predictions. Surface 1 of the lens did not decentre or tilt by more than 36μm, which is well within the specifications, as given in table 2.5.

After the vacuum cycling tests were complete the lens-cell system was removed from the vacuum chamber and stored for later attachment to the barrel. Figure 6.9 is the completed lens-cell system.

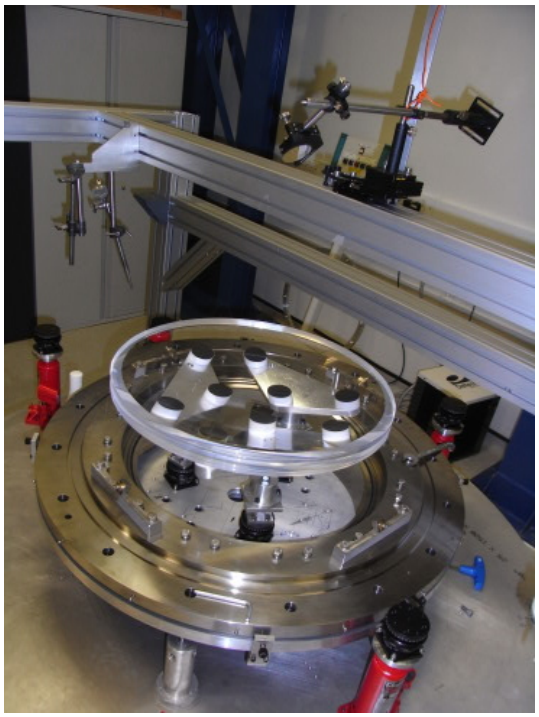

Figure 6.8: Lens 5 aligned, with the cell in the process of alignment.

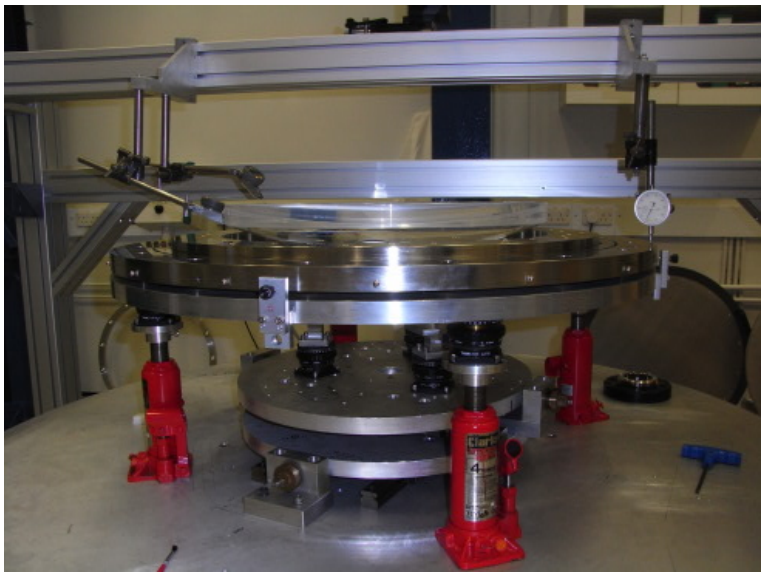

Figure 6.9: Lens and cell being brought into contact.

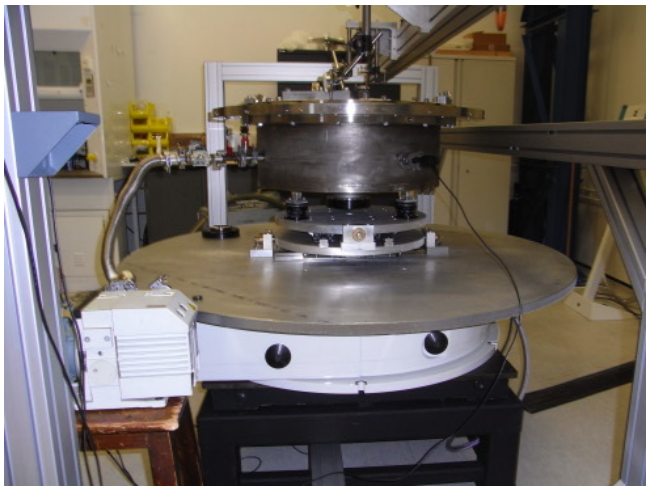

Figure 6.10: Lens 5 undergoing the vacuum test.

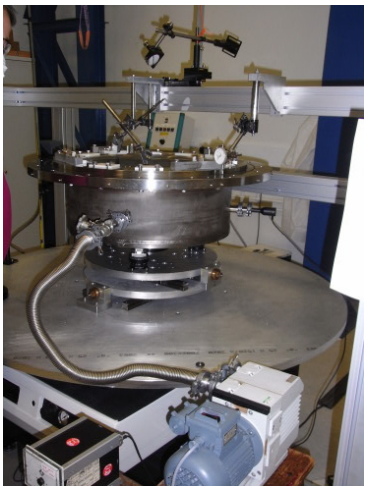

Figure 6.11: Lens 5 undergoing the vacuum test.

6.7 C2 alignment

The next lens to be aligned was C2. Whilst the diameter of this lens is significantly smaller than the C1 lens it has by far the largest edge thickness.

6.7.1 C2 axial pads

As already mentioned C2 sustained damage around the edge of the lens that required a custom pad to keep the axial pads equally spaced. The damage was mapped at UCL to determine what room there was to fit in the axial pads, as shown in figure 6.12. The damage extended over 30°, meaning that to keep the axial pads evenly spaced it was necessary to have one pad in the damaged area. However over the entire damaged area the chamfer on the lens had been extended out meaning a 10mm by 10mm pad would be too wide. It was found that there was an area large enough to fit a pad which was half the width but twice as long (20mm by 5mm), keeping the same S factor as the square pads. This elongated pad is shown in figure 6.14 which has been aligned under the correct insert for the wedge to sit in the required orientation.

Once the pads had been glued onto the cell the laser displacement sensor was used to determine the height variation in the pads, as in figure 6.15. It was found that the pads had a variation of $\pm 25\mu$m as in the graph in figure 6.16. This amount of variation is taken up fully by the compression of the pad under the lens weight.

6.7.2 Lens to cell alignment

The cell was then placed on the rotary stage and the lens onto its whiffletree. The lens was levelled and centred to the rotational axis using clocking to 5μm. The cell was then raised until the axial surface was approximately 0.5mm away from the lens and then roughly aligned. The cell was then raised until it was about 200μm from the lens and aligned so the cell was within 4μm of the rotational centre. It was then raised until the lens had moved off the whiffletree and was completely supported by the cell. The lens was then levelled, again to about 5μm, and the cell was found to be level with a decentre of 9μm.

To determine the cell's position with respect to the rotational axis maps were created that showed the measured run-out of the mating ring when attached to the barrel at Fermilab. These were then matched against the run-out of the mating ring during alignment and the cell was aligned when it matched the positioning at Fermilab. Figure 6.17 shows

the map for the alignment of C2 before and after the cell was in contact with the lens. There are two lines for the run-out that should be aimed for, one where it was aligned off of the barrel and one where it is on the barrel. As can be seen, there appears to be some distortion of the ring when it is attached to the barrel.

6.7.3 Gluing the lens into position

Once the cell took the full weight of the lens the distances between the lens and cell were measured at each insert. This then allowed the inserts to be individually milled to the correct thickness for the radial pad to give an athermal system. The radial pads were placed on a block with the same radius of curvature as the insert and had a thin even glue layer bladed onto them. The insert was place on top and left to cure. A picture of the pads glued to the inserts is shown in figure 6.19. The extra surface area of the inserts is painted black, shown in figure 6.20, to match the cell and reduce reflected light in the system.

Once all the inserts have had a radial pad glued on and painted, they were placed into the cell. Paper was used to fill the space between the lens and the radial pads. Opposite inserts are removed and a glue layer equal to the size of the gap between the lens and the cell is bladed on as in figure 6.21. After each pair of inserts was glued to the lens the positioning was rechecked to ensure that there was no movement of the lens in the cell. The graph detailing this is in figure 6.22.

The majority of the radial pads had good glue layers but two inserts had incomplete coverage when attaching to the lens. In these cases the incomplete glue layers caused gaps at the edge of the radial pad and the lens, as shown in figures 6.23 and 6.24. In both cases the air gap is at the edge of each pad so no air is trapped between RTV and the lens. It is not thought that these air gaps will have any bearing on the effectiveness of the radial pad to hold the lens in position or on athermal design. A picture of the C2 lens and cell glued together is in figure 6.25, ready to have the C3 cell and lens attached to it before being placed in the barrel.

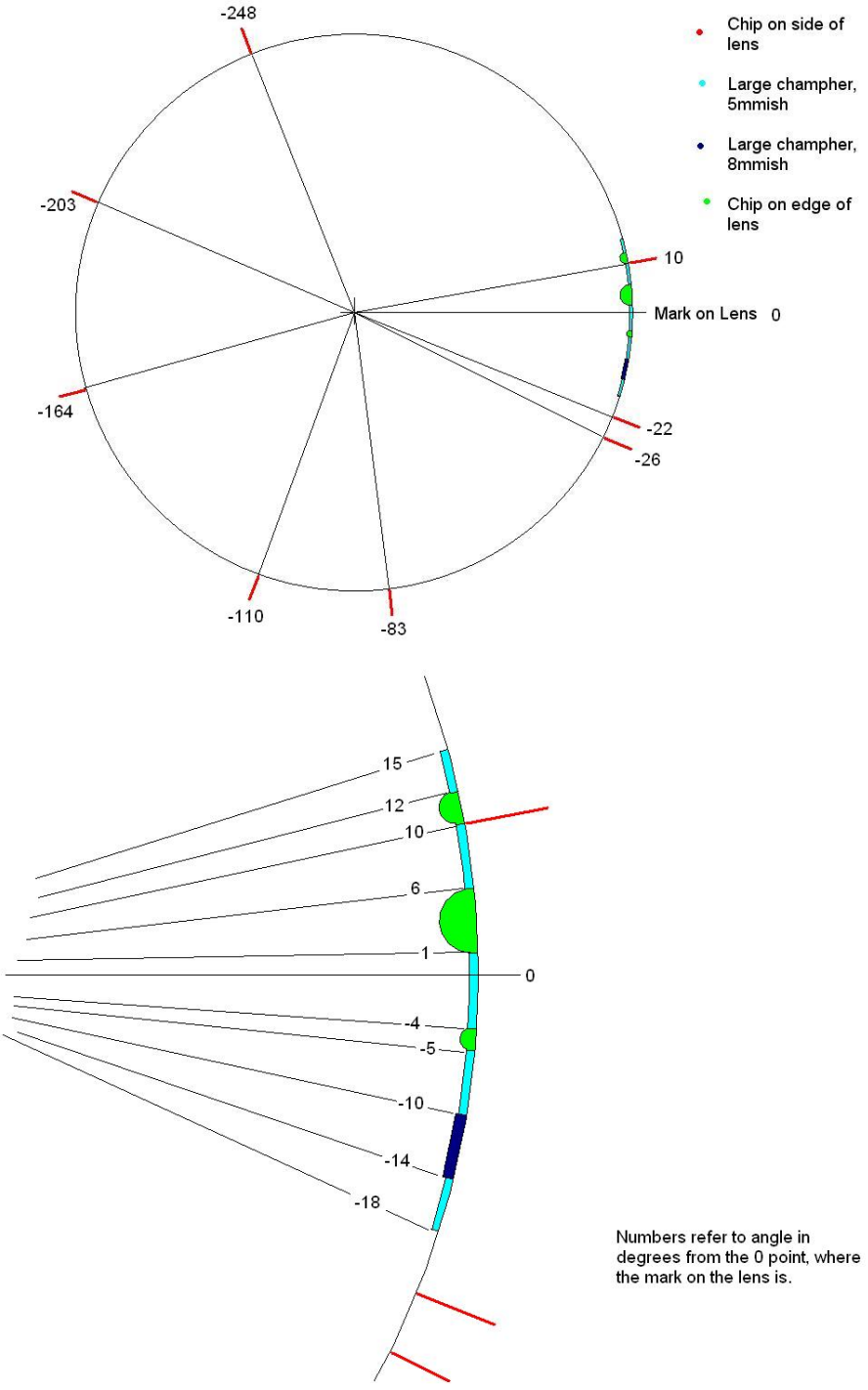

Figure 6.12: Map of all the damage on L2 as measured at UCL. This map was used to orientate the lens to avoid axial pads sitting on a damage surface, risking a lack of contact at that point.

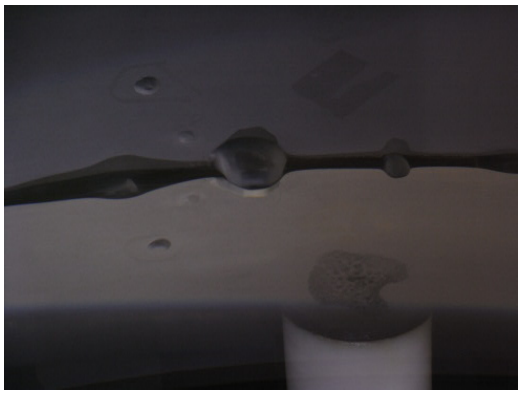

Figure 6.13: Damage to Lens 2

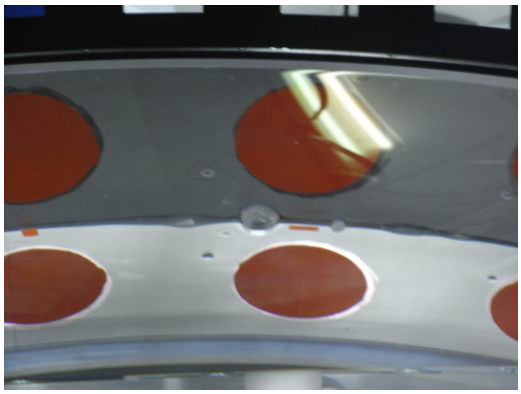

Figure 6.14: Positioning of pads around the damaged area.

Figure 6.15: Measuring the height of the axial pads on C2. A non-contact method was used to avoid small compression in the pad masking height variaitons.

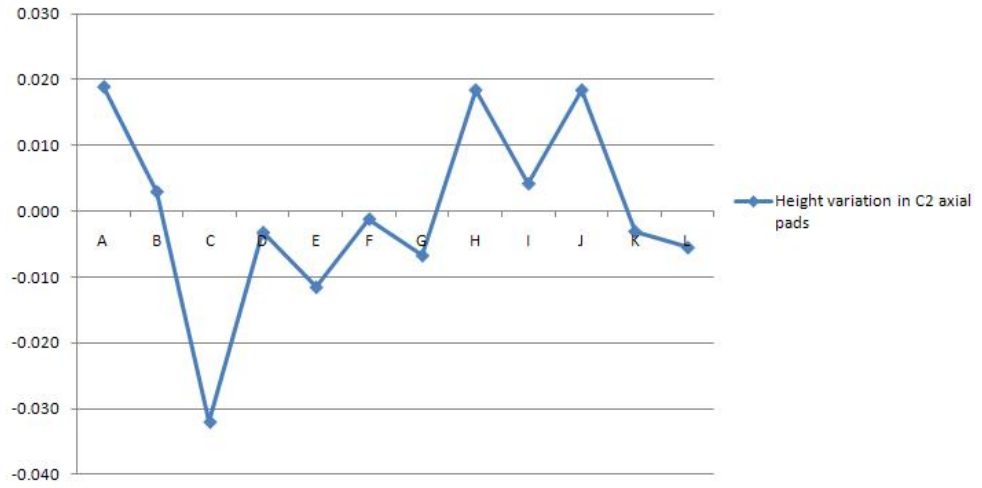

Figure 6.16: Height variation of the C2 axial pads. Units are in mm. The letters refer to the holes in the cell where the radial pads will be inserted. Axial pads were placed in the centre of these insert holes and were so labelled for the insert under which they sit.

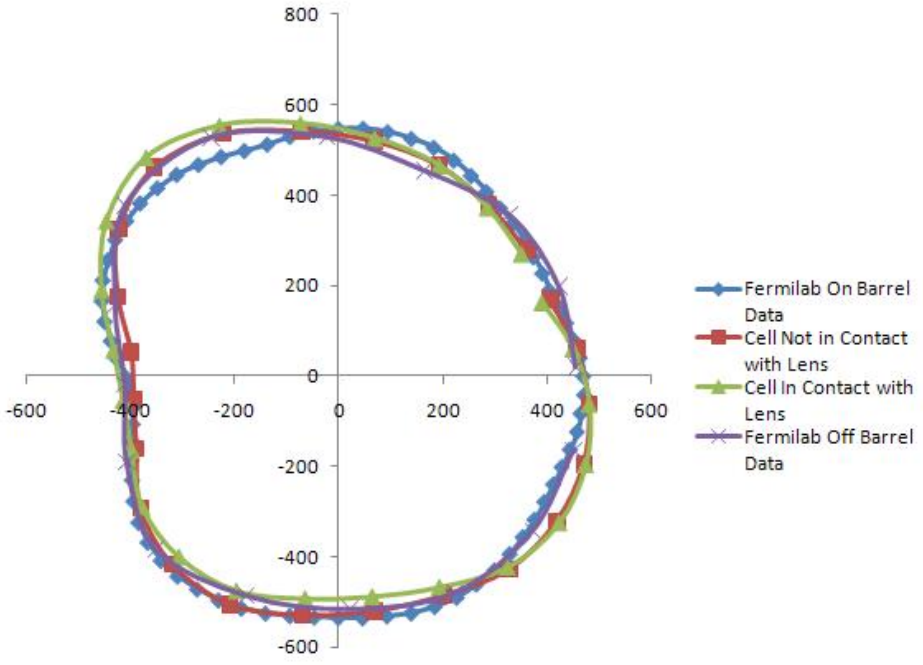

Figure 6.17: Alignment map used to align the C2 cell. Units are in μm.

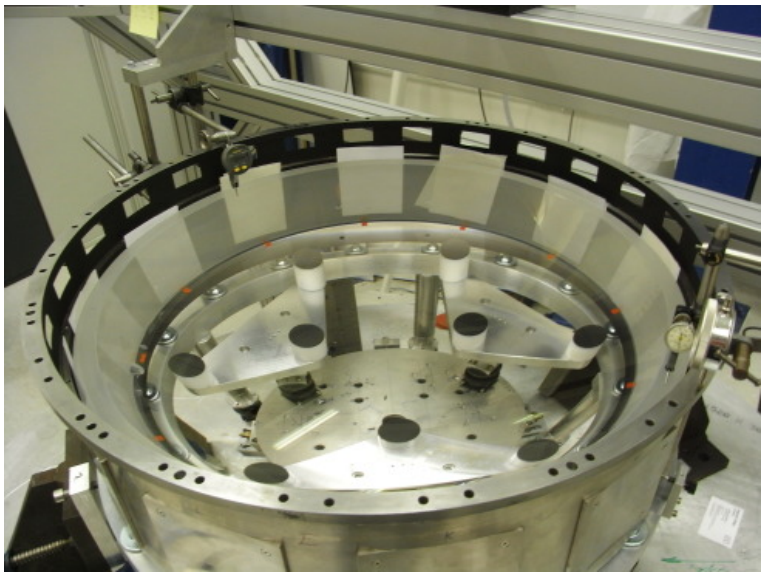

Figure 6.18: Lens 2 in its cell.

Figure 6.19: Radial pads glued to their inserts ready for painting.

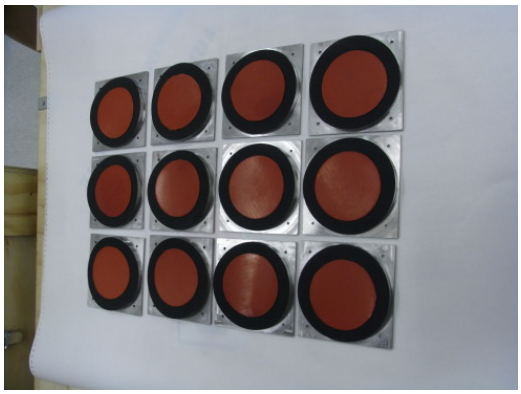

Figure 6.20: Radial pads glued to their inserts complete with black paint to match the cell. Another layer of glue will be added just before attaching to the lens.

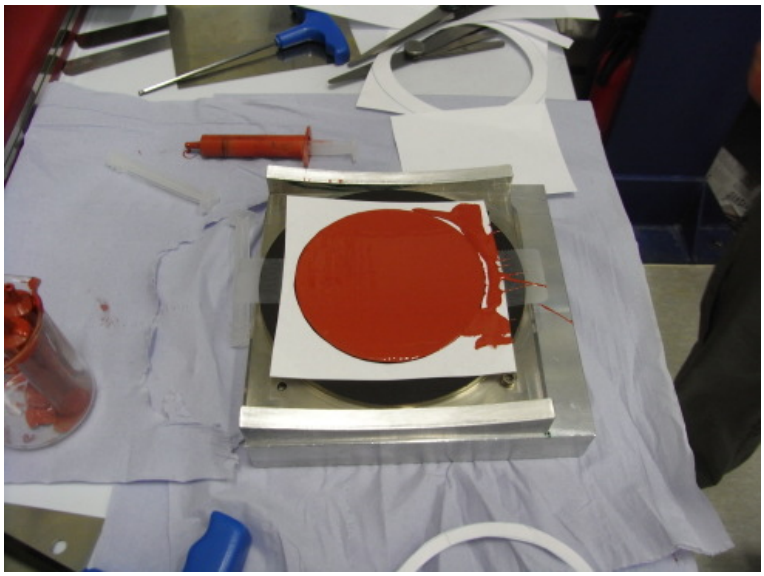

Figure 6.21: Blading technique used to ensure an even layer of the rubber solution over the pad. The height of the guides at the edge ensure that just enough glue is used to fill the gap between the lens and insert, reducing excess and preventing stresses and spillage. The white paper is peeled off before the insert is placed in its hole.

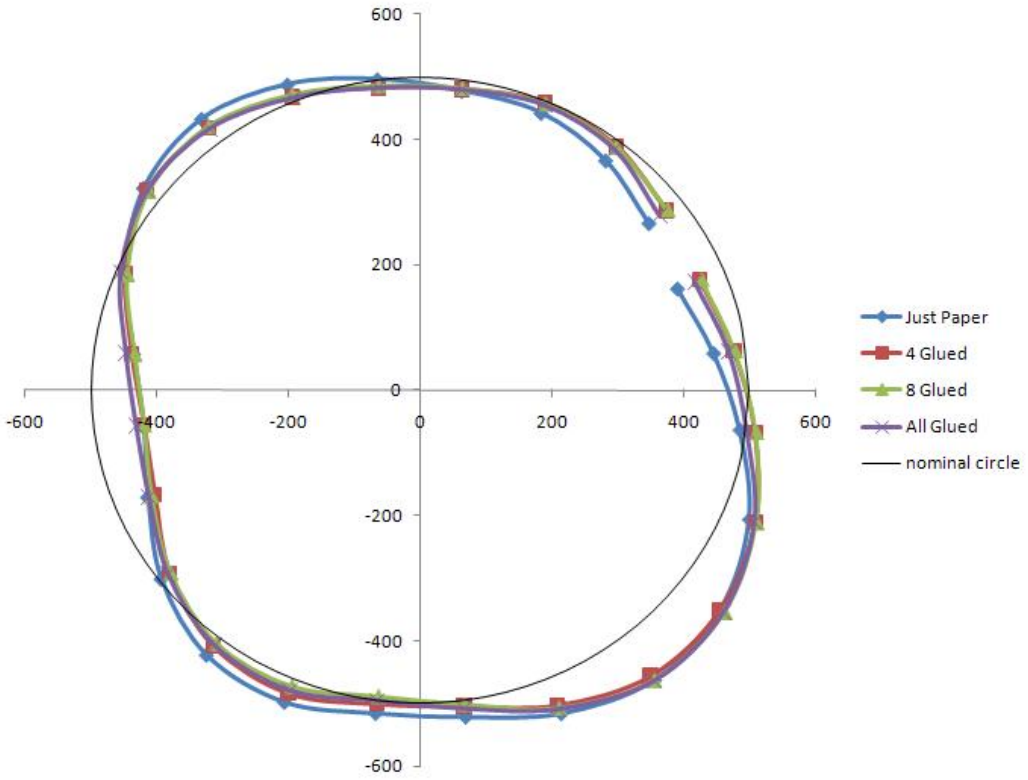

Figure 6.22: Graph showing the change of shape of the outer diameter of the retaining ring as the inserts are glued to the lens. Units are in μm.

Figure 6.23: Picture of the first incomplete glue layer between the lens and the radial pad.

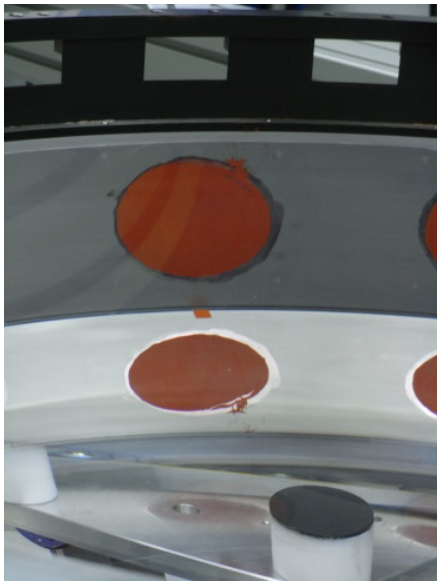

Figure 6.24: Picture of the second incomplete glue layer between the lens and the radial pad.

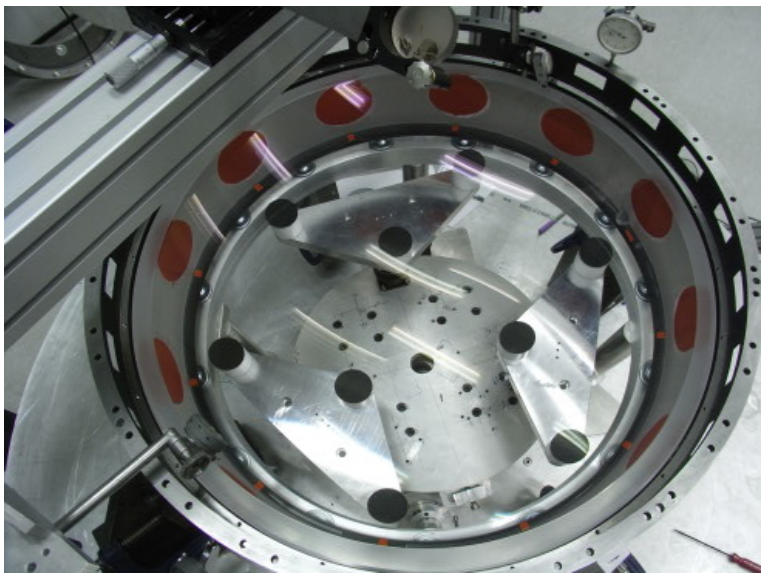

Figure 6.25: The completed alignment of lens 2 into its cell. It is ready to be mated with C3 before its alignment into the barrel.

6.8 C3 Alignment

A pre-alignment check found that the outer diameter of the mating surface on the C3 cell was too large and so did not fit into C2. As such the C3 cell had to have the outer diameter of the mating ring reduced by 2mm, also requiring a remapping of the axial sloped surface to the outer ring diameter.

The C3 lens was placed in its cell several times. This allowed the C2-C3 lens distance to be controlled to 50μm. No shims are to be used between these two lenses. For the first alignment the lens and cell were not glued into position, but placed on top of C2. This allowed measurement of the spacing between surface 1 of C3 and surface 2 of C2. This distance is required to be 95.360±0.025mm and so some removal of material from the bottom of C3 was expected to be needed. The measured distance from the top of the C3 ring to the base of the sloped axial surface was 23.39mm rather than the expected 22.50mm. This is too much material to be removed by grinding alone. As such, it was decided to reduce the height of the axial pads by 0.5mm to lower the lens. After this change it was found that 644μm was required to be removed from the base of the cell to reach the target distance.

6.8.1 Axial pad heights

The initial 2mm thick axial pads were removed to be replaced with 1.5mm thick pads. As pads had been cast into 0.9 and 1.9mm thicknesses, a 0.6mm glue layer was initially tried with a 0.9mm pad. The large glue layer caused the pads to easily slide and uneven glue layers with high variation were produced. These pads were removed and the moulds used to produce the 1.9mm thick pads were remachined to produce pads 1.4mm thick. A glue layer of 100μm brought the total height of the pad up to 1.5mm which when glued to the cell had an average height variation of ±35μm, graphs of which are shown in figures 6.26 and 6.27.

6.8.2 Alignment of lens to cell

To determine the centre of the cell the run-out of the outer diameter of the mating ring was measured when the sloped axial surface was aligned to the rotational axis of the rotary table. This can be seen in figure 6.28, which is the map used to align the cell. As C3 attaches directly to C2, it acts as the retaining ring for the C2 lens. This meant that it

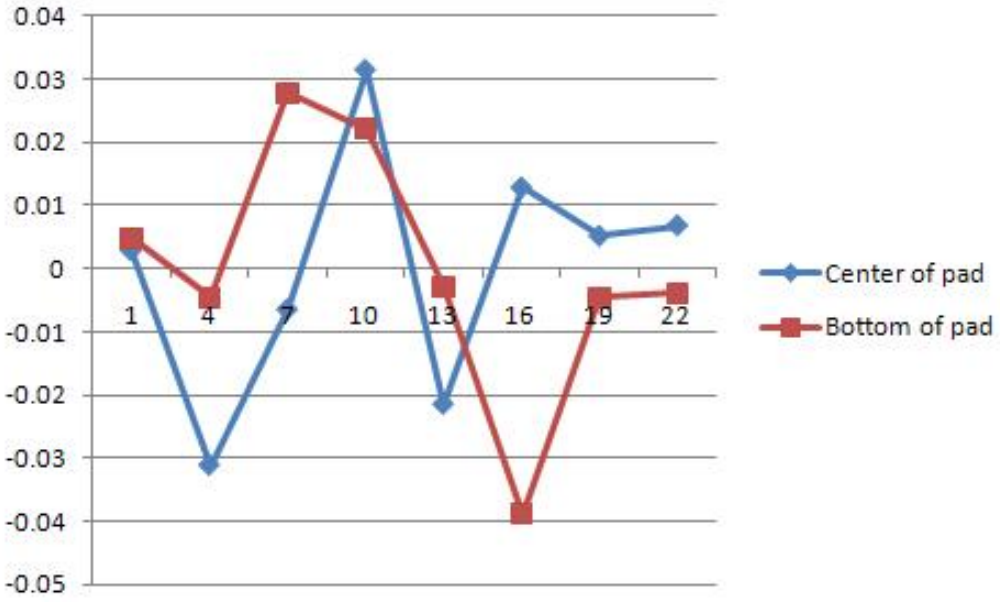

Figure 6.26: Graph of the average height of the C3 axial pad taken at two positions, across the centre of the pad and across the bottom of the pad. Units are in mm on the Y axis, with the X axis being unit-less flexure numbers.

required retaining pads to be placed on the underside of the mating ring, in case of lens movement during transit. The pads were glued to the underside of the C3 ring by placing the pads on the edge of the C2 lens with a glue layer on the uppermost side of the pad. Primer was placed on the appropriate places on C3, before being lowered onto C2 and left for the RTV to cure. This process then fixed the alignment of the C3 cell to the C2 cell; as if they were rotated with respect to each other any height variations could cause the RTV retaining pads to come into contact with lens, creating an uneven pressure. This created the north-south axis to the alignment of the lens wedge as given in section 6.5. The rest of the alignment procedure remained the same as for C2.

6.8.3 Attachment of the radial pads

The method used to attach the radial pads to C2 also used for C3, although there were twice as many inserts, and much smaller than C2's. The gluing of the radial pad to the insert was slightly more difficult on these smaller pads as the insert's diameter was only approximately 2mm larger than the pad, giving little room for slippage during curing.

A picture of the completed C3 lens-cell is shown in figure 6.29, ready to be aligned with C2. When the lens is aligned to the rotational axis and levelled the cell has a decentre of 4μm with respect to the lens.

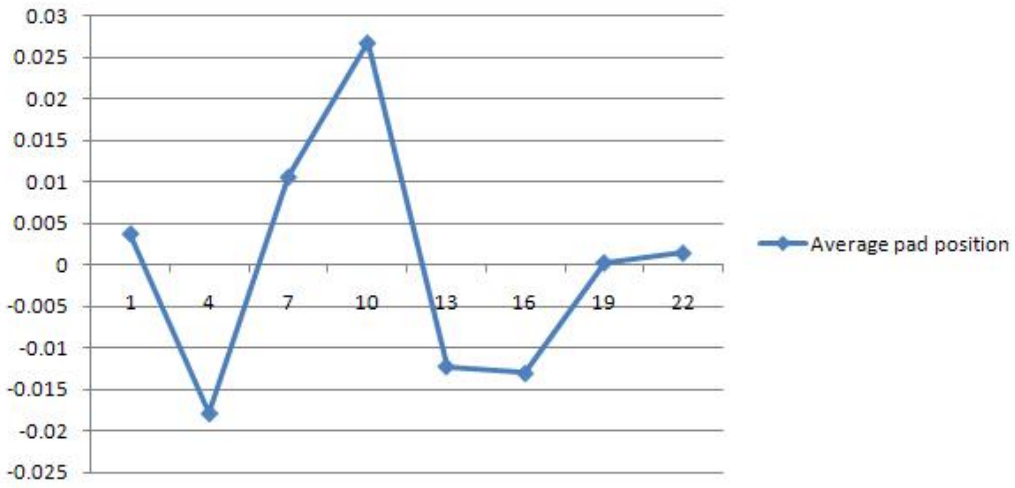

Figure 6.27: Average variation over the whole pads in the height of the C3 axial pad. Units are in mm on the Y axis, with the X axis being unit-less flexure numbers.

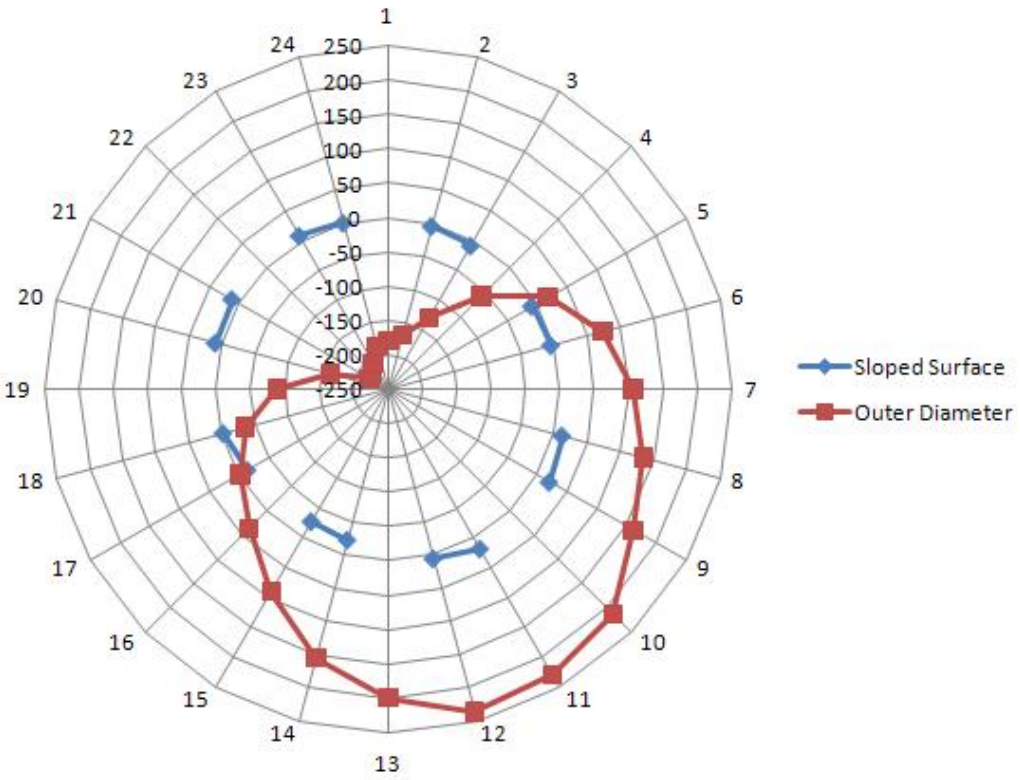

Figure 6.28: Map of the run-out of the outer diameter of the mating ring on C3 to the sloped surface. The sloped axial surface is not a continual ring as the pads interrupted the measurement of the axial surface. Units are in μm on the central axis, with the outside axis being unit-less flexure numbers.

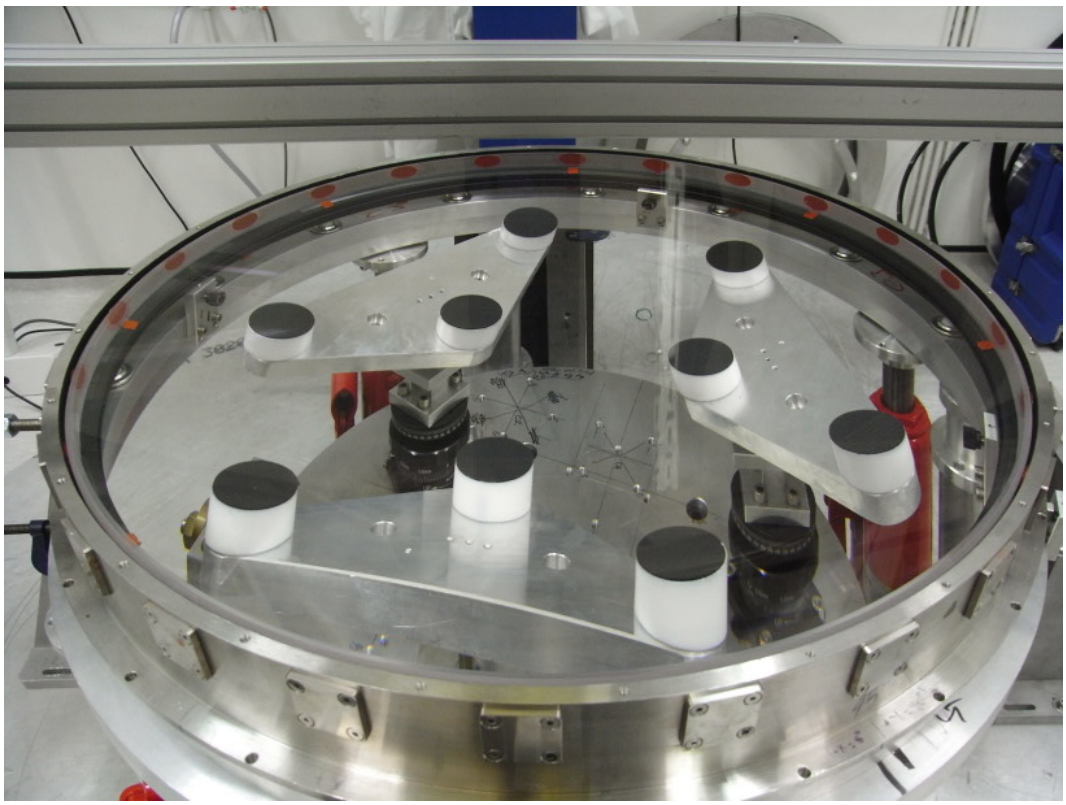

Figure 6.29: Cell C3 with all radial pads attached.

6.9 C4 Alignment

C4 was aligned whilst the C3 cell was away for grinding. It was hoped to align this lens first due its small size but delays in the shipment of the lens prevented this from occurring.

6.9.1 Axial pad heights

The pad height of the C4 axial pads when cast were 1.9mm with 0.1mm added in the glue layer. These were glued on to the sloped surface which is angled at 26.7°. This large angle gave some difficulty in the gluing process as the pad would slide on the steep surface, creating uneven pad heights. The initial variation was found to be 125μm. As the expected compression was 120-130μm, this was too large a variation to accept. Two pads with high readings were removed and replaced and three pads had an extra glue layer bladed on top to increase their height. In two instances the blading worked but on the third the RTV layer did not bond properly and so pealed away. This pad was removed and a fresh pad glued into its place. Whilst the two originally replaced pads had new heights that were acceptable, the two bladed pads and the last replacement pad were all too high. Rather than replacing them again, it was decided to try and sand down these three to the bring their height into line with the other pads. The final height variation of the axial pads at three different radii is shown in figure 6.30 with the average height variation of ±40μm shown in figure 6.31.

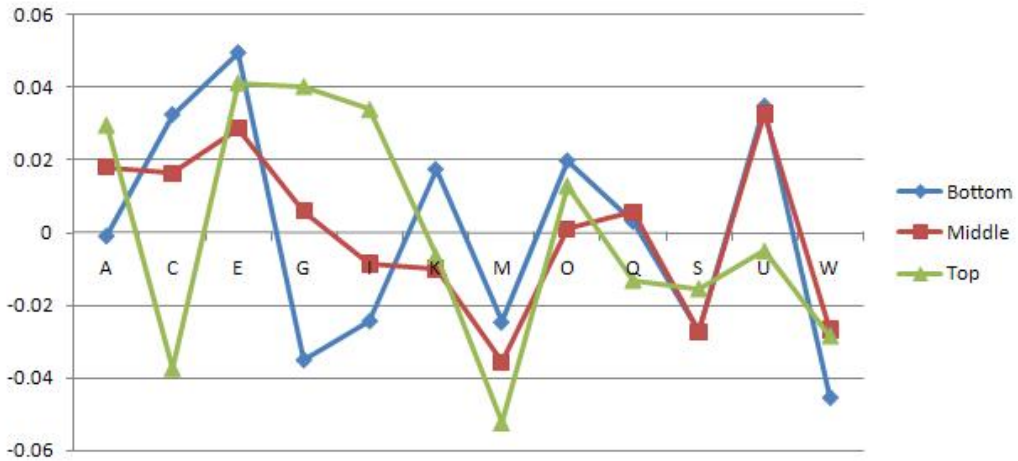

Figure 6.30: Height variation of the C4 axial pads taken at different radii. Top defines the readings taken nearest the inner diameter of the cell wall. Units are in mm.

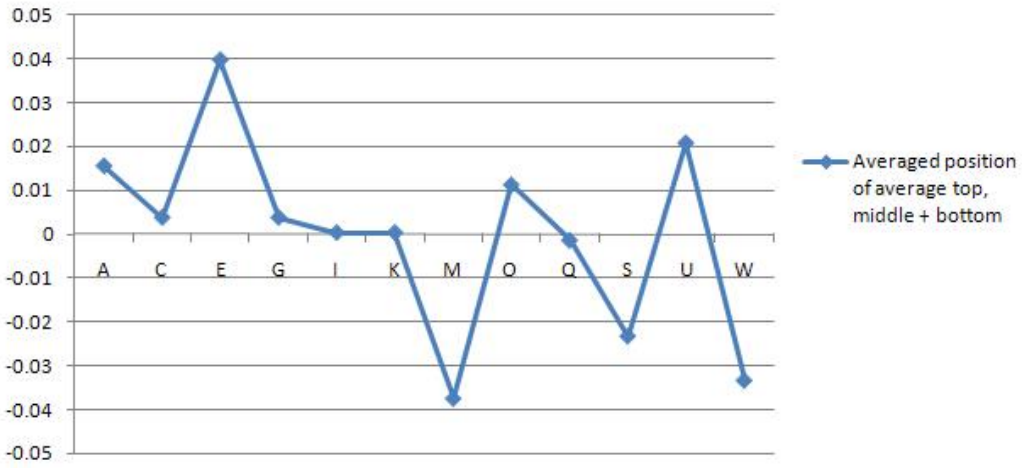

Figure 6.31: Average height variation of the C4 axial pads. Units are in mm.

6.9.2 Alignment of lens to cell

C4's cell to lens alignment process was the same as for C2 and C3, with figures 6.32 and 6.33 showing the lens and cell going through the clocking and raising stages. However, once the lens was sitting in the cell and the cell was centred and levelled, the lens had a 40μm tilt with a 20μm decentre. The tolerances on C4 are no more than a 58μm tilt and 100μm decentre. Conclusions drawn from work in Chapter 7 shows that a tilt on C4 effects the image quality much more than a decentre. Therefore it was decided to try and use a decentre to compensate for the tilt. The C4 cell was decentred by 50μm from the rotational axis and then raised into contact with the lens, which had been centred to the rotational axis. Once the cell was taking the lens' weight the cell was then centred to the rotational axis and levelled so it had no tilt. The position of the lens was then measured and it was found to have a tilt of 8μm and a decentre of 9μm with respect to the cell.

6.9.3 Attachment of the Radial Pads

The process for gluing the radial pads is as for C2, with the pads glued first to the inserts, six of which are shown in figure 6.34, and then all placed into the cell with paper between the pad and lens. Opposite inserts were then removed and placed into a blading rig as shown in figure 6.35.

Twice too much glue was applied and excess leaked out down the side of the lens, as in figure 6.36, with the completed lens-cells system pictured in figure 6.37. Once all the radial pads had been glued into position and fully cured the centring of the lens and cell

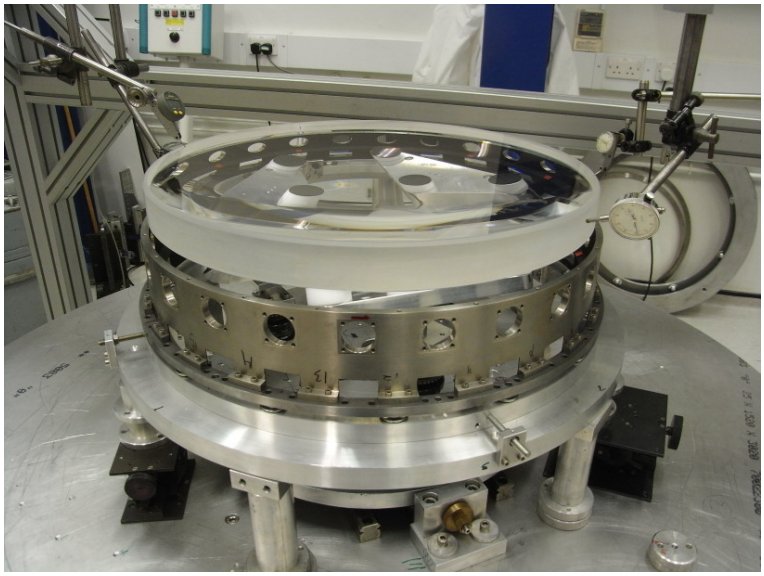

Figure 6.32: The C4 lens and cell on the alignment rig. The lens is being clocked and aligned.

was checked. The cell was centred to the rotational axis and the mating ring ran level. The lens was found to have a tilt of 18μm and a decentre of 3μm with respect to the cell.

6.9.4 Attaching the retaining ring

Before C4 can be aligned within the barrel the retaining ring must be attached. Thin pads were placed on the lens with a glue layer facing upwards as shown in figure 6.38. Primer was applied to the retaining ring in the appropriate places, placed on top of the pads and left to cure, as in figure 6.39, where a retaining pad can just be seen between the ring and lens. After curing C4 was stored until attachment to the barrel.

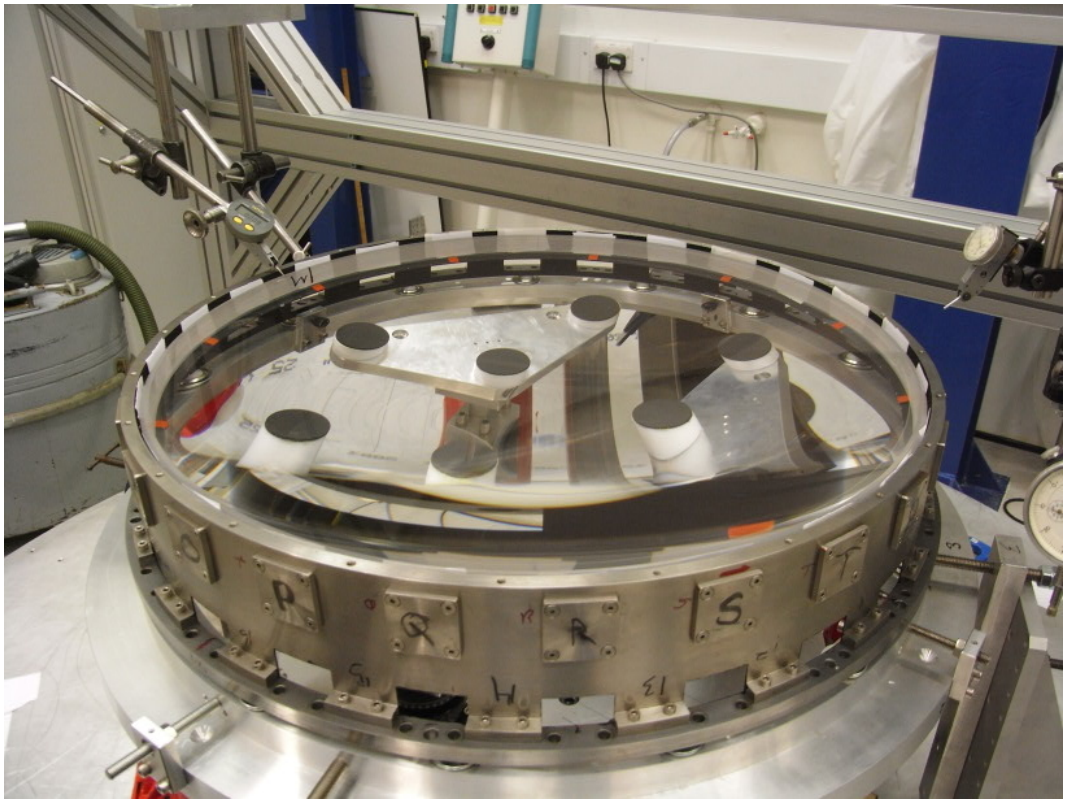

Figure 6.33: The C4 lens and cell on the alignment rig. The cell is being brought up into alignment with the lens. The micrometer on the lens indicates any movement in the lens.

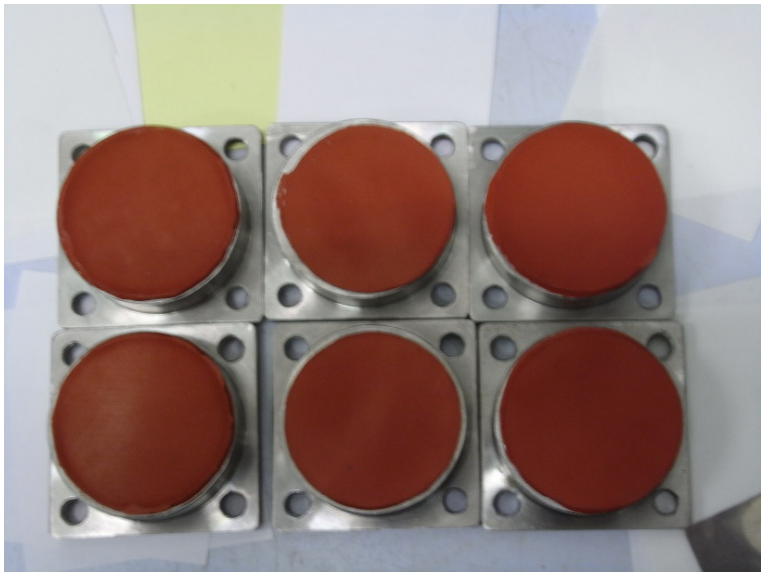

Figure 6.34: Six of the radial pads for C4, glued to the inserts.

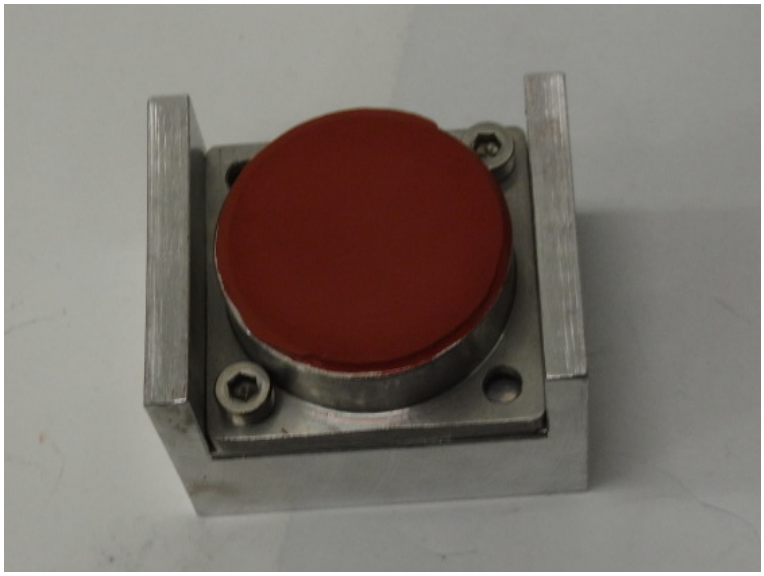

Figure 6.35: One insert in the blading rig. It is ready to have a mask placed over it to catch excess glue during the blading process.

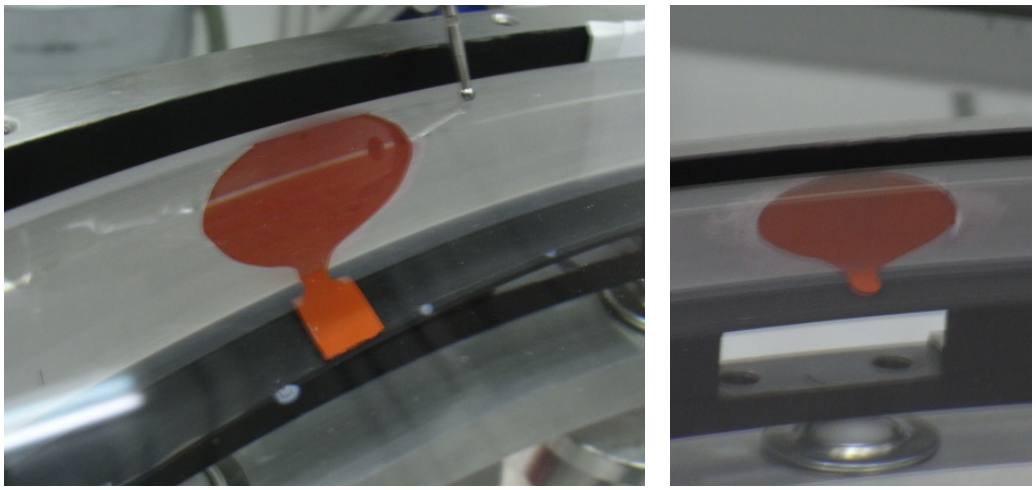

Figure 6.36: Two imperfect radial pads, both were glued with two much excess. On the right the excess has joined with the axial pad below. On the left it has just formed a drip on the side of the lens.

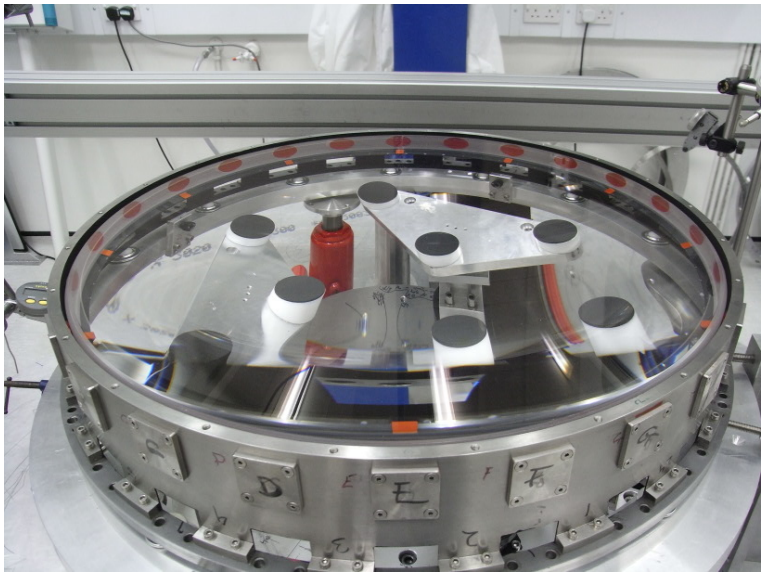

Figure 6.37: Image of the C4 cell with all of the inserts in place.

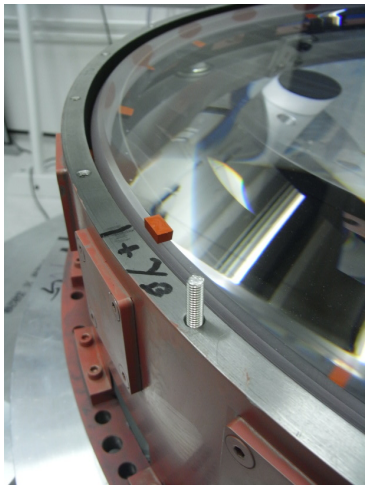

Figure 6.38: Image of a single retaining pad with its glue layer resting on the lens.

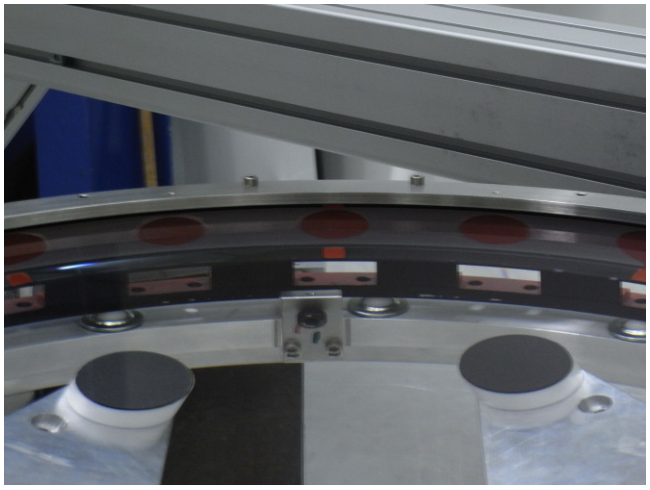

Figure 6.39: The retaining ring has been placed on the C4 cell. At the centre of the picture the retaining pad can just be seen.

6.10 Comparison of Alignment to Specifications

In table 6.3 the alignment of all the lenses that have been glued into the cells are compared with the specification requirements for the lens to cell alignment. It can be seen that all four lenses have been aligned to within the specified mechanical tolerances, mostly to very high precision.

Lens	tilt specification (μm)	actual tilt (μm)	decentre specification (μm)	actual decentre (μm)
C2	± 31	<10	± 12.5	12
C3	± 29	<5	± 25	4
C4	± 33	18	± 25	3
C5	± 75	<20	± 100	<70

Table 6.3: Specification of the mechanical assembly tolerances for the lens to cell[40], compared against the actual alignment of the DECam lenses in their cells.

Chapter 7

The Effect of Misalignment of the Lenses on the Weak Lensing Data

First, solve the problem. Then, write the code.

John Johnson

This chapter investigates the effect of non-perfect alignment of the lenses. Whilst the lenses will not be glued until they are within tolerance, absolutely perfect alignment is not possible. The DECam design was optimised using the RMS spot size whereas weak lensing looks at the distortion of the shape of the image. Therefore this chapter looks at the effect of lens misalignment on the shear and flexions of the point spread function (PSF), as these are used in weak lensing calculations. The expected image quality is compared to the theoretical limits for the weak lensing science that will be performed with the camera's images.

Weak lensing allows a direct measurement of mass along the line of sight between the Earth and distant galaxies. By measuring the distortion of the shape of the galaxies it is possible to create a dimensionless convergence mass map, κ, that gives the density of the matter between the galaxy and Earth[8][60]. The most common method is to use the shear, a measurement of the elongation of a galaxy. This is effectively modelled as a matrix distortion of the entire galaxy image where the position of an unlensed galaxy (x_u y_u) is

related to the position of a lensed galaxy at $(x_l\ y_l)$ by[61]

$$\begin{pmatrix} x_u \\ y_u \end{pmatrix} = A \begin{pmatrix} x_l \\ y_l \end{pmatrix} \tag{7.1}$$

where A is

$$A = \begin{pmatrix} 1 - g_1 & -g_2 \\ -g_2 & 1 + g_1 \end{pmatrix} \tag{7.2}$$

and g represents the reduced shear. A positive shear in the g_1 direction stretches the galaxy along the x axis and compresses it in the y axis. A positive shear in the g_2 direction stretches the galaxy diagonally, along the y = x direction, and compresses it along y = -x[61]. When flexions are considered the second order effects are examined. Equation 7.4 is expanded using [62]

$$g \equiv \frac{\gamma}{1 - \kappa} \tag{7.3}$$

where γ is the shear. This gives the new matrix to be[62]

$$A(\theta) \equiv \begin{pmatrix} 1 - \kappa - \gamma_1 & -\gamma_2 \\ -\gamma_2 & 1 - \kappa + \gamma_1 \end{pmatrix} \tag{7.4}$$

These second order effects come from the false assumption made in the shear calculations that the shear and convergence are constant over a source galaxy image[60]. It is possible for the flexion to be expressed as a gradient of the shear where the first flexion, F, relates to the shear by[63]

$$F = \delta^* \gamma = (\delta_1 \gamma_1 + \delta_2 \gamma_2) + i(\delta_1 \gamma_2 - \delta_2 \gamma_1) \tag{7.5}$$

and the third flexion, G, relates by[63]

$$G = \delta \gamma = (\delta_1 \gamma_1 - \delta_2 \gamma_2) + i(\delta_1 \gamma_2 + \delta_2 \gamma_1) \tag{7.6}$$

In order to calculate the shear values the elongation of the image is measured using quadrupole moments. The initial stage is to measure the central position of the galaxy by

its image brightness, I(x,y), using its first moments[61]

$$\overline{x} = \frac{\int I(x,y)xdxdy}{\int I(x,y)dxdy} \tag{7.7}$$

$$\overline{y} = \frac{\int I(x,y)ydxdy}{\int I(x,y)dxdy} \tag{7.8}$$

From this, the quadruple moments can then be found by[61]

$$Q_{xx} = \frac{\int I(x,y)(x-\overline{x})^2dxdy}{\int I(x,y)dxdy} \tag{7.9}$$

$$Q_{xy} = \frac{\int I(x,y)(x-\overline{x})(y-\overline{y})dxdy}{\int I(x,y)dxdy} \tag{7.10}$$

$$Q_{yy} = \frac{\int I(x,y)(y-\overline{y})^2dxdy}{\int I(x,y)dxdy} \tag{7.11}$$

where $\overline{x}$ and $\overline{y}$ are the mean position in x and y respectively. These moments can be combined to generate the overall ellipticity, e, by the equation

$$e \equiv e_1 + ie_2 = \frac{Q_{xx} - Q_{yy} + 2iQ_{xy}}{Q_{xx} + Q_{yy} + 2(Q_{xx}Q_{yy} - Q_{xy}^2)^{1/2}} \tag{7.12}$$

where i^2 = -1[61] and similarly $g = g_1 + ig_2$. The lensed ellipticity, e_l, is related to the complex conjugate of the reduced shear, g^*, and the unlensed ellipticity, e_u, by

$$e_l = \frac{e_u + g}{1 + g^*e_u} \tag{7.13}$$

The ellipticity measured from the quadrupole moments is approximately equal to the reduced shear[61]

$$\langle e_l \rangle \approx g \tag{7.14}$$

Although this relies on the assumptions that there is no preferred orientation present in the galaxies and that a large sample size is present.

Using a generalised transform any nth-order moment can be found by[62]

$$\langle x^n y^m \rangle \equiv \frac{\int dxdyI(x,y)(x-\overline{x})^n(y-\overline{y})^m}{\int dxdyI(x,y)} \tag{7.15}$$

Equation 7.15 makes it possible to derive all the octopole moments required to find the first and third flexions by the equations

$$F = \left(\frac{Q_{xxx} + Q_{xyy}}{Q_{xxxx} + 2Q_{xxyy} + Q_{yyyy}}\right)\left(\frac{Q_{xxy} + Q_{yyy}}{Q_{xxxx} + 2Q_{xxyy} + Q_{yyyy}}\right) i\left(\frac{9}{4} - \frac{3(Q_{xx} + Q_{yy})^2}{Q_{xxxx} + 2Q_{xxyy} + Q_{yyyy}}\right)^{-1} \quad (7.16)$$

and

$$G = \frac{4}{3}\left(Q_{xxx} - 3Q_{xyy} + \frac{i(3Q_{xxy} - Q_{yyy})}{Q_{xxxx} + 2Q_{xxyy} + Q_{yyyy}}\right) \quad (7.17)$$

Figure 7.1 shows the effect of shear and flexion on an unlensed circular galaxy[63]. The largest problems faced in trying to resolve the galaxy's shape from the images are: the accuracy in determining the distance to the galaxy, the intrinsic alignment in the galaxy cluster, the accuracy of predictions of dark matter on small scales and an unbiased measurement of the shear[64]. The images used to determine shear have noise added from the atmosphere, telescope optics, pixelation from the CCD chips and readout noise from the CCDs. The galaxies used in weak lensing are faint. There is normally photon noise of about 5% error on the amount of light coming from the galaxy. The noise adds up to ten times more ellipticity to the image than the gravitational effect of dark matter[61]. These effects must be calibrated out. Fortunately, there will be many field stars in the same images as the galaxies. These stars can be considered point like objects, so their distortion can be used to map out the noise and remove it from the galaxy images. Residual shears and flexions are caused by the non-perfect removal of the telescopic distortions. These usually depend on the size and shape of the PSF. For example, if the PSF is more elliptical then the additive shear bias is larger[64]. It is therefore important to reduce the size and asymmetry of the PSF as much as possible in the telescope design and assembly.

7.1 Calculation of Shear and Flexion

The initial stage of calculating the shear and flexion was to generate PSF of the telescope over the focal plane and convolved with a modelled atmosphere. It was assumed that the atmosphere and CCDs contribute a circular Gaussian component of a full-width half maximum (FWHM) of 0.7 arcseconds. This corrosponds to the best expected seeing con-

ditions at La Blanco, where the median expected is 0.9 arcseconds[4]. This was convolved with the optics point spread function to obtain the full PSF.

In order to generate the PSFs the central ray of the i band filter, a wavelength of 743.9nm, was used in a ZEMAX model of the system, as created by Rebecca Bernstein and Sue Worswick. At all times the focal plane remained in its original position. Images of the generated PSFs are shown in figure 7.2, at positions (0,0) and (-0.54,0.46) degrees, both before and after they were combined with a Gaussian atmosphere. Quadrupole moments were then used to convert the PSFs at each point into a shear and flexion value. These values were then combined to create maps of the distortions over the entire focal plane, as shown in figure 7.3, where the perfect alignment map is compared against what is being taken as a worst case alignment. It is not possible to have a definite worst case alignment as six conditions are being considered: the real and imaginary part of the mass coverage of shear, first and third flexion. As these consider the different shapes that the distortion might take, shown in figure 7.1, a lens alignment that gives a maximum in one shape does not necessarily give the maximum distortion in another shape. Therefore in this chapter the worst case alignment used is that which gives the largest RMS spot size, the requirement that was used during the optical design.

The shear and flexion maps for the worst alignment whisker plot are quite unusual, with the shears heading vertically down the focal plane. Figures 7.4 and 7.5 look at the PSF generated by the optical modelling software in the top left hand quadrant of the shear and flexion maps. In figure 7.4, where the alignment of the optics is perfect, it can be seen that the PSFs do appear to radiate out of the centre of the focal plane. However, in figure 7.5, where the worst possible alignment was used, there appears to be large amount of distortion causing the PSF to be stretched vertically. The increase in size of the PSF between these two alignments can be clearly seen.

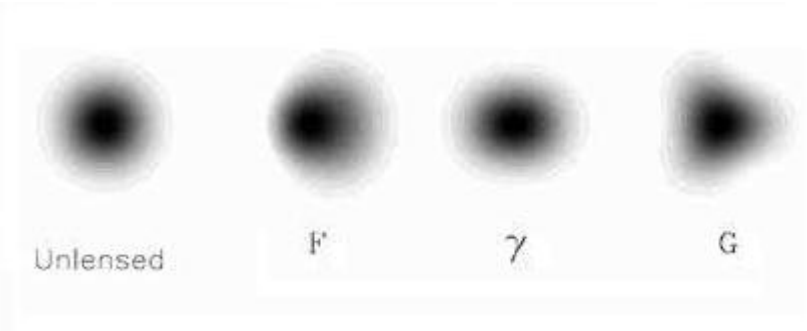

Figure 7.1: The effect of shear (γ, second from right) and flexion (1st flexion, F, is second from left and 3rd flexion, G, is far right) on an unlensed circular galaxy (far left)[63].

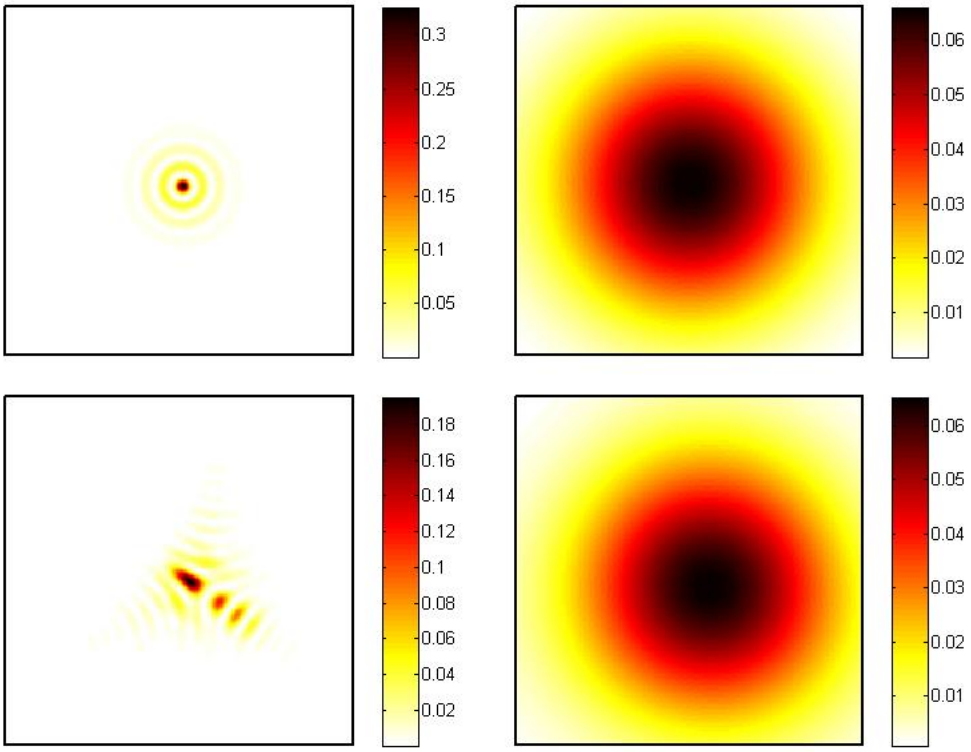

Figure 7.2: The point spread function at the centre of the focal plane, top left, and at the edge of the focal plane, bottom left. Top right shows the central PSF combined with a 0.7 FWHM Gaussian atmosphere and bottom right shows the edge PSF combined with the same Gaussian atmosphere. Each box is 56μm square. The intensity of the PSF is in arbitrary units.

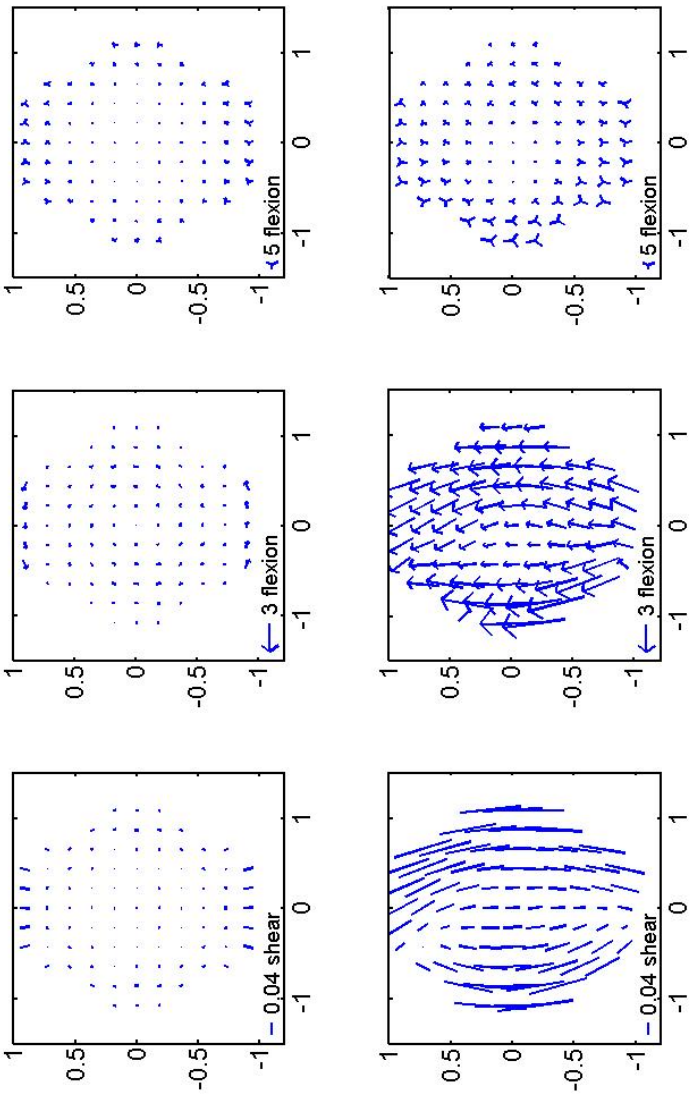

Figure 7.3: Whisker plots for the shear (far left), first (middle) and third (far right) flexion. The top row shows the whisker plots for the system when it is in perfect alignment and the bottom row shows the whisker plots when the lenses are in the worst alignment.

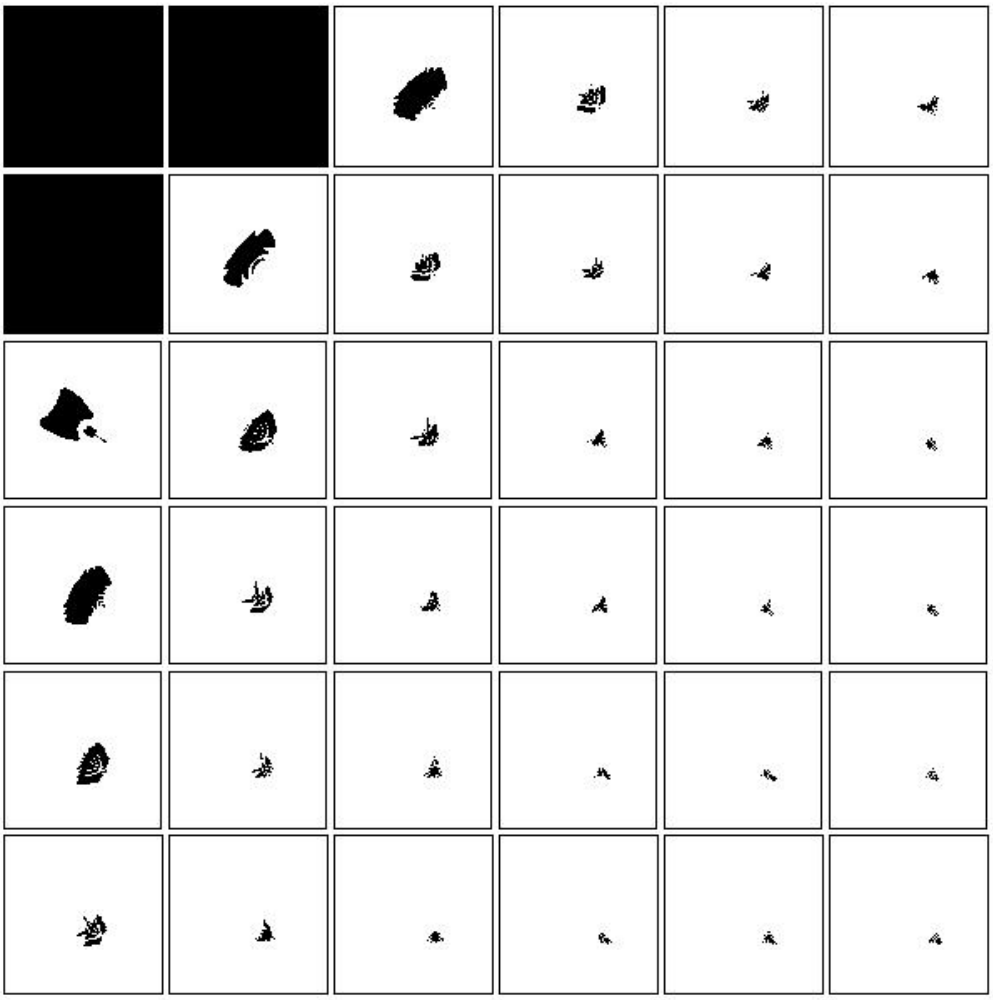

Figure 7.4: The raw PSFs generated by the optical modelling software in the top left hand quarter of focal plane, when the lenses were in perfect alignment.

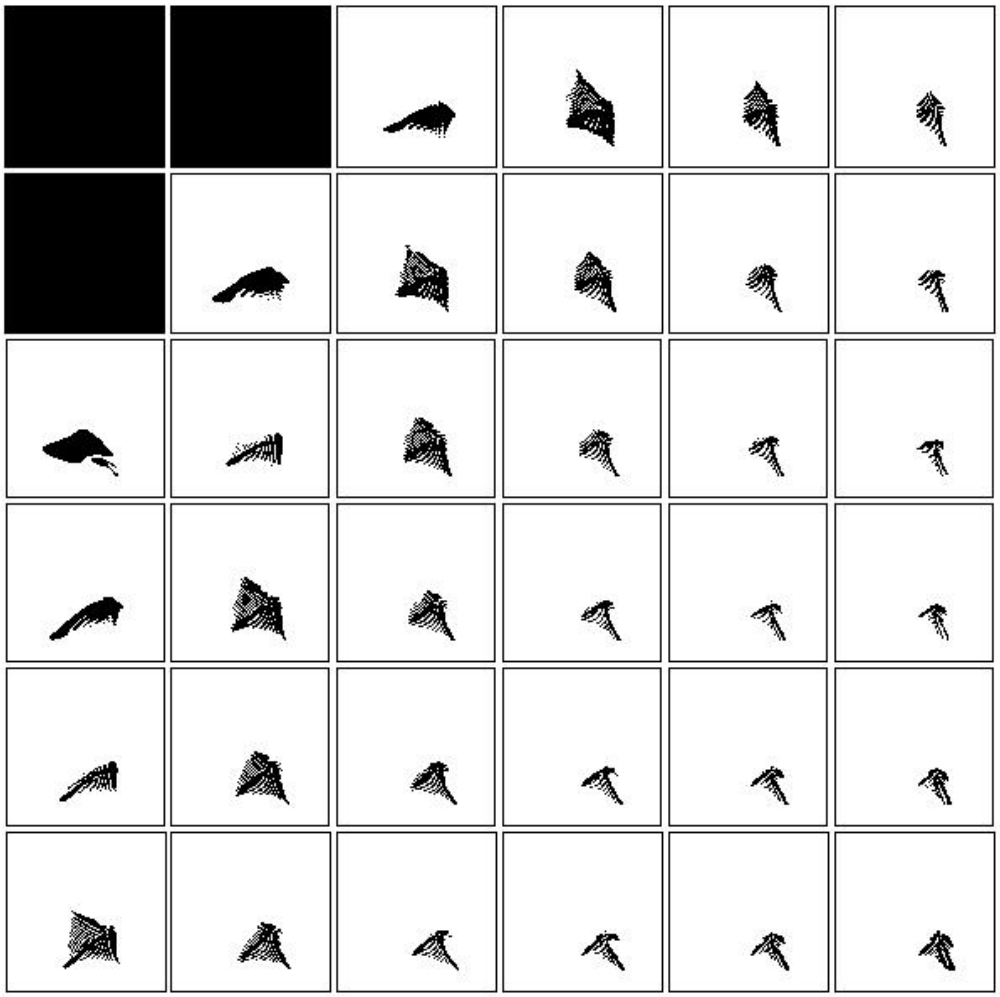

Figure 7.5: The raw PSFs generated by the optical modelling software in the top left hand quarter of focal plane, when the lenses were in worst possible alignment.

7.2 Mass Converegnce Maps

The shear and flexion were then used to create the mass map that would be simulated by the telescope optics. κ contains a real and imaginary part where the real part is that which could be caused by gravitational effects. The imaginary part is caused by pure noise and can only come from the telescope optics and never dark matter. Generally only the real part of the convergence map is considered as this contains the scientific data. The imaginary part can be used to determine the level of noise seen in the data as the telescope is expected to produce approximately the same amount of erronous real and imaginary signal. Here both the real and imaginary parts are investigated. The bases of this conversion of the shear to the convergence, κ_S, was the equation[65]:

$$\tilde{\kappa_S}(\vec{k}) = \tilde{\gamma}(\vec{k})\tilde{D}(\vec{k}) \tag{7.18}$$

where $\tilde{D}$ is a Fourier space construction over the area we are looking at equal to

$$\tilde{D} = \frac{k_1^2 - k_2^2 - 2ik_1k_2}{k_1^2 + k_2^2} \tag{7.19}$$

where k_1 and k_2 are defined as

$$k_1 = -\frac{\pi}{-X} : \frac{2\pi}{2X} : \frac{\pi}{X} \tag{7.20}$$

$$k_2 = -\frac{\pi}{-Y} : \frac{2\pi}{2Y} : \frac{\pi}{Y} \tag{7.21}$$

where 2X is the width and 2Y is the length of the focal plane in degrees. This definition allows k_1 and k_2 to remain constant between both the shear and flexion calculations. This expands out for $\tilde{K_S}$ to be

$$\tilde{K_S} = \frac{k_1^2 - k_2^2 - 2ik_1k_2}{k_1^2 + k_2^2}\tilde{\gamma} \tag{7.22}$$

with the inverse Fourier transform of this $\tilde{K_S}$ being the mass convergence map for the shear.

The definition used to determine κ_F and κ_G for both the real and imaginary parts of κ for the first and third flexion was derived using the same definition for κ as used for the

shear. For the first flexion[63]

$$\tilde{F} = \mathcal{F}(F_1 + iF_2) \tag{7.23}$$

we then define

$$\tilde{F} = \tilde{Q}\tilde{K_F} \tag{7.24}$$

where

$$\tilde{F_1} = -ik_1\tilde{K}k \tag{7.25}$$

$$\tilde{F_2} = -ik_2\tilde{K}k \tag{7.26}$$

we can then say that

$$\tilde{Q_1} = -ik_1 \tag{7.27}$$

$$\tilde{Q_2} = -ik_2 \tag{7.28}$$

These then combine to

$$\tilde{Q} = \frac{-ik_1 - k_2}{k_1^2 + k_2^2} \tag{7.29}$$

using the definition

$$\frac{1}{z} = \frac{z^*}{|z|^2} \tag{7.30}$$

where $|z|$ is equal to 1. Therefore we get

$$\tilde{K_F} = \frac{-ik_1 - k_2}{k_1^2 + k_2^2}(\tilde{F_1} + i\tilde{F_2}) \tag{7.31}$$

For third flexion[63]

$$\tilde{G} = \mathcal{F}(G_1 + iG_2) \tag{7.32}$$

then define

$$\tilde{G} = \tilde{R}\tilde{K_G} \tag{7.33}$$

where

$$\tilde{G_1} = 0.5i(k_1^3 - 3k_1k2^2)\tilde{\psi} \tag{7.34}$$

$$\tilde{G_2} = 0.5i(3k_1^2k_2 - k2^3)\tilde{\psi} \tag{7.35}$$

and $\tilde{K_G}$ is related to $\tilde{\psi}$ by[66]

$$\tilde{K_G} = -\frac{1}{2}(k_1^2 + k_2^2)\tilde{\psi} \tag{7.36}$$

therefore

$$\tilde{\psi} = \frac{-2\tilde{K}}{k_1^2 + k_2^2} \tag{7.37}$$

this gives us $\tilde{G_1}$ and $\tilde{G_2}$ to be

$$\tilde{G_1} = \frac{-i\tilde{K}(k_1^3 - 3k_1k2^2)}{k_1^2 + k_2^2} \tag{7.38}$$

$$\tilde{G_2} = \frac{-i\tilde{K}(3k_1^2k_2 - k2^3)}{k_1^2 + k_2^2} \tag{7.39}$$

This can then be expressed in terms of R, where $\tilde{R_1}$ is

$$\tilde{R_1} = \frac{-i(k_1^3 - 3k_1k_2^2)}{(k_1^2 + k_2^2)} \tag{7.40}$$

and $\tilde{R_2}$ is

$$\tilde{R_2} = \frac{-i(k_2^3 - 3k_1^2k_2)}{(k_1^2 + k_2^2)} \tag{7.41}$$

giving $\tilde{R^*}$ to be

$$\tilde{R^*} = \frac{-i(k_1^3 - 3k_1k_2^2)}{(k_1^2 + (k_2^3 - 3k_1^2k_2)}(k_1^2 + k_2^2)^2 \tag{7.42}$$

and hence the kappa convergence map for the third flexion is found by

$$\tilde{K_G} = \frac{-i(k_1^3 - 3k_1k_2^2) + (k_2^3 - 3k_1^2k_2)}{(k_1^2 + k_2^2)^2}\tilde{G} \tag{7.43}$$

For both the shear and flexion the real (E mode) and imaginary (B mode) of the convergence map were considered, these correspond to a shape distortion as shown in figure 7.6. The E mode is considered real as this is the pattern produced by an intervening dark matter source; it cannot give a B mode signal. The instrument however, will give both an E mode and a B mode signal, so any B mode signal present in the data can be used to determine how much of the E mode signal is from the telescope rather than the sky.

The convergence maps for a perfectly aligned system are shown in figure 7.7. In order to compare maps from multiple lens alignments the standard deviation, $\sigma_{\rm sys}$, was used as this allowed the map to be described by a single number.

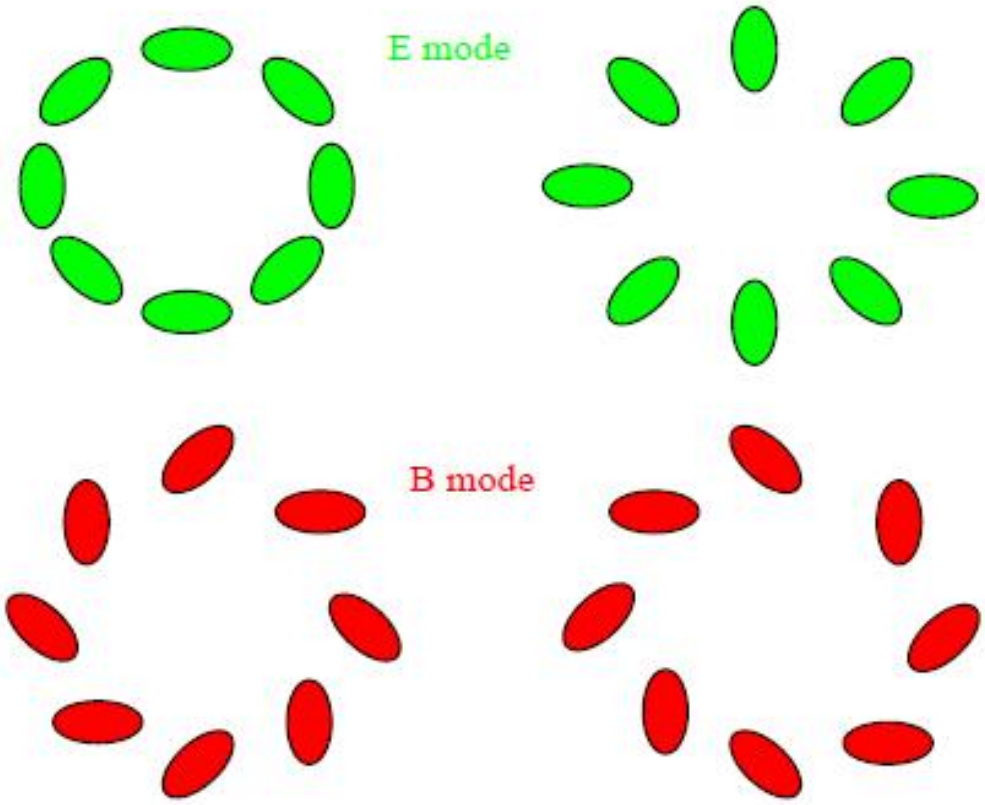

Figure 7.6: Schematic of the E and B mode[9]. The E mode shear pattern is seen where weak lensing is present, the B mode shear pattern is caused by telescopic distortions.

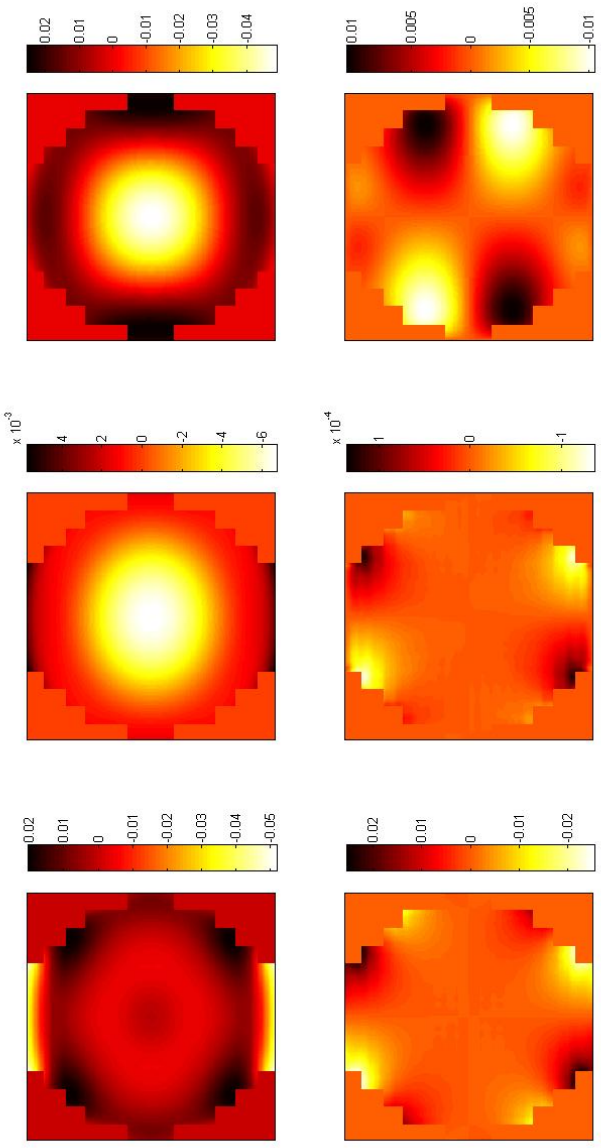

Figure 7.7: Maps of κ, a dimensionless quantity, for the shear, first and third flexion for a perfectly aligned optical system. E mode is on the top, B mode on the bottom.

7.3 Effects of Misalignment

In this section the effect of misalignment of lenses on the image quality was examined using two methods. The first involves moving each lens in turn with the others remaining in perfect alignment. This allows the effect each lens has on the system to be observed. The second moves all the lenses by a random amount, whilst staying within the given tolerances, to see the effect of multiple misalignments. Looking at multiple lens displacements allowed a general look at possible shear values that the system will have. Initially σ_{sys} was found for when the lenses were in perfect alignment and when they were in the worst case alignment. It is expected that the final alignment of DECam will produce results between the values shown in table 7.1.

	σ_E shear	σ_B shear	σ_E 1st flexion	σ_B 1st flexion	σ_E 3rd flexion	σ_B 3rd flexion
Perfect Alignment	$86\text{x}10^{-4}$	$44\text{x}10^{-4}$	$26\text{x}10^{-4}$	$0.23\text{x}10^{-4}$	$168\text{x}10^{-4}$	$38\text{x}10^{-4}$
Worst Alignment	$135\text{x}10^{-4}$	$79\text{x}10^{-4}$	$44\text{x}10^{-4}$	$14\text{x}10^{-4}$	$195\text{x}10^{-4}$	$47\text{x}10^{-4}$

Table 7.1: Best and worst possible variation in κ for shear and flexion.

7.3.1 Relative effect of single lenses

An initial test was done to investigate which lens has the largest effect on the image quality. To determine this each lens was moved out to its maximum alignment tolerance in steps of 20% of maximum tolerance. This was done to each lens twice, once for decentre and then for tilt. For this test only one lens was moved and all other lenses kept in perfect alignment. The resultant shears and flexions of the PSF generated were then converted into a mass convergence map. In order to quantify the relative impact of different lenses on shear and flexion, the σ_{sysE} and σ_{sysB} were investigated, where E denotes the real part of the convergence map and B denotes the imaginary part. The σ_{sys} for each tilt and decentre outcome was then plotted against those for the other lenses. These plots can been seen in figures 7.8 and 7.9.

When the lenses have a pure decentre applied to them C1 creates the largest change in the shear, with both C1 and C2 effecting the flexion maps equally. However this is only a slight change, with the lens tilts causing a greater increase in σ_{sys}. When tilted, C4 has the greatest effect on shear and flexion sizes. Here again C1 and C2 have similar contributions, mainly within the flexions. Both C3 and C5 have little effect when tilted

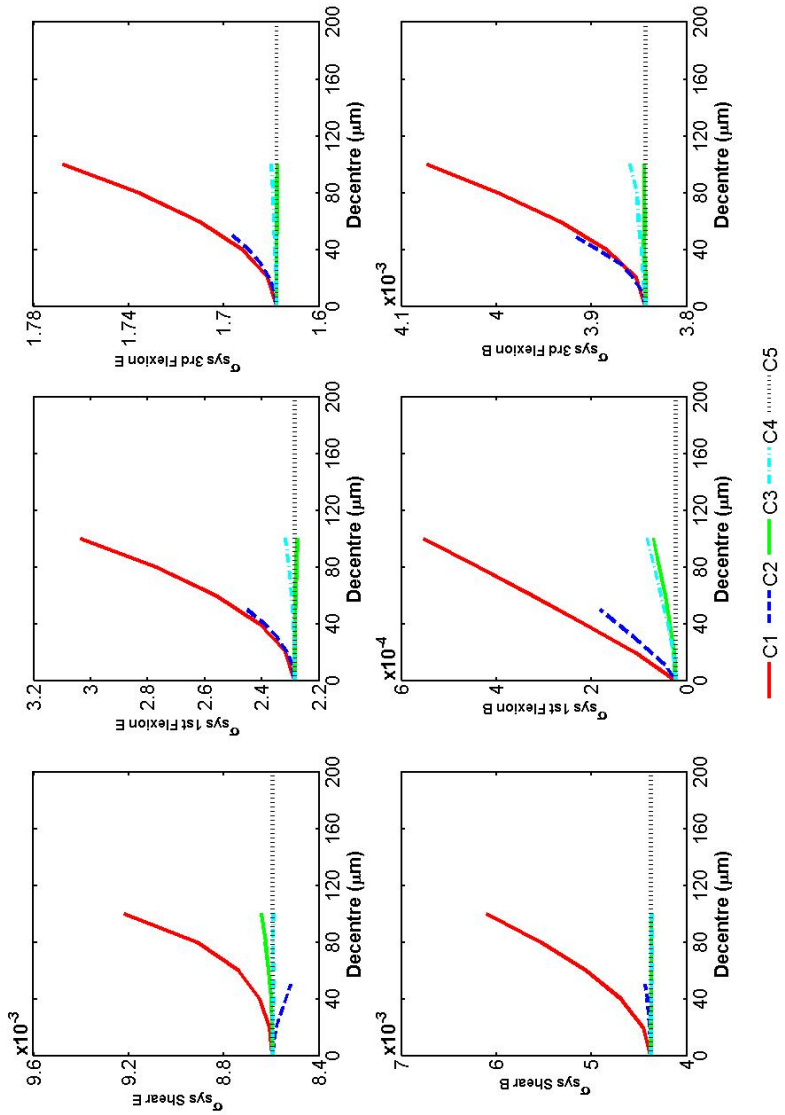

Figure 7.8: The standard deviation, $\sigma_{\rm sys}$ of the κ map is plotted against an individual decentre of each lens. The real part is shown on top and the imaginary part on the bottom, with the far left being shear, the middle 1st flexion and the far right 3rd flexion.

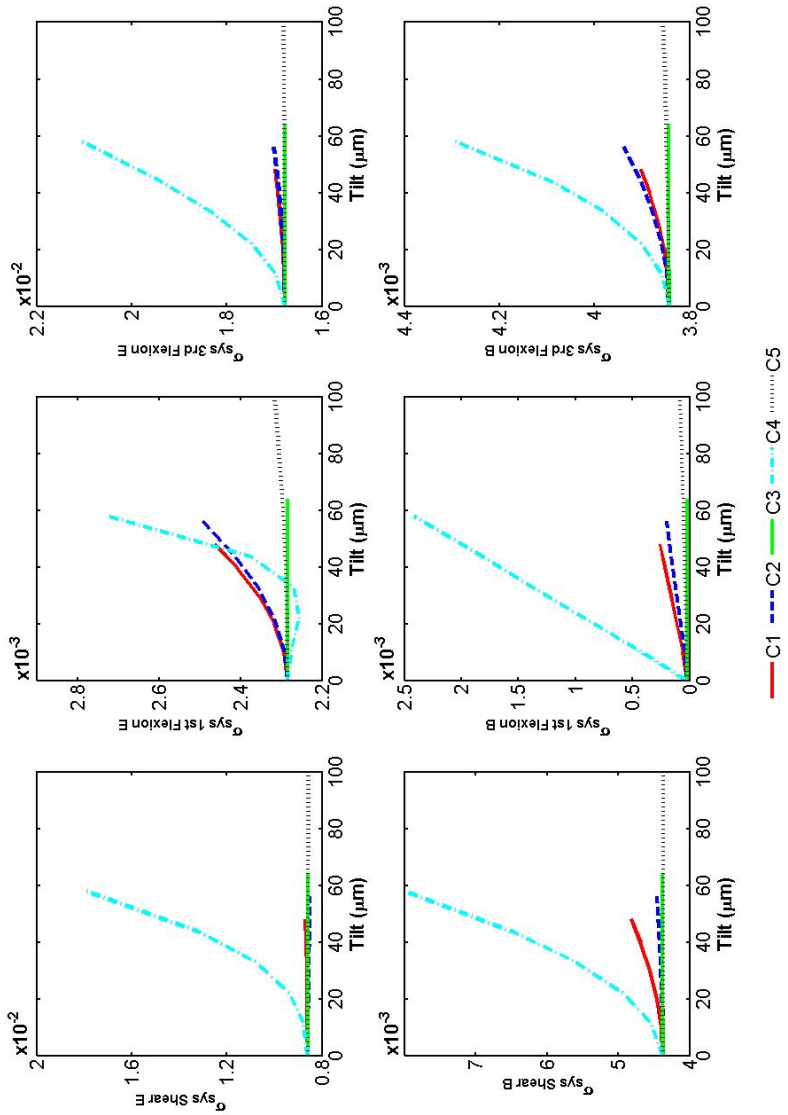

Figure 7.9: The standard deviation, $\sigma_{\rm sys}$ of the κ map is plotted against an individual tilt of each lens. The real part is shown on top and the imaginary part on the bottom, with the far left being shear, the middle 1st flexion and the far right 3rd flexion.

or decentred. There are noticeable differences between the E and B modes. The shears' B mode is a factor of 10 smaller than the E mode, with a similar effect in the third flexion. However, the first flexion's E and B modes are very similar.

7.3.2 Multiple lens offsets

This subsection sets out to answer two questions. Firstly, does the relative importance of the lenses hold when more than one lens is off-set from the ideal position? Secondly, what is a realistic size of distortion that will come from the completed optical camera? In order to answer these questions sixty three different alignments were created, where each lens was given a random tilt and decentre. This was randomised using a Gaussian distribution with a FWHM of 3 sigma of the tolerance for each degree of freedom. The resultant $\sigma_{\rm sys}$ values from these PSFs were then plotted as a histogram in figure 7.10.

The values for the random misalignments are much greater than for the single lens movements. This then leads to the question of which lens is causing the greatest effect. To determine this a correlation co-efficient was used to see if there was a link between an increase in $\sigma_{\rm sys}$ and an increase in either the tilt or decentre of each lens. A value above 0.26 means that the lens gives a significant contribution to either the shear or flexion. It was found that decentre gave no contribution to $\sigma_{\rm sys}$, so the results in table 7.2 only show the tilts.

It is interesting to note that the C4 tilt, which looked very important in figure 7.9, has very little correlation with the $\sigma_{\rm sys}$ of the multiple lens off-sets. However, the tilt of lenses C1 and C2 now dominate the distortions. In a way this is expected, as one of DECam's optical designers, Sue Worswick, found that C1 and C2 had the largest impact on when displaced on the size of the R.M.S. spot size. Figure 7.11 shows the plots of $\sigma_{\rm syssheareE}$ plotted against the C1, C2 and C4 tilt. These findings show that the correct placements of C1 and C2 are the most critical for the weak lensing data, although if possible C4 should not be tilted.

7.4 Implications for Weak Lensing

In order to recover a weak lensing signal the systematics in the residual shear must be controlled, allowing the results to be statistically significant. This tolerance on the variance, $\sigma^2_{\rm sys}$ can be defined by area of the survey, A_s, the galaxy density, n_g and the median

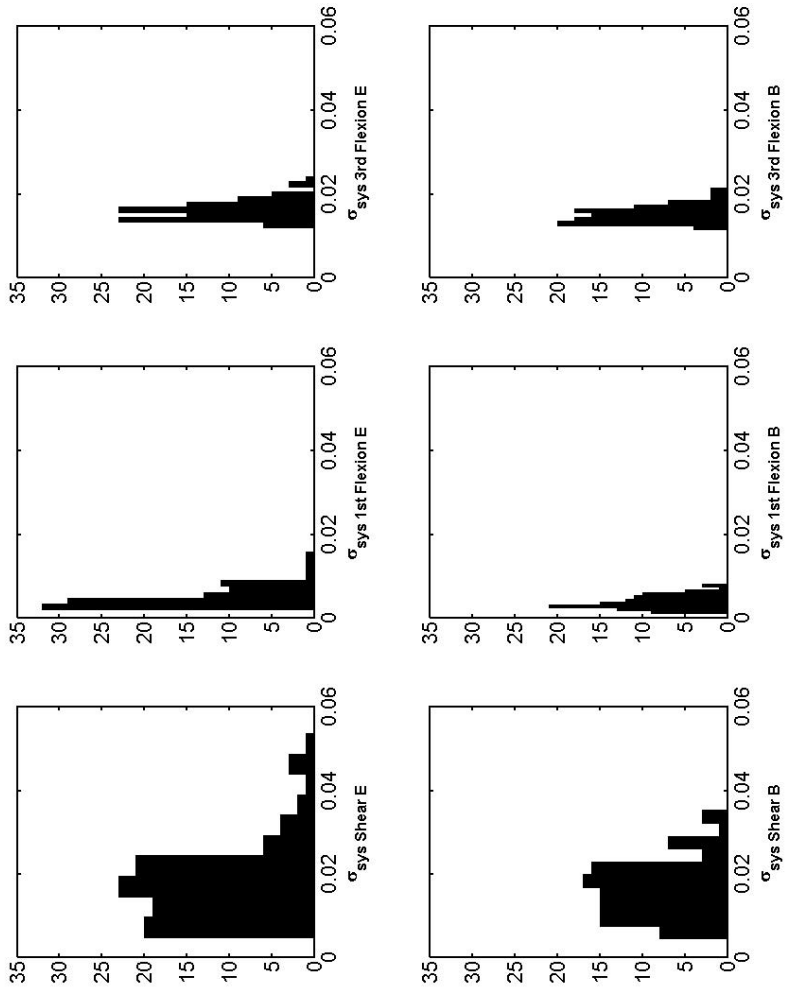

Figure 7.10: Histogram of 63 random misalignments of all lenses showing the $\sigma_{\rm sysE}$ and $\sigma_{\rm sysB}$ of the system. On the left is the shear, in the centre is the first flexion and on the right is the 3rd flexion.

	correlation co-efficient	
	E mode	B mode
C1 tilt		
Shear	0.39	0.55
First Flexion	0.55	0.69
Third Flexion	0.69	0.66
C2 tilt		
Shear	0.49	0.67
First Flexion	0.06	0.19
Third Flexion	0.25	0.37
C3 tilt		
Shear	0.17	0.11
First Flexion	0.06	0
Third Flexion	0	0
C4 tilt		
Shear	0.14	0.21
First Flexion	0.14	0.08
Third Flexion	0.05	0.05
C5 tilt		
Shear	0.25	0.22
First Flexion	0.16	0.18
Third Flexion	0.22	0.25

Table 7.2: Table showing correlation coefficients of $\sigma_{\rm sysshear}$ from a covariance matrix for random misalignments, within the given tolerances. For the E and B modes only the lens tilts are shown as all the decentres were below the error value of 0.26.

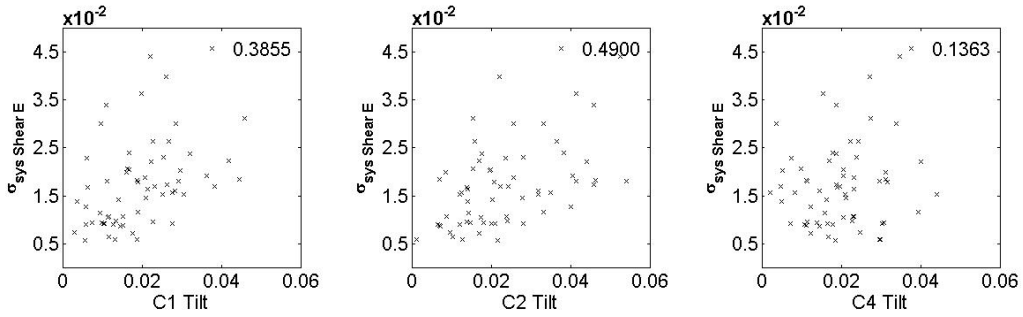

Figure 7.11: Correlations between tilting the lenses C1, C2 and C4 and the $\sigma_{\rm sysshearE}$ values, with the correlation function in the top right hand corner of the plot.

redshift, z_m[67], where

$$\sigma^2_{\rm sys} < 10^{-7} \left(\frac{A_s}{2 \times 10^4 degrees^2} \right)^{-0.5} \left(\frac{n_g}{35 arcmin^{-2}} \right)^{-0.5} \left(\frac{z_m}{0.9} \right)^{-0.6} \tag{7.44}$$

For DES, A_s is 5000 deg^2, n_g is 10 arcmin^{-2} and z_n is 0.7[4]. This puts a requirement on DES for $\sigma_{\rm sys}$ to be less than 0.0008. Whilst all the results quoted previously are significantly above this level, this has not been taking into account the expected reduction by the weak lensing pipeline. The use of this pipeline will create what is known as the residual shear and when the residual shear is used the numbers drop significantly. The current best method would reduce the shears by a factor of 126[64]. Reductions in the flexions were not calculated using this method so it is not yet confirmed whether they can also be reduced by this amount. This brings the $\sigma_{\rm sysshear}$ of these residual shears to under the required 8x10^{-4} for both perfect and worst case alignment as shown in table 7.3.

	Residual Shear	
	σsys$_{\rm E}$	σsys$_{\rm B}$
Perfect alignment	2.7x10^{-4}	1.4x10^{-4}
Worst alignment	4.3x10^{-4}	2.5x10^{-4}

Table 7.3: Expected size of remaining shear in the image after the telescopic distortions have been removed to the limits of current analysis techniques.

Chapter 8

Summary and Future Work

If it draws blood, it's hardware

Unknown

This chapter summaries the conclusions of the work in this thesis, as well as presenting ideas for future work. At the time of writing DECam is on schedule for shipment in late 2011 with first light in 2012. No major obstacles were encountered in the construction and alignment of DECam and the author has no reason to believe that all the alignment specifications will not be achieved.

8.1 Summary of Work Presented

The initial work presented showed that the compression modulus of the RTV as gained by experimentation matched the theoretical models used in the creation of the DECam design, giving confidence to the FEA results. A production method was created using moulds to produce identical pads, to ensure equal weight and stress distribution over the lens. CTE and chemical composition testing showed that the cell material for DECam was compliant with the specifications, although the prototype material was of an unusual composition that did not match the material mix requested.

The metrology of the cells showed that the alignment procedure developed would allow for the specified tolerances to be met. The mating rings of cells C1, C2 and C4 were

Lens	tilt (μm)	decentre (μm)
C2	< 10	12
C3	< 5	4
C4	18	3
C5	< 20	< 70

Table 8.1: Final alignment of lenses C2-C5.

successfully aligned and bolted to their retaining rings despite the non-circularity of the rings and the cells. Maps of the mating ring's run-out were created to allow for realignment of the cell during lens-cell assembly. Four of the lenses, C2-C5 were successfully aligned within their cells with C2-C4 being glued into position and C5 held by plastic mounts, due to it being the cryostat window. All of these lenses are well within specifications as shown in table 8.1.

Work was done on classifying the shape of the PSF into three forms: shear, first and third flexion. These were used to determine the effect of lens misalignment on the weak lensing data. It was found that when all the lenses were in some form of misalignment the C1 lens had the largest effect on image quality. However, when all the lenses were in perfect alignment and a single lens was displaced, C4 affected the results the most. In both cases a tilt caused greater degradation of the image quality than a decentre of the same amount. Even with the worst possible image quality, as given by the specifications, the image quality will remain in the required range for weak lensing analysis to be performed on the data.

8.2 Future Work

In this section a few ideas for extensions to this thesis are examined. There is much work that the author would have liked to complete, but was unable to do so due to time constraints. As this thesis is being written work is under way to mount C3 to C2 and align C2/C3 into the barrel along with C4 and C5. The attachment of the C1 axial pads is being done in preparation for the alignment of this lens into it's cell before being mounted on the cone. The alignment of DECam will need to be checked once it has been shipped to CTIO in order to ensure that no movement has occurred during transport.

Whilst much work was performed on the compression modulus of the RTV pads no experiments were performed on the ability of the radial RTV pads to hold the lens in position when the telescope is away from the zenith. From FEA models the thin radial

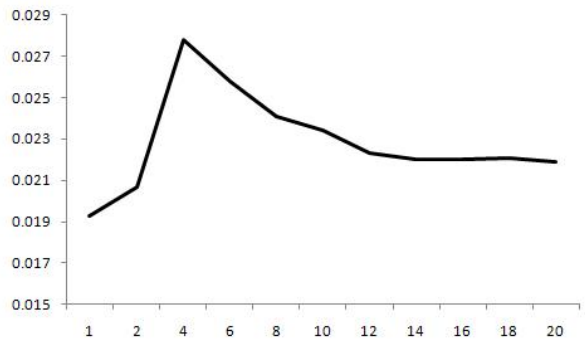

Figure 8.1: Median shear at perfect alignment when different number of wavelengths are used. The wavelengths are evenly spaced over the i filter band.

pads provide support the lens preventing it moving, however no experimental data on this has been taken. Whilst there is no reason to disbelieve the FEA model, confirmation would help support the FEA results where a gravity vector is added after the pads are attached to the side of the lens.

Shear and flexions were calculated using the prime wavelength of the i band filter. It was hoped to expand this out to 14 wavelengths evenly spaced over the filter band, to give a more realistic version of the shears and flexions that would be found. Figure 8.1 shows that by changing the number of wavelengths the median shear over the focal plane changes. Once 14 wavelengths are used there the increase in shear size plateaus off. It was also hoped to repeat the expected σ_{sys} calculations for the r and z bands in which it is also hoped to preform weak lensing measurements.

It is known that during telescope operations the alignment of the lenses will change as the telescope moves away from the zenith. As well as the lenses moving within their cells the barrel will also flex. This will create a new κ map different from that at the zenith and the impact of this on the variance of the κ map would be interesting to see. Once the lenses have been attached to the barrel the final alignment of the entire system will be known. This data can be combined with the wavefront maps of the lenses, as provided by SESO, to create a full model of DECam in ZEMAX. The telescopic distortions can then be mapped and a more accurate model created.

8.2.1 Future Optical Correctors

DECam is scheduled to operated for five years and so an upgrade is already in the pipeline, the Dark Energy Spectrograph, DESpec. It aims to allow spectrographic data to be

taken from targets identified by DECam, using absorption and emission lines to determine redshifts more accurately. By measuring the velocities of galaxies to higher precision it is possible to reduce the uncertainty in the mass to light ratio, allowing tighter constraints on dark energy. DESpec would use the same optics as DECam, apart from C5 which acts as a cover to protect the DECam CCDs. An atmospheric dispersion corrector (ADC) would also be required, room is available within the FCM for this[68].

BigBoss is a new spectrograph that has been commissioned for the Mayall 4-meter telescope at Kitt Peak. It aims to observe spectroscopic targets selected from previous imaging surveys and will cover 14,000 square degrees that overlaps current imaging surveys like PanSTARRS-1 and DES. It aims to be operational for 500 nights over five years and take 5000 simultaneous spectra over the wavelengths 340nm to 1060nm. The corrector consists of four lenses with two ADCs and a focal plane of 0.95m diameter, making it significantly larger than DES. The corrector elements will be mounted in a similar fashion to DES, with an RTV interface between the glass and its metal holder. A nickel-iron alloy will be used in the cell material with the exact mix to be determined by the thickness requirement of the RTV pad for an athermal design. Flexures will again be used to isolate the lens-cell assembly from the barrel. Construction on BigBoss is expected to start in 2013, aiming for first light in 2016 and survey operation in 2017[69].

The construction of DES has raised several areas in the design that could be improved upon to make the alignment of future optical correctors easier. An increase in the size of the mating ring, and having it lapped, would provide more support to the cell as well as giving an easier surface to flatten the cell to during alignment. By attaching the ring earlier, during the manufacturing process, the mating surface could be used as a reference surface from the axial surface to be aligned to. As discrete points were used to seat the lens another possibility is to machine small, individual units with the correct sloped surface and attach these to the cell, rather than the axial surface being machined from the cell. This would allow the large cell to have all surfaces lapped flat to micron precision as well as having smaller parts which are easier to manufacture to high accuracy, with the use of jigs allowing identical reproduction.

Glossary

Meanings of all TLAs and similar used within this thesis:

- ADC - Atmospheric Dispersion Corrector
- C1-5 - Lens-cells for positions 1-5
- CCD - Charge-Coupled Device
- CDM - Cold Dark Matter
- CTIO - Cerro Tololo Inter-American Observatory
- CTE - Coefficient of Thermal Expansion
- DDGI - Digital Dial Gauge Indicators
- DECam - Dark Energy Camera
- DES - Dark Energy Survey
- DESpec - Dark Energy Spectrometer
- E_c - Compression modulus
- FCM - Filter Changer Mechanism
- FEA - Finite Element Analysis
- FWHM - Full Width Half Maximum
- MMT - Multiple Mirror Telescope

- NPL - National Physics Laboratory
- OSL - Optical Science Laboratory
- Pan-STARRS - Panoramic Survey Telescope and Rapid Response System
- PSF - Point Spread Function
- PSI - Pounds per Square Inch
- PS1 - Pan-STARRS 1
- RTV - Room Temperature Vulcanizing (silicone rubber)
- RTV560 - the name of a specific type of room temperature vulcanizing silicone rubber, used in the construction of DECam
- S - Shape factor
- S factor - Shape factor
- SEM - Scanning Electron Microscope
- STFC - Science, Technology and Facilities Council
- TLA - Three Letter Acronym
- UCL - University College London
- w - Dark energy equation of state parameter
- Λ - The cosmological constant
- ΛCDM - The current standard cosmological model

Afterword

When the author left the project in September 2011, the last lens, C1, had yet to be aligned with its cell and all the lens-cells systems were awaiting alignment to the barrel. A brief overview of the final alignment of DECam is given here. The work in this section was completed between September 2011 and January 2012. As this afterword is being written DECam sits at CTIO awaiting integration with the Blanco telescope.

By the end of September 2011 only one cell had yet to have the axial pads attached. This was C1, which had a variation in the height of the sloped surface which was at the edge of the RTV pad's compression range. In order to compensate for this, the height variation the thicknesses of the pads were varied to provide an even surface for the lens to sit on. Fermilab's results of the variation in the C1 axial sloped surface were used to determine the ideal pad height at each axial pad position. The C1 gluing tool was then modified to provide the correct glue layer. The results of this can be seen in figure 8.2. The axial pads were no more than 20μm from their intended height. Once the axial pads had been attached to the cell, the C1 lens and cell were aligned to the rotational axis of the rotary table, using the same method as for the other lenses. After the lens had been glued into the cell the finial position of the C1 lens to cell was found. When the mating ring had been levelled, the lens' concave surface had a run-out of 0μm. The convex surface of the lens had a tilt of 74μm and a decentre of 33μm, both towards north (-Y). These combined to give a total micrometer run-out of 65μm on the convex surface.

Once all the lens-cell systems were completed were then aligned and pinned into the barrel. This was done by aligning the optical axis, as defined by Fermilab's measurements, to the rotational axis of the rotary table by clocking off of the body and cone. As there were no external reference surfaces on the barrel that were suitable for clocking, the O-

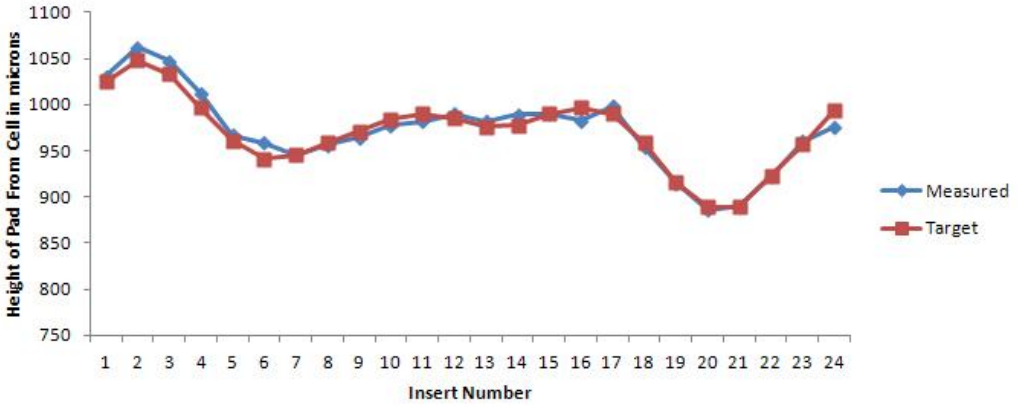

Figure 8.2: Height variation of the C1 axial pads. The values marked "'Target"' were the intended height for the pads with those marked "'Measured"' being the measured values.

ring grove in the body flange was used as the centring reference surface. No measurements were done by Fermilab defining the O-ring grove with respect to the optical axis and inevitably there will be some offset between them. As such, the alignment measurements will be affected by a decentre offset. This means that the measurements taken below are probably an upper limit on the alignment precision.

C2 and C3 were the first lens-cells placed into the barrel. A DDGI measured a run-out on the concave surface of C3 of 40μm with a peak 60 degrees from +Y. This can be compared to the run-out of 25μm at 30 degrees from +Y which were on C3 just after the lens had been glued into its cell. C4 was then attached, completing the body section of the barrel. The concave surface of C4 had a run out of 60μm, with the highest point 20 degrees from +Y. When the C4 lens' convex surface was measured after the lens-cell had been glued together a run out of 36μm with a peak had 45 degrees was found. About 37μm can be accounted for due to the wedge of the C4 lens giving a calculated run out on the lens of 23μm.

By mid-December 2011 DECam was ready for shipment. It was sealed into bags to protect against contamination and placed in specially built packing crates. In January 2012 DECam was unpacked at CTIO. A visual inspection of the lenses, cells and barrel showed no obvious damage. Measurements were taken with the laser system which gave the similar results to measurements taken earlier at UCL. This makes it highly unlikely that the lenses have shifted out of alignment during transport.

Figure 8.3: The body section of DECam raised on the crane at CTIO. The C2 lens is visible at the bottom of the body and is undergoing inspection by Dr Brooks.

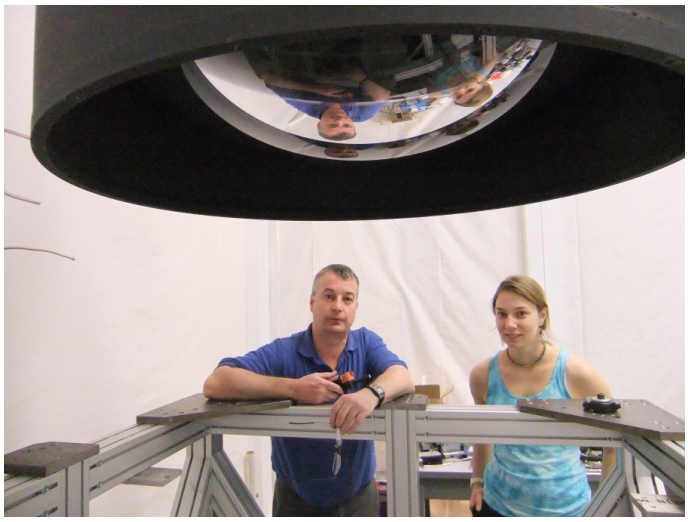

Figure 8.4: The cone section of DECam is suspended by the crane at CTIO. Underneath are Dr Brooks and the author.

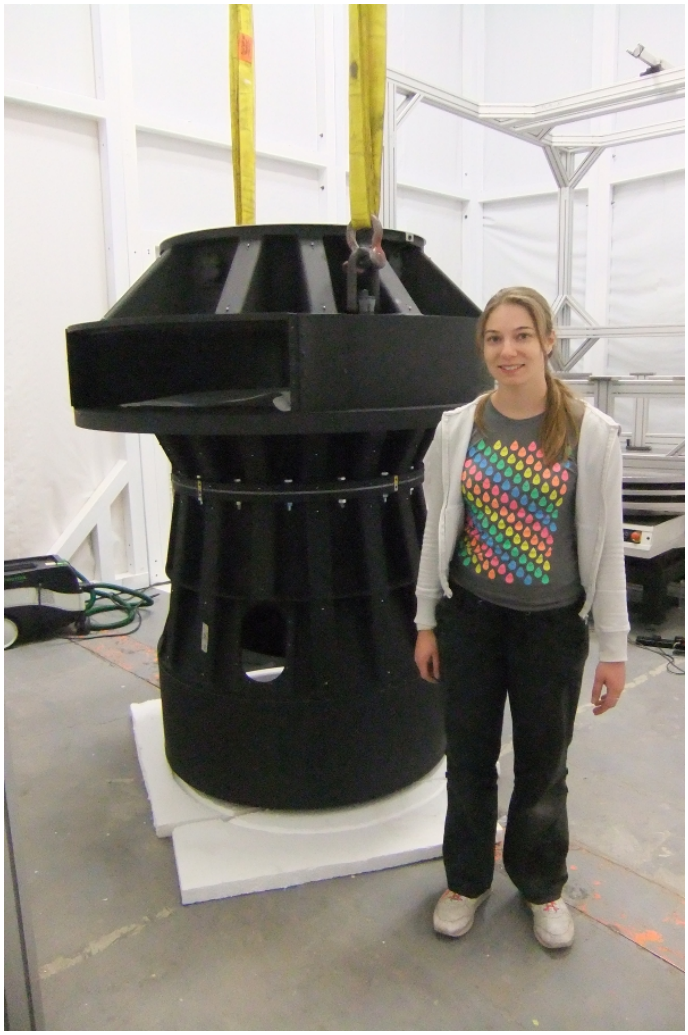

Figure 8.5: The author standing next to the completed DECam at CTIO after alignment of the body and cone.

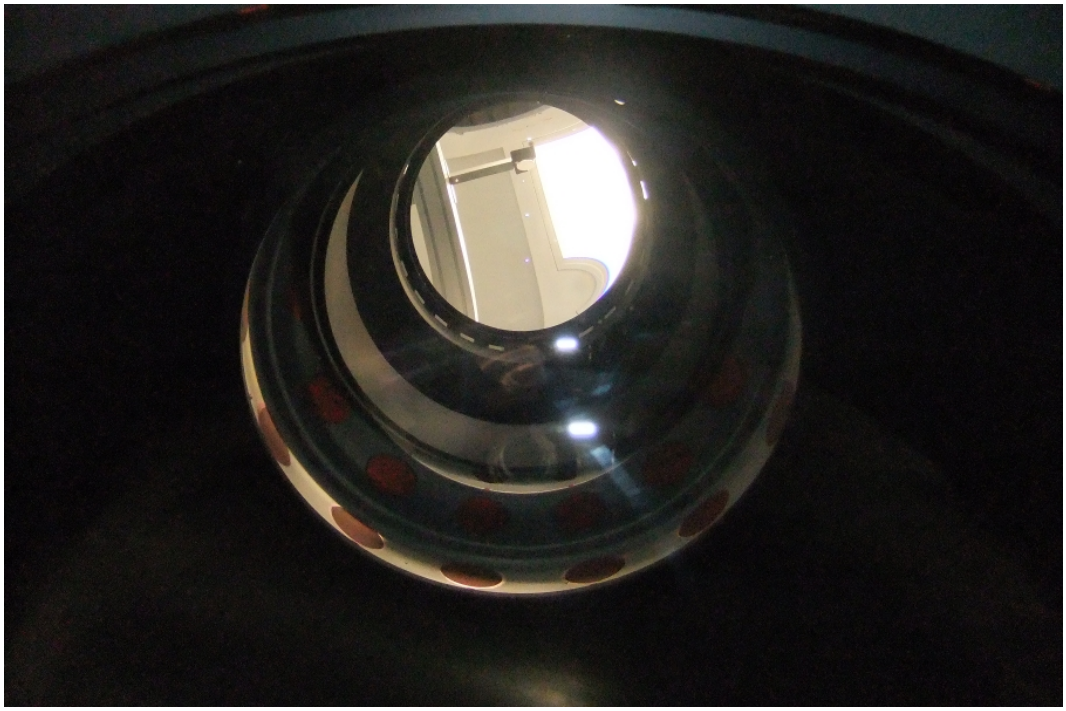

Figure 8.6: Looking up the completed DECam from C1 to C4. C1 is the nearest lens, but this cannot be seen. The most obvious features are C2's radial pads and their reflection, the side of the body between C2 and the filter chamber and gaps between C4's flexures. One of the alignment mirrors and part of the support structure can be seen at the centre of the image.

Bibliography

[1] Rich, J., [*Fundamentals of Cosmology*], Springer, 2nd edition ed. (2009).

[2] Riess, A. G., Filippenko, A. V., Challis, P., Clocchiatti, A., Diercks, A., Garnavich, P. M., Gilliland, R. L., Hogan, C. J., Jha, S., Kirshner, R. P., Leibundgut, B., Phillips, M. M., Reiss, D., Schmidt, B. P., Schommer, R. A., Smith, R. C., Spyromilio, J., Stubbs, C., Suntzeff, N. B., and Tonry, J., "Observational Evidence from Supernovae for an Accelerating Universe and a Cosmological Constant," **116**, 1009–1038 (Sept. 1998).

[3] Perlmutter, S., Aldering, G., Goldhaber, G., Knop, R. A., Nugent, P., Castro, P. G., Deustua, S., Fabbro, S., Goobar, A., Groom, D. E., Hook, I. M., Kim, A. G., Kim, M. Y., Lee, J. C., Nunes, N. J., Pain, R., Pennypacker, C. R., Quimby, R., Lidman, C., Ellis, R. S., Irwin, M., McMahon, R. G., Ruiz-Lapuente, P., Walton, N., Schaefer, B., Boyle, B. J., Filippenko, A. V., Matheson, T., Fruchter, A. S., Panagia, N., Newberg, H. J. M., Couch, W. J., and The Supernova Cosmology Project, "Measurements of Omega and Lambda from 42 High-Redshift Supernovae," **517**, 565–586 (June 1999).

[4] Annis, J., Dodelson, S., Flaugher, B., Frieman, J., Gladders, M., Hui, L., Kent, S., Lin, H., Limon, P., Peoples, J., Scarpine, V., Stebbins, A., Stoughton, C., Tucker, D., Wester, W., Brunner, R., Karliner, I., Mohr, J., Plante, R., Selen, M., Thaler, J., Carlstrom, J., Dodelson, S., Frieman, J., Hu, W., Kent, S., Sheldon, E., Wechsler, R., Aldering, G., Roe, N., Bebek, C., Levi, M., Perlmutter, S., Abbott, T., Smith, R. C., Suntzeff, N., and Walker, A., "A Proposal to NOAO for the Dark Energy Survey," (2004).

[5] Prialnik, D., [*An Introduction to the Theory of Stella Structure and Evolution*], Cambridge University Press (2000).

[6] Flaugher, B., "The Dark Energy Survey instrument design," in [*Society of Photo-Optical Instrumentation Engineers (SPIE) Conference Series*], *Presented at the Society of Photo-Optical Instrumentation Engineers (SPIE) Conference* **6269** (July 2006).

[7] "Dark Energy Survey White Paper for the Dark Energy Task Force," (2005).

[8] Kaiser, N. and Squires, G., "Mapping the dark matter with weak gravitational lensing," **404**, 441–450 (Feb. 1993).

[9] Munshi, D., Valageas, P., van Waerbeke, L., and Heavens, A., "Cosmology with weak lensing surveys," *Physics Reports* **462**, 67–121 (June 2008).

[10] Kirk, D., Laszlo, I., Bridle, S., and Bean, R., "Optimising cosmic shear surveys to measure modifications to gravity on cosmic scales," *ArXiv e-prints* (Sept. 2011).

[11] Kirk, D., Bridle, S., and Schneider, M., "The impact of intrinsic alignments: cosmological constraints from a joint analysis of cosmic shear and galaxy survey data," **408**, 1502–1515 (Nov. 2010).

[12] Fata, R. G. and Fabricant, D. G., "Design of a cell for the wide-field corrector for the converted MMT," in [*Society of Photo-Optical Instrumentation Engineers (SPIE) Conference Series*], D. Vukobratovich, P. R. Yoder, & V. L. Genberg, ed., *Presented at the Society of Photo-Optical Instrumentation Engineers (SPIE) Conference* **1998**, 32–38 (Sept. 1993).

[13] Fata, R. G. and Fabricant, D. G., "Mounting large lenses in wide-field instruments for the converted MMT," *Optical Astronomical Instrumentation* **3355**(1), 275–284, SPIE (1998).

[14] Pedichini, F., Giallongo, E., Ragazzoni, R., Di Paola, A., Fontana, A., Speziali, R., Farinato, J., Baruffolo, A., Magagna, C. E., Diolaiti, E., Pasian, F., Smareglia, R., Anaclerio, E., Gallieni, D., and Lazzarini, P. G., "LBC: the prime focus optical imagers at the LBT telescope," in [*Society of Photo-Optical Instrumentation Engineers (SPIE) Conference Series*], M. Iye & A. F. M. Moorwood, ed., *Presented at the Society of Photo-Optical Instrumentation Engineers (SPIE) Conference* **4841**, 815–826 (Mar. 2003).

[15] Diolaiti, E., Farinato, J., Ragazzoni, R., Vernet, E., Arcidiacono, C., and Faccin, F., "Optical alignment of the LBT prime focus camera," in [*Society of Photo-Optical Instrumentation Engineers (SPIE) Conference Series*], A. F. M. Moorwood & M. Iye, ed., *Society of Photo-Optical Instrumentation Engineers (SPIE) Conference Series* **5492**, 513–524 (Sept. 2004).

[16] Gentile, G., Ragazzoni, R., Diolaiti, E., Farinato, J., Hill, J., Bertam, R., and Baruffolo, A., "LBT report activities concerning the optomechanics alignment of the Large Binocular Camera's Red Channel," in [*Society of Photo-Optical Instrumentation Engineers (SPIE) Conference Series*], *Presented at the Society of Photo-Optical Instrumentation Engineers (SPIE) Conference* **7014** (Aug. 2008).

[17] Hodapp, K. W., Siegmund, W. A., Kaiser, N., Chambers, K. C., Laux, U., Morgan, J., and Mannery, E., "Optical design of the Pan-STARRS telescopes," in [*Society of Photo-Optical Instrumentation Engineers (SPIE) Conference Series*], J. M. Oschmann Jr., ed., *Society of Photo-Optical Instrumentation Engineers (SPIE) Conference Series* **5489**, 667–678 (Oct. 2004).

[18] Kaiser, N., Burgett, W., Chambers, K., Denneau, L., Heasley, J., Jedicke, R., Magnier, E., Morgan, J., Onaka, P., and Tonry, J., "The Pan-STARRS wide-field optical/NIR imaging survey," in [*Society of Photo-Optical Instrumentation Engineers (SPIE) Conference Series*], *Society of Photo-Optical Instrumentation Engineers (SPIE) Conference Series* **7733** (July 2010).

[19] Morgan, J. S. and Kaiser, N., "Alignment of the Pan-STARRS PS1 prototype telescope optics," in [*Society of Photo-Optical Instrumentation Engineers (SPIE) Conference Series*], *Society of Photo-Optical Instrumentation Engineers (SPIE) Conference Series* **7012** (Aug. 2008).

[20] Leger, R. F., "Decam Hexapod And Positional Adjustment System Specifications." Internal Document number 335-v1, des-docdb.fnal.gov (November 15, 2006).

[21] Abbott, T., "Blacno Performance for the Preliminary Design Review." Internal Document number 16-v1, des-docdb.fnal.gov (2006).

[22] Abbott, T. M. C., Schumacher, G., Warner, M., Mondaca, E., Schmidt, R. E., Cantarutti, R., Martinez, M., Estay, O., Delgado, F., and Walker, A., "Cerro Tololo

Inter-American Observatory, Victor M. Blanco 4-m Telescope: an upgrade to the telescope control system," in [*Society of Photo-Optical Instrumentation Engineers (SPIE) Conference Series*], *Presented at the Society of Photo-Optical Instrumentation Engineers (SPIE) Conference* **7012** (Aug. 2008).

[23] Abbott, T., "DECam & CTIO." Internal Document number 141-v3, des-docdb.fnal.gov (July 2006).

[24] Abbott, T., "The Blanco Telescope." Internal Document number 273-v1, des-docdb.fnal.gov (Dec 2006).

[25] R. French Leger, Dave McGinnis, A. S. D. D. G. G. and Flaugher, B., "DECam Hexapod Position Adjustment System Specification." Internal Document number 427-v17, des-docdb.fnal.gov (4 February 2008).

[26] Leger, R. F., "Design Review For Prime Focus Hexapod Support System For The Dark Energy Camera." Internal Document number 575-v1, des-docdb.fnal.gov (November 30, 2005).

[27] Stefanik, A., "Critical Review of the Optical Design for the Dark Energy Survey: Barrel." Internal Document number 365-v1, des-docdb.fnal.gov (March 2007).

[28] Flaugher, B. L., Abbott, T. M. C., Annis, J., Antonik, M. L., Bailey, J., Ballester, O., Bernstein, J. P., Bernstein, R., Bonati, M., Bremer, G., Briones, J., Brooks, D., Buckley-Geer, E. J., Campa, J., Cardiel-Sas, L., Castander, F., Castilla, J., Cease, H., Chappa, S., Chi, E. C., da Costa, L., Depoy, D. L., Derylo, G., de Vicente, J., Diehl, H. T., Doel, P., Estrada, J., Eiting, J., Elliott, A., Finley, D., Frieman, J., Gaztanaga, E., Gerdes, D., Gladders, M., Guarino, V., Gutierrez, G., Grudzinski, J., Hanlon, B., Hao, J., Holland, S., Honscheid, K., Huffman, D., Jackson, C., Karliner, I., Kau, D., Kent, S., Krempetz, K., Krider, J., Kozlovsky, M., Kubik, D., Kuehn, K. W., Kuhlmann, S. E., Kuk, K., Lahav, O., Lewis, P., Lin, H., Lorenzon, W., Marshall, S., Martínez, G., McKay, T., Merritt, W., Meyer, M., Miquel, R., Morgan, J., Moore, P., Moore, T., Nord, B., Ogando, R., Olsen, J., Peoples, J., Plazas, A., Roe, N., Roodman, A., Rossetto, B., Sanchez, E., Scarpine, V., Schalk, T., Schindler, R., Schmidt, R., Schmitt, R., Schubnell, M., Schultz, K., Selen, M., Serrano, S., Shaw, T., Simaitis, V., Slaughter, J., Smith, R. C., Spinka, H., Stefanik, A., Stuermer,

W., Sypniewski, A., Talaga, R., Tarle, G., Thaler, J., Tucker, D., Walker, A. R., Weaverdyck, C., Wester, W., Woods, R. J., Worswick, S., and Zhao, A., "Status of the dark energy survey camera (DECam) project," in [*Society of Photo-Optical Instrumentation Engineers (SPIE) Conference Series*], *Presented at the Society of Photo-Optical Instrumentation Engineers (SPIE) Conference* **7735** (July 2010).

[29] Cease, H., "Requirements and Specifications DES Document NNN: Imager Vessel." Internal Document number 781-v1, des-docdb.fnal.gov (21 August 2007).

[30] Greg Derylo, K. S. and Diehl, H., "Procedure For Mounting the Imager Onto The Corrector Barrel." Internal Document number 5115-v5, des-docdb.fnal.gov (12 August 2011).

[31] Flaugher, B., "DECam Technical Requirements (Cooling)." Internal Document number 953-v3, des-docdb.fnal.gov (Sept 2007).

[32] Abbott, T., Annis, J., DePoy, D. L., Flaugher, B., Kent, S., Lin, H., and Merritt, W., "Dark Energy Camera Specifications and Technical Requirements." Internal Document number 806-v23, des-docdb.fnal.gov (Sept 2011).

[33] DePoy, D. L., "Technical Specifications for Design and Fabrication of Large Format Filters for Dark Energy Camera (DECam)." Internal Document number 3284-v4, des-docdb.fnal.gov (Nov. 11, 2009).

[34] Tarlé, G., Bigelow, B., Boprie, D., Cooper, C., Dede, E., Lorenzon, W., Nord, B., Schubnell, M., and Weaverdyck, C., "Large format filter changer mechanism for the dark energy survey," in [*Society of Photo-Optical Instrumentation Engineers (SPIE) Conference Series*], *Presented at the Society of Photo-Optical Instrumentation Engineers (SPIE) Conference* **7739** (July 2010).

[35] Bigelow, B. C., "Preliminary Review of the Optical Design for the Dark Energy Survey: Corrector Opto-Mechanics." Internal Document number 17-v4, des-docdb.fnal.gov (2006).

[36] Doel, P., Abbott, T., Antonik, M., Bernstein, R., Bigelow, B., Brooks, D., Cease, H., DePoy, D. L., Flaugher, B., Gladders, M., Gutierrez, G., Kent, S., Stefanik, A., Walker, A., and Worswick, S., "Design and status of the optical corrector for the

DES survey instrument," *Ground-based and Airborne Instrumentation for Astronomy II* **7014**(1), 70141V, SPIE (2008).

[37] Bernstein, R., "Critical Design Review for the Dark Energy Survey Optics: Corrector Optical Design." Internal Document number 348-v2, http://des-docdb.fnal.gov (2007).

[38] Incorporated, C., "HPFS Fused Silica Standard Grade Product Sheet," (2003).

[39] Kent, S., Bernstein, R., Abbott, T., Bigelow, B., Brooks, D., Doel, P., Flaugher, B., Gladders, M., Walker, A., and Worswick, S., "Preliminary optical design for a 2.2 degree diameter prime focus corrector for the Blanco 4 meter telescope," in [*Society of Photo-Optical Instrumentation Engineers (SPIE) Conference Series*], *Society of Photo-Optical Instrumentation Engineers (SPIE) Conference Series* **6269** (July 2006).

[40] Doel, P., "Mechanical Assembly Tolerances for Lens C1-C5 (Barrel-Cell separate fiducial manufacture)." Internal Document number 2571-v1, http://des-docdb.fnal.gov (Aug 2009).

[41] Worswick, S., "Preliminary Review of the Optical Design for the Dark Energy Survey: Sensitivity Analysis." Internal Document number 37-v2, des-docdb.fnal.gov (2006).

[42] Doel, P. and Kendrew, S., "Technical Note on RTV radial pad thickness." Internal Document number 222-v1, http://des-docdb.fnal.gov (2006).

[43] Silicones, G. B., "RTV560 Data Sheet."

[44] Tipler, P. A. and Mosca, G., [*Physics for Scientists and Engineers, Extended Version*], W.H. Freeman and Company, 5th edition ed. (2004).

[45] Saito, H., e., [*Physics and applications of Invar Alloys: Honda Memorial Series and Materials Science; No.3*], Marusen Company Ltd., Tokyo (1978).

[46] Bailey, J., "CTIO C5 and Flat Window Cell Design." Internal Document number 3413-v1, des-docdb.fnal.gov (July 22, 2009).

[47] Brooks, D., "Lens, Cell and Barrel Alignment Procedure for Dark Energy Survey Instrument Corrector Optics." Internal Document number 352-v6, des-docdb.fnal.gov (Mar 2007).

[48] Fata, Kradinov, and Fabricant, "Mounting Large Lenses for the MMT's f/5 Wide-Field Corrector: Lessons Learned," *Proceedings of SPIE: Ground-based Instrumentation for Astronomy* **5492**, 553–563 (2004).

[49] P.B.Lindley, Fuller, K., and Muhr, A., *Engineering Design with Natural Rubber*. Malaysian Rubber Producers' Research Association, 5th ed. (1984).

[50] Michels, G. J., Genberg, V. L., and Doyle, K. B., "Finite element modeling of nearly incompressible bonds," in [*Society of Photo-Optical Instrumentation Engineers (SPIE) Conference Series*], A. E. Hatheway, ed., *Society of Photo-Optical Instrumentation Engineers (SPIE) Conference Series* **4771**, 287–295 (Sept. 2002).

[51] Mast, T. S., Choi, P. I., Cowley, D. J., Faber, S. M., James, E. C., and Shambrook, A. A., "Elastomeric lens mounts," in [*Society of Photo-Optical Instrumentation Engineers (SPIE) Conference Series*], S. D'Odorico, ed., *Society of Photo-Optical Instrumentation Engineers (SPIE) Conference Series* **3355**, 144–154 (July 1998).

[52] Burlakov, S. F., Volod'kov, M. T., and Ermolaev, B. I., "The reduction of the expansion coefficient of Invar by quenching," *Metal Science and Heat Treatment* **12**, 759–760 (1970). 10.1007/BF00652727.

[53] Stefanik, A., "Cell and spacer placement in DECam corrector." Internal Document number 5357-v3, des-docdb.fnal.gov (March 17 2011).

[54] Doel, P., "C5 cell accident report and analysis." Internal Document number 3741-v1, des-docdb.fnal.gov (21 October 2009).

[55] Doel, P., "Status of the optical corrector for the DES survey." Internal Document number 4245-v1, des-docdb.fnal.gov (March 2010).

[56] Doel, P., "Lens Parameters." Internal Document number 4567-v5, des-docdb.fnal.gov (07 Jan 2011).

[57] Brooks, D., "Detailed lens, cell and barrel alignment procedure." Internal Document number 2592-v1, des-docdb.fnal.gov (2009).

[58] Brooks, D., "Lens, Cell and Barrel Alignment." Internal Document number 3374-v3, des-docdb.fnal.gov (2009).

[59] Ingalls, A. G., [*Amateur Telescope Making, Book 1*], Scientific American, Inc. New York (1972).

[60] Goldberg, D. M. and Bacon, D. J., "Galaxy-Galaxy Flexion: Weak Lensing to Second Order," **619**, 741–748 (Feb. 2005).

[61] Bridle, S., Shawe-Taylor, J., Amara, A., Applegate, D., Balan, S. T., Berge, J., Bernstein, G., Dahle, H., Erben, T., Gill, M., Heavens, A., Heymans, C., High, F. W., Hoekstra, H., Jarvis, M., Kirk, D., Kitching, T., Kneib, J.-P., Kuijken, K., Lagatutta, D., Mandelbaum, R., Massey, R., Mellier, Y., Moghaddam, B., Moudden, Y., Nakajima, R., Paulin-Henriksson, S., Pires, S., Rassat, A., Refregier, A., Rhodes, J., Schrabback, T., Semboloni, E., Shmakova, M., van Waerbeke, L., Witherick, D., Voigt, L., and Wittman, D., "Handbook for the GREAT08 Challenge: An image analysis competition for cosmological lensing," *Annals of Applied Statistics* **3**, 6–37 (2009).

[62] Goldberg, D. M. and Natarajan, P., "The Galaxy Octopole Moment as a Probe of Weak-Lensing Shear Fields," **564**, 65–72 (Jan. 2002).

[63] Bacon, D. J., Goldberg, D. M., Rowe, B. T. P., and Taylor, A. N., "Weak gravitational flexion," **365**, 414–428 (Jan. 2006).

[64] Bridle, S., Balan, S. T., Bethge, M., Gentile, M., Harmeling, S., Heymans, C., Hirsch, M., Hosseini, R., Jarvis, M., Kirk, D., Kitching, T., Kuijken, K., Lewis, A., Paulin-Henriksson, S., Schölkopf, B., Velander, M., Voigt, L., Witherick, D., Amara, A., Bernstein, G., Courbin, F., Gill, M., Heavens, A., Mandelbaum, R., Massey, R., Moghaddam, B., Rassat, A., Réfrégier, A., Rhodes, J., Schrabback, T., Shawe-Taylor, J., Shmakova, M., van Waerbeke, L., and Wittman, D., "Results of the GREAT08 Challenge: an image analysis competition for cosmological lensing," **405**, 2044–2061 (July 2010).

[65] Bartelmann, M. and Schneider, P., "Weak gravitational lensing," **340**, 291–472 (Jan. 2001).

[66] Bridle, S. L., Hobson, M. P., Lasenby, A. N., and Saunders, R., "A maximum-entropy method for reconstructing the projected mass distribution of gravitational lenses," **299**, 895–903 (Sept. 1998).

[67] Amara, A. and Réfrégier, A., "Systematic bias in cosmic shear: extending the Fisher matrix," **391**, 228–236 (Nov. 2008).

[68] Diehl, T., "DESpec." Internal Document number 5017-v1, des-docdb.fnal.gov (Oct 2010).

[69] Schlegel, D., Abdalla, F., Ahn, C., Allende-Prieto, C., Annis, J., Aubourg, E., Azzaro, M., Baltayi, C., Baugh, C., Bebek, C., Becerril, S., Blanton, M., Boltong, A., Bromleyg, B., Cahn, R., Carton, P.-H., Chuf, Y., Cortes, M., Dawsong, K., Dey, A., Diehl, H. T., Doel, P., Ealet, A., Edelstein, J., Eppelle, D., Escoffier, S., Evrardc, A., Faccioli, L., Frenk, C., Gehai, M., Gerdesc, D., Gondolog, P., Gonzolez-Arroyo, A., Grossan, B., Heckman, T., Heetderks, H., Ho, S., Honscheid, K., Huterer, D., Ilbert, O., Ivansg, I., Jelinsky, P., Jing, Y., Kent, S., Kiedag, D., Kim, C., Kneib, J.-P., Kongf, X., Kosowsky, A., Krishnan, K., Lahav, O., Lampton, M., LeBohec, S., Brun, V. L., Levi, M., Lim, H., Linder, E., Lorenzonc, W., Magneville, C., Malina, R., Marinoni, C., Martinez, V., Majewskih, S., McDonald, P., McKayc, T., McMahonc, J., Menard, B., Miralda-Escude, J., Modjaz, M., Mostek, N., Newmand, J., Nichole, R., Nugent, P., Olsen, K., Padmanabhani, N., Park, I., Peacocka, J., Percivale, W., Perlmutter, S., Peroux, C., Petitjean, P., Prada, F., Prieto, E., Prochaska, J., Reil, K., Rockosi, C., Roe, N., Rollinde, E., Roodman, A., Ross, N., Rudnick, G., Ruhlmann-Kleider, V., Schimd, C., Schubnell, M., Scoccimaro, R., Seljak, U., Seo, H., Sholl, M., Shulte-Ladbeck, R., Slosar, A., Smoot, G., Springer, W., Stril, A., Szalay, A., Tao, C., Tarle, G., Taylor, E., Tilquin, A., Tinker, J., Wang, J., Wang, T., Weaver, B. A., Weinberg, D., White, M., Wood-Vasey, M., Yang, J., Yeche, C., Zakamska, N., Zentner, A., Zhai, C., and Zhang, P., "A Proposal to NOAO for the BigBOSS Experiment at Kitt Peak National Observatory," (October 1, 2010).

Acknowledgements

Only those with their feet on rock can build castles in the air.
Carpe Jugulum, Terry Pratchett

PhDs are not done alone. Many people have helped me to get this far and I thank you all. Here I would like to mention a few names.

My first thank you must go to my supervisor Peter Doel who as put up with me asking obvious questions, sent me on conferences and to meetings and has corrected so many badly worded reports and chapters. Anasuya Aruliah, my second supervisor who reminded me that I was here to write a thesis. David Brooks, who corrected all my minor mistakes and stopped me making any major ones. Jim and everyone in the MAPS workshop who appear to be psychic and can make exactly the part I wanted from a drawing that looked nothing like it. Sarah Bridle and David Bacon who introduced me to the wonderful world of cosmology and weak lensing. STFC should also be thanked for funding me and paying my fees for four years, making this thesis possible.

Sam and Caz. Without you two I would have never made it to the end of the PhD. Your support, advice, Women in Optics journal club and understanding of how frustrating FEA can be has been invaluable. I will never forget the importance of cake.

Adam, Cris and DK for their explanation of all things cosmological in small words. As well all of the PhD students and postdocs, past and present, of Group A and those friends outside of Astro who have listened to my ups and downs. My office mates who have put up with the occasional swear word directed at the computer when my FEA wouldn't mesh and everyone who has listened to me moan about how little rubber pads just won't

give the expected result. Thank you also for the pub trips and the random conversations. Thanks to you these past four years have been absolutely brilliant.

My boyfriend Spike must also get a mention. He has always made me smile, lifted my spirits and given me a shoulder to cry on. Without you, getting to the end of this PhD would have been so much harder.

Finally my parents, who have always fed, encouraged, clothed, put money in my pocket and housed me. Thank you for all of this and the encouragement to do physics. The careers advice my Dad gave me when I was in school should also be mentioned here. After being told by the school careers advisor that astrophysics was "too hard" and I should "try something easier" you told me to "ignore them and do what you want. We will always support you." So I ignored them, did what I wanted and they have always supported me. It seems to have turned out all right.